Ph.D. Thesis

# Quantitative detection of molecules using Surface Enhanced Raman Spectroscopy with silver nanocluster films as active substrates

RAJU BOTTA

School of Physics
University of Hyderabad

Ph.D. Thesis

Quantitative detection of molecules using Surface Enhanced Raman Spectroscopy with silver nanocluster films as active substrates

RAJU BOTTA

2015

# Quantitative detection of molecules using Surface Enhanced Raman Spectroscopy with silver nanocluster films as active substrates

A thesis submitted for the award of

Doctor of Philosophy

in PHYSICS

by

RAJU BOTTA

(10PHPH10)


School of Physics

University of Hyderabad

Hyderabad-500046, Telangana, India.

**December 2015**

In the memory of my Father Veeraiah
and
Grandmother Ramulamma

## DECLARATION

I hereby declare that the thesis entitled "**QUANTITATIVE DETECTION OF MOLECULES USING SURFACE ENHANCED RAMAN SPECTROSCOPY WITH SILVER NANOCLUSTER FILMS AS ACTIVE SUBSTRATES**" submitted by me under the supervision of Prof. C. Bansal and Co-supervison of Dr. A. Rajanikanth is a bonafide research work which is also free from plagiarism. I also declare that it has not been submitted previously in part or in full in this university or any other University or Institution for the award of any degree or diploma. I hereby agree that my thesis can be deposited in Shodganga/INFLIBNET.

**A report on plagiarism statistics from the University Librarian is enclosed.**

Raju Botta

(Reg. No. 10PHPH10)

Co-supervisor

Supervisor

SCHOOL OF PHYSICS
UNIVERSITY OF HYDERABAD

---

## CERTIFICATE

This is to certify that the research work compiled in the thesis entitled "**QUANTITATIVE DETECTION OF MOLECULES USING SURFACE ENHANCED RAMAN SPECTROSCOPY WITH SILVER NANOCLUSTER FILMS AS ACTIVE SUBSTRATES**" is an original work carried out by Mr. **RAJU BOTTA** under my supervision and the same has not been submitted for the award of any degree of any University or Institution.

Dr. A. Rajanikath
(Co-supervisor)

Prof. C. Bansal
(Supervisor)

Dean
School of Physics

## ACKNOWLEDGEMENTS

I wish to express my deep sense of gratitude to Prof. C. Bansal, for his inspiring guidance and constant encouragement at every stage of this work and also Dr. A. Rajanikanth.

I would like to thank, the present Dean Prof. R. Singh and the former Deans, Prof. S. Chaturvedi, Prof. S.P. Tiwari and Prof. C. Bansal, for providing all the facilities to carry out my research. I would also like to thank the faculties, School of Physics. Special thanks to my doctorial committee members, Prof. D. Narayana Rao and Dr. S.V.S. Nageswara Rao, for fruitful discussions and valuable suggestions.

I thank Abraham for the help he has extended in administrative matters. I thank Deepthi, Chinna Das, Sunitha, Laxminarayana, Sureshbabu, Ravishanker, Alemuddin, Somu, Shailaja and other non-teaching employees of School of Physics.

I am grateful to Dr. G. Upender for enlightening me at the first glance of research.

I would like to thank my fellow lab mates Dr. Seema Awasthi, Joshy Joseph and Jitu.

Without friends nothing is possible in this regard I would like to thank Ramesh Ade, B. Ravi Kumar, Ummar Pasha, Dr. Pavan Kumar Naik, Bandi Ashok, M. Yadaiah, M. Sathyanarayana, J. Pundareekam Goud, M. Narasimhappa, S.L.D. Varma, G. Rahul, Dr. Ravikant Verma, Sanjeeb Dey, Santanukumar Padi, Dr. M. Suman Kalyan, Dr. Ananthaiah, Pavan Venu Prakash, Umasankar (late), M. Vijaya Laxmi, M. Padmavathi, K.N. Deepthi, Uma Lavanya, Luhluh Jahan, Monisha, Dr. Saipriya, Ramya, Jasmeet Kaur, Nisha Goutham, Atiya Farheen, Rasna, Rashmita, Thirupathi, Mahender,

Chakradhar Sahoo, Shivarama Krishna, Venkatesh, Sandeep, Srinivas, Mohan, Chander, Sampath, I.V. Sankar, Aalu, Narasimha Raju, Sanjeev, Sivanagi Reddy, Nagaraju, Binoy, Dhanunjay, Manikantha, Siva R.K, Shravan, Anilkumar, Venkata Sai, Prakash, Dr. Poonam Tandon, Dr. Anju Ahlawat, Dr. Dileepkumar Misra, Dr. R. Sathyavathi, Arun, Dr. Sri Ramulu, Dr. Shekhar, Dr. Suresh, Dr. Shankaraiah, Dr. Shanker, Dr. Ramudu, Dr. Devendrakumar, Dr. Parthsarathy, Dr. Swaroop Raj, Dr. Yugandhar, Dr. Joji Kurian and Dr. Saikiran.

I also thank all my friends from ACRHEM, SEST, Chemistry and SOS.

I would like to thank my B.Sc. friends, D. Mohan, P. Ashok, G. Sainath, Parashuram Pawar, R. Jagan Naik, M. Ramesh, K. Srinivas, A. Anilkumar, P. Swamy, K. Mahender, U. Balraju, Prince and K. Pochalu.

I am thankful to my M.Sc. friends, M. Reddikumar, Hema Sunder, V. Srinivasa Rao, Rajesh, Praveenkumar, Naresh, Sampath, Sivaprasad and other M.Sc. friends.

I thank my School friends from APRS Nagarjuna Sagar and Intermediate college friends from APRJC Sarvail.

I would like to thank my childhood friends, Paramesh, Ambedkar, Naresh, Radhakrishna etc.

I am grateful to B. Yadagiri for his support and encouragement.

“If it does not bend as a sapling, will it when it is a tree?” without my teachers effort I may not be here, so I would like to thank my teachers Himaja, Srinivas Reddy, Dr. Mallikarjun Goud and Battu Sharma etc.

I would like to express my sincere gratitude to Bharat Ratna Dr. B.R. Ambedkar, without his effort I may not be here today.

In the end, I would like to express my deepest and sincere gratitude to my parents, my grandmother and my family members. Without their support, their encouragement and their care, this work would never have been done.

December 2015 (Raju Botta)

Hyderabad

## CONTENTS

**List of figures:**

**List of Tables:**

# Chapter 1

# Introduction

## 1.1 Raman scattering:

Raman scattering is the inelastic scattering of photons by matter. In 1928, Sir Chandrasekhara Venkata Raman and K. S. Krishnan first observed this inelastic scattering effect experimentally [1]. The discovery was publicly announced on February 28, 1928 and presented by Sir C. V. Raman in the inaugural address of the South Indian Science Association on March 16, 1928. Sir C. V. Raman was awarded the Nobel Prize for this discovery in 1930. A historic account of the discovery has been given by Krishnan and Shankar [2]. The measurement and analysis of the Raman scattered photons that contain useful information on the vibrational and rotational modes or electronic excitation energy of the material under investigation is called Raman spectroscopy.

The ensuing scattering processes for a photon interacting with matter can be illustrated using a Jablonski diagram as shown in figure 1.1, which shows the vibrational states associated with a given electronic state of the material. The incident photon excites the material system to a virtual state as shown in figure 1.1, and can re-emit a photon of same energy and come to the same vibrational ground state. This is known as elastic scattering or Rayleigh scattering. If the system is excited to a virtual state and emits a photon of different energy, it is inelastic scattering and is known as Raman scattering. The inelastic scattering or Raman scattering process happens in two ways, one is Stokes-Raman scattering and the other one is

anti-Stokes Raman scattering. In Stokes-Raman scattering the energy of the scattered photon is reduced from the energy of the incident photon by an amount equal to the excitation energy of one of the modes of the material with which the photon interacts whereas in anti-Stokes Raman scattering the scattered photon has more energy than the incident photon energy by an amount equal to one of the excitation modes of the material system. The probability of anti-Stokes Raman scattering is much less than Stokes Raman scattering because it depends on the number of molecules present in the excited modes at a given temperature which is given by the Boltzmann distribution.

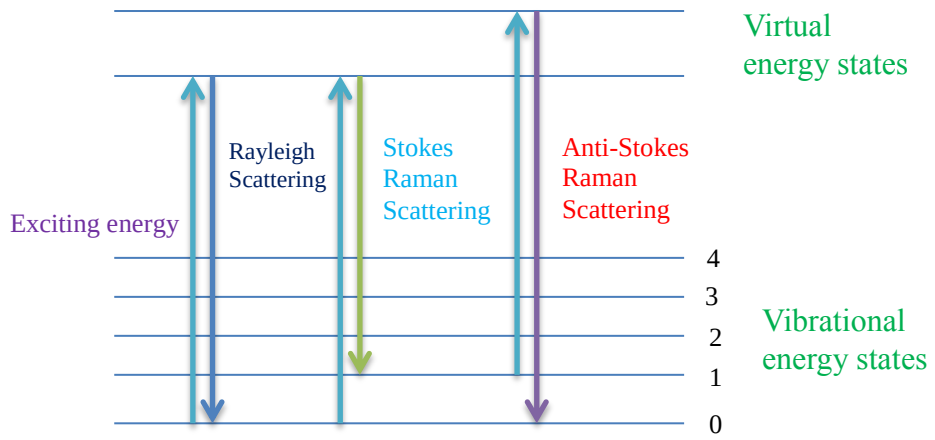


*Figure 1.1: Jablonski diagrams of Rayleigh and Raman scattering processes.*

The shift in energy of the incident photon $(\Delta E)$ is expressed in wavenumbers $(\bar{\nu})$ as

$$\bar{\nu} = \frac{1}{\lambda} = \frac{\Delta E}{hc}$$

A typical Raman spectrum consists of the intensity of the Raman lines as a function of the Raman shift in wavenumbers ($cm^{-1}$) as shown in figure 1.2 which was recorded by us for an amino acid.

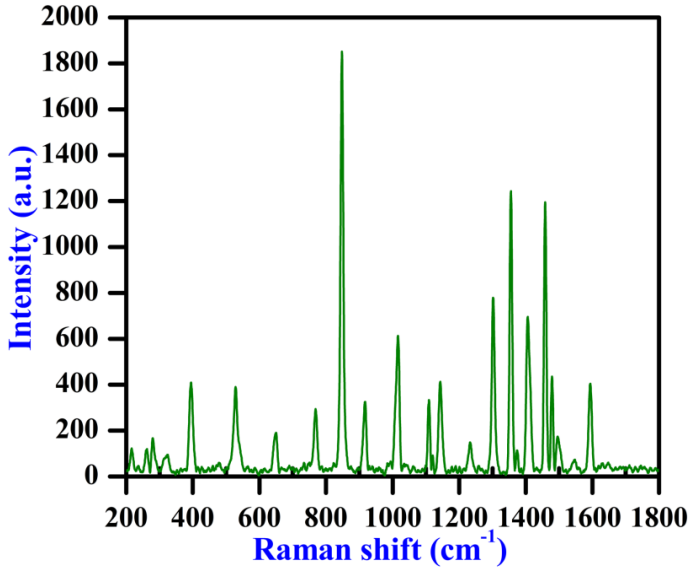


*Figure 1.2: Stokes Raman spectrum of L-Alanine Powder.*

### 1.1.1 Theoretical treatment of Raman scattering:

Raman scattering can be described using both classical and quantum mechanical models [3]. The scattered radiation in both treatments is taken to originate from the oscillating electric and magnetic multipoles induced in the molecules by the elecromagnetic field of the incident light. The dominating multipole is the electric dipole moment and the magnetic diplole and electric quadrupole contributions are much smaller than the electric dipole radiation.

In the classical treatment, the incident radiation as well as the molecular material system is treated classically and the frequency and amplituude of the induced moments are calculated. The time dependence of

the magnitude of electric field strength of an electromagnetic (EM) wave can be expressed as

$$\vec{E} = E_0 \cos(2\pi\nu_0 t) \quad \text{.....1}$$

where $E_0$ is the amplitude and $\nu_0$ is the frequency. If this EM wave is incident on the molecule it produces an induced dipole moment in it, given by:

$$\vec{P} = \alpha \vec{E} = \alpha E_0 \cos(2\pi\nu_0 t) \quad \text{.....2}$$

where $\alpha$ is the polarizability of the molecule. For simplicity let us consider a molecule that is free to vibrate and there is no rotation. If the molecule is vibrating with the freequency $\nu_{vib}$, the nuclear desplacement about the equilibrium position will be:

$$q = q_0 \cos(2\pi\nu_{vib} t) \quad \text{.....3}$$

where $q_0$ is the vibrational amplitude. This nuclear displacement will cause a change in polarizability at the slower frequency $\nu_{vib}$. For small amplitude of vibration $q$, the polarizability α can be expressed in a Taylor series in $q$ as:

$$\alpha = \alpha_0 + \left(\frac{\partial \alpha}{\partial q}\right)_0 q + \quad \text{.....4}$$

Combining equations 1-4 we get

$$\vec{P} = \alpha_0 E_0 \cos(2\pi\nu_0 t) + \left(\frac{\partial \alpha}{\partial q}\right)_0 q_0 E_0 \cos(2\pi\nu_0 t)\cos(2\pi\nu_{vib} t)$$

or

$$\vec{P} = \alpha_0 E_0 \cos(2\pi\nu_0 t) + \frac{1}{2}\left(\frac{\partial\alpha}{\partial q}\right)_0 q_0 E_0 [\cos 2\pi(\nu_0 + \nu_{vib})t + \cos 2\pi(\nu_0 - \nu_{vib})t]$$

.....5

Equation (5) shows that the induced dipole moment has three frequency components: $\nu_0, \nu_0 + \nu_{vib}$ and $\nu_0 - \nu_{vib}$. The first term in the equation represents the dipole moment oscillations at the same frequency as the incident EM wave and gives rise to Rayleigh scattering. The second term is Raman scattering at frequency $\nu_0 + \nu_{vib}$, known as anti-Stokes Raman scattering and the third term represents a Raman scattering frequency of $\nu_0 - \nu_{vib}$ called as Stokes Raman scattering. The phase of the Raman dipole radiations is different from the phase of the incident EM wave. The term $\left(\frac{\partial\alpha}{\partial q}\right)$ represents the Raman activity and molecules for which

$\left(\frac{\partial\alpha}{\partial q}\right) = 0$ are classified as Raman inactive

$\left(\frac{\partial\alpha}{\partial q}\right) \neq 0$ are classified as Raman active

The intensity of radaiation from an oscillating dipole with amplitude $p_0$ and angular frequency ω, at an angle θ relative to the dipole axis is given by

$$I = k_\omega \omega^4 p_0^2 \sin^2\theta, \text{ with } k_\omega = \frac{1}{32}\pi^2 \varepsilon_0 c^3 \text{.....6}$$

Equation (6) thus gives classically the intensity of the Raman scatterred radiations where, $p_0 = \frac{1}{2}\left(\frac{\partial\alpha}{\partial q}\right)_0 q_0 E_0$ and $\omega = 2\pi(\nu_0 - \nu_{vib})$ and $\omega = 2\pi(\nu_0 + \nu_{vib})$ for Stokes and anti-Stokes Raman frequencies from equation (5).

### 1.1.2 Advantages and applications of Raman spectroscopy:

The following are some of the advantages of the Raman Spectroscopic technique over other similar spectroscopic methods:

a) **Specificity**: Raman spectroscopy detects fundamental vibrations of molecules and it has small signal-to-noise ratio and are non-overlapping. This allows a Raman spectrum to use everything from finger printing of molecules to constructing complex chemical models of reaction process.

b) **Analysis of aqueous systems**: IR spectrum of water is strong and relatively complex. IR analyses of aqueous solutions are inadequate due to the strong interference of water bands. Whereas Raman spectrum of water is very weak and unconstructive, so good Raman spectrum of aqueous solutions can be acquired.

c) **Analysis of organic and inorganic chemistries**: Unique Raman signature may be produced if covalent chemical bond exists between chemical species.

d) **Wide concentration range**: The measured Raman intensity is directly proportional to the concentration. This allows a Raman analysis to measure a species concentration from a fraction of 1% to 100% without sample dilution.

e) **No sample preparation**: Particular sample preparation method not required in Raman measurements. It all about incident the Laser light on the sample and collect the scattered photons.

f) **Non-destructive analysis**: Raman measurements are involved by illuminating sample; laser light from the window and collecting the scattered photons. This makes Raman spectroscopy non-destructive.

g) **Compatible with common windows**: It can utilize the sample containers and windows made up of glass, sapphire, transparent polymers and diamond to measure samples in-situ.

h) **Quantitative Raman**: Raman intensity is directly proportional to the number of molecules giving rise to the Raman band, and then Raman band can be used to provide a measure of the concentration of the molecules.

i) **Short measurement times**: Raman spectrum typically can be acquired from a few seconds to minutes. Raman can be used to monitor chemical reactions in real time.

Raman spectroscopy has emerged as an important source for information about molecular structure and dynamics. Raman spectroscopy has many applications in the fields such as in i) art and archeology, ii) biosciences, iii) vibrational studies and analytical chemistry, iv) solid state physics viz. minerals, crystals, glasses, ceramics and etc., v) liquids and liquid interactions, vi) nanomaterials, vii) phase transitions of various kinds, including liquid crystals, viii) pharmaceutical studies, ix) high-pressure physics and chemistry x) forensic science.

Since the change in polarizability with nuclear displacement $\left(\frac{\partial \alpha}{\partial q}\right)$ is small, the effective Raman scattering cross-section is small [4] ($10^{-31}$-$10^{-29}$ $cm^2$/molecule) which hinders the applications of Raman

spectroscopy as an analytical technique. However with techniques such as Surface Enhanced Raman Scatttering (SERS) the Raman scatterring cross section can be significantly enhanced and makes the technique applicable to quantitative analysis as well.

## 1.2 Surface enhanced Raman scattering:

A strong enhancement of the Raman scattering occurs when the scattering molecules are in close proximity (<10 nm) to or adsorbed on a metal surface [5]. This is called Surface Enhanced Raman Scattering (SERS) and was first observed by Fleischmann et al. [6] for adsorption of pyridine on roughened silver (Ag) electrodes. It was thought at first that this enhancement was due to a large surface area available for the molecules but subsequently it was shown by Jeanmaire and Van Duyne [7] and Albrecht and Creighton [8] independently that it was indeed a new phenomenon related to the presence of an enhanced electromagnetic field around the metal surface due to excitation of a surface Plasmon. The most commonly used metals for SERS are Ag and Au, however many other metals have now been used in the SERS measurements viz. Cu, Pt, Hg, Li, Na, K, In, Al, and Rh [9]. Recently some research groups have reported SERS on Ni [10] and Pd [11].

Nowadays there are other techniques related to the SERS/plasmonics, which are: Surface Enhanced Infrared Absorption (SEIRA), Tip Enhanced Raman Spectroscopy (TERS), Transmission Localized Surface Plasmon Resonance Spectroscopy (T-LSPR), Propagating Surface Plasmon Resonance Spectroscopy (P-SPR), Surface Enhanced Fluorescence (SEF) and Surface Enhanced Hyper-Raman Scattering (SEHRS), among many others [12].

However, there is much more interest in SERS due to its great potential for applications. The enhancement in the Raman signal being provided by metal surface resolved the problem of intrinsic inefficiency of the Raman process and brings rich information about the vibrational spectrum of molecules. The combination of sensitivity and selectivity of the technique [13] makes it an ideal technique for chemical sensing applications. SERS also brings the advantage of quenching the fluorescence of molecules near the metal surface.

In general, two mechanisms were proposed to explain the large enhancement of the normal Raman signal viz. electromagnetic (EM) and chemical (CH) enhancement. Electromagnetic enhancement plays a greater role [14-20], whereas chemical enhancement plays a role in some analytes which are chemisorbed on the metal surface and form a complex with metal surface atoms. In addition to large enhancement contribution from the EM if there is a charge transfer both can contribute to increase Raman scattering cross-section [21-25]. Raman scattering cross-section can also be increased when the incident laser wavelength is close to molecular electronic levels. This is known as resonance Raman scattering (RRS). A description about EM, CH enhancement mechanisms and RRS are given in the following sections.

### 1.2.1 Electromagnetic enhancement:

The mobile conduction electrons and the static positive ion cores in a metal constitute plasma and the system has a natural oscillation frequency $\omega_p = \left( \frac{Ne^2}{\varepsilon_0 m_0} \right)^2$ called the plasma frequency, where $N$ is the number of

conduction electrons per unit volume, $e$ is the electron charge, $m_0$ is the electron mass and $\varepsilon_0$ is the free space permittivity [26]. This is a longitudinal plasma oscillation mode of the electron gas caused by a collective displacement of the electrons against the positive ion cores that provide a restoring force for the electrons and a longitudinal oscillation mode of the electron gas sets in. Quanta of these oscillations are called plasmons.

At the plasma frequency the dielectric constant of the system also goes over from a negative value to a positive value since the frequency dependence of the dielectric constant of undamped free electron plasma is given by [27]: $\varepsilon_r(\omega) = 1 - \frac{\omega_p^2}{\omega^2}$. The plasma frequency $\omega_p$ lies in the ultraviolet (UV) frequency region for metals and frequencies more than the plasma frequencies are transmitted by the free electron plasma ($\varepsilon_r$ is real). In the interesting optical region below UV, the dielectric constant is negative and the electromagnetic waves ideally do not exist inside the metal. However this is the situation for an ideal metal with infinite electrical conductivity where the electrons do not undergo any damping in the medium at any frequency. The conductivity of a real metal is finite and frequency dependent due to finite relaxation time for the electrons in the metal. The electromagnetic waves therefore exist inside the metal to a small distance. This is responsible for the important properties of absorption and scattering of the electromagnetic waves by a metal.

The frequency dependent conductivity of a metal in the presence of a damping constant $\beta$ (where $\beta = \frac{1}{\tau}$, $\tau$ is the relaxation time) is given by [28]

$$\sigma(\omega) = \frac{\omega_p^2 \varepsilon_0}{(\beta - i\omega)} \quad \text{.....7}$$

and the complex frequency dependent dielectric constant of the metal is given by:

$$\varepsilon(\omega) = 1 - \frac{\omega_p^2}{\omega(\omega + i\beta)} \quad \text{.....8}$$

The real and imaginary parts of the dielectric constant determine the behavior of the electromagnetic fields inside the metal. The real and imaginary parts of $\varepsilon(\omega)$ are

$$\mathrm{Re}\,\varepsilon(\omega) = 1 - \frac{\omega_p^2}{(\omega^2 + \beta^2)^2} \quad \text{.....9}$$

$$\mathrm{Im}\,\varepsilon(\omega) = \frac{\omega_p^2 \beta}{\omega(\omega^2 + \beta^2)} \quad \text{.....10}$$

Longitudinal oscillations at the plasma frequency mentioned above are natural oscillations of the system and are also called as bulk plasma oscillations or bulk plasmons after quantization of the oscillations. However since these are longitudinal modes they do not couple to the electromagnetic waves. Later Ritchie [29] showed that on the surface of thin films of metal on a dielectric medium there are surface modes which are propagating at the metal dielectric interface in the presence of an electromagnetic field. These coupled modes of the Plasmon and EM waves are more generally known as Plasmon-Polaritons as they exist due to the interaction of light with plasma. These are depicted schematically in figure 1.3 which shows charge density oscillations along the direction of

propagation of the surface plasmon-polariton. However if the geometry is confined to zero dimensions as for a metallic particle on a dielectric medium, these modes are called localized surface plasmons polaritons (LSPP) or also sometimes just LSP, as shown in figure 1.4.

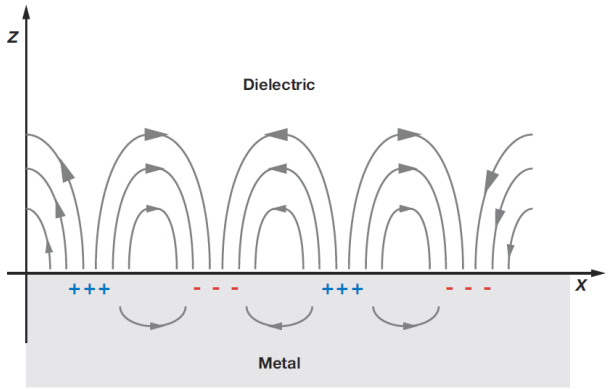


*Figure 1.3 Schematic representation of propagating surface plasmon modes at a metal dielectric interface.*

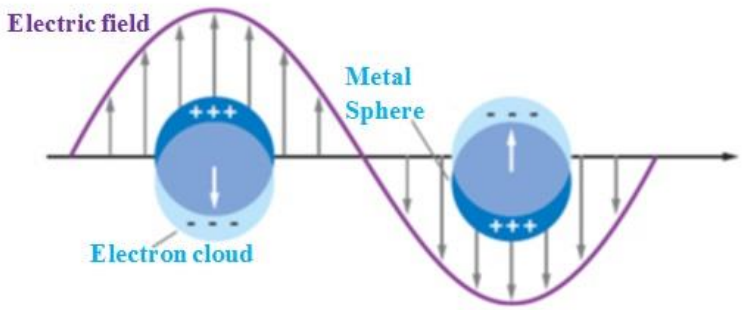


*Figure 1.4 Schematic representations of localized surface plasmon modes.*

A general treatment of Surface Enhanced Raman Spectroscopy and applications for various types of nanostructures is given in detail in many monographs [4, 10, 30, 31]. In the present work, the substrates used for Surface Enhanced Raman Scattering (SERS) studies comprise of metal nanoclusters deposited on a dielectric medium and the concept of localized

surface Plasmons is applicable to our systems. We therefore discuss briefly the electric field enhancement and Raman signal enhancement effects due to localized surface Plasmons, which bring out the basic principles involved in SERS measurements.

When an electromagnetic wave is incident on a metallic nanocluster the electric field of the incident wave is drastically modified by the Localized Surface Plasmon (LSP) in the nanocluster and more so at the resonant frequency of the LSP. The local electric field, $\vec{E}_{loc}$ at the molecule position that is adsorbed on the metal surface is therefore different from the incident field of the electromagnetic wave, $\vec{E}_{inc}$ in magnitude as well as direction and also depends on the distance from the surface. The dipole moment induced in the Raman molecule is proportional to this enhanced $\vec{E}_{loc}$ and therefore an enhancement of the Raman signal is observed. As shown earlier (equation 6) the Raman intensity is proportional to the square of the electric field amplitude at the Raman molecule and hence, one defines a local field intensity enhancement factor (EF) to quantify the Raman signal as:

$$I_{EF} = \frac{E_{loc}^2}{E_{inc}^2} \quad \text{.....11}$$

For the sake of completeness and to understand the work presented in this thesis, we consider here a simple model of a metallic nanoparticle on the surface of a dielectric to bring out the salient features of the local electric field enhancement effect. This is also the relevant model for our SERS substrates used in this work. The study of this problem is usually made under the following plausible approximations.

i) Electrostatic field approximation (EFA): One assumes that the size of the nanoparticle is small as compared to the wavelength of the incident electromagnetic wave. The electric field variation over the size of the nanoparticle can be ignored and the nanoparticle can be assumed to lie in an electric field of constant amplitude. This approximation may actually hold only for very small size nanoparticles but the essential features for a bigger size particle would also be reproduced by this model to some extent.

ii) The electric field at a point near the surface of the nanoparticle is considered as the sum of the incident field and the field arising out of the polarization of the nanoparticle in the presence of the external field.

iii) The nanoparticle is assumed to predominantly have a dipole radiation field from the induced polarization.

iv) The frequency dependence of the electromagnetic field is introduced by taking the dielectric constant of the metal sphere to be frequency dependent as $\varepsilon(\omega)$ in a medium of dielectric constant $\varepsilon_m$.

The electric field inside a nanoparticle $\vec{E}_{in}$ is then given by (J.D. Jackson 1999 [32]):

$$\vec{E}_{in} = \left[1 - \left(\frac{\varepsilon(\omega) - \varepsilon_m}{\varepsilon(\omega) + 2\varepsilon_m}\right)\right]\vec{E}_{inc} \quad \text{.....12}$$

The polarization of the particle relative to the medium $\vec{P}_m = \varepsilon_0(\varepsilon(\omega) - \varepsilon_m)\vec{E}_{inc}$ is then

$$\vec{P}_m = 3\varepsilon_0\varepsilon_m\left(\frac{\varepsilon(\omega)-\varepsilon_m}{\varepsilon(\omega)+2\varepsilon_m}\right)\vec{E}_{inc} \quad \text{.....13}$$

The dipole moment of the nanoparticle of volume $\frac{4}{3}\pi a^3$ ('a' is the radius of the particle) is therefore given by $\vec{P} = \frac{4}{3}\pi a^3 \vec{P}_m$ and the polarizability $\alpha$ defined by $\vec{P} = \alpha \vec{E}_{inc}$ is given by

$$\alpha = 4\pi a^3 \varepsilon_0 \varepsilon_m \left(\frac{\varepsilon(\omega)-\varepsilon_m}{\varepsilon(\omega)+2\varepsilon_m}\right) \quad \text{.....14}$$

If $\vec{E}_p$ is the dipole field near the surface of the particle produced by the dipole moment $\vec{P}$ of the particle, the total electric field near the particle surface would be

$$\vec{E}_{loc} = \vec{E}_{inc} + \vec{E}_p \quad \text{.....15}$$

The electric field at a general point $x$ due to a dipole $p$ situated at a point $x^1$ is given by

$$\vec{E}_p = \frac{1}{4\pi\varepsilon_0}\frac{\left[3\vec{n}\left(\vec{n}.\vec{p}\right)-\vec{p}\right]}{r^3} \quad \text{.....16}$$

where $\vec{n}$ is a unit vector in the direction of $\vec{x}-\vec{x}^1$ and $\vec{r} = \left|\vec{x}-\vec{x}^1\right|$ is the distance between the dipole and the point $\vec{x}$. To get a simplified result for the purpose of illustration of the electric field enhancement, we consider the

incident electric field along the $Z$ - axis and also consider a point along the $Z$ - axis at a distance $u$ from the center where the particle is centered. The electric field due to polarization dipole moment $\left(\vec{P}\right)$ of the particle (which is also along the $Z$ - axis) would be

$$\vec{E}_p = \frac{2\alpha \vec{E}_{inc}}{4\pi u^3} = 2a^3\varepsilon_m\left(\frac{\varepsilon(\omega)-\varepsilon_m}{\varepsilon(\omega)+2\varepsilon_m}\right)\frac{\vec{E}_{inc}}{u^3} \quad \text{.....17}$$

And the total electric field at a point at a distance $u$ from the center of the particle would be

$$\vec{E}_{loc} = \left[1+2\frac{a^3}{u^3}\varepsilon_m\left(\frac{\varepsilon(\omega)-\varepsilon_m}{\varepsilon(\omega)+2\varepsilon_m}\right)\right]\vec{E}_{inc} \quad \text{.....18}$$

At $u = a$,

$$\vec{E}_{loc} = \left[1+2\varepsilon_m\left(\frac{\varepsilon(\omega)-\varepsilon_m}{\varepsilon(\omega)+2\varepsilon_m}\right)\right]\vec{E}_{inc} \quad \text{.....19}$$

In the above equation if we write

$$\eta = \left[\frac{\varepsilon(\omega)-\varepsilon_m}{\varepsilon(\omega)+2\varepsilon_m}\right] \quad \text{.....20}$$

The important resonance characteristics of the local field can be discussed in terms of the frequency dependence of $\eta$:

i) The condition for resonance to occur is $\mathrm{Re}\,\varepsilon(\omega) = -2\varepsilon_m$ which gives the resonance frequency as $\omega = \frac{\omega_p}{\sqrt{1+2\varepsilon_m}}$, i.e. the resonance

frequency is shifted to lower than the ultraviolet plasma frequency $\omega_p$.

ii) The red shift is larger for larger values of the dielectric constant of the medium but it does not depend on the radius of the particle in the electrostatic approximation.

At the resonant frequency $|\eta|^2 = 1 + \frac{9\varepsilon_m^2}{[\mathrm{Im}\,\varepsilon(\omega)]^2}$ and the resonance will be large if the dissipation term of the metal dielectric constant $(\mathrm{Im}\,\varepsilon(\omega))$ is small. The enhancement factor defined in equation 11 would be:

$$I_{EF} = \left|\frac{E_{loc}}{E_{inc}}\right|^2 = 1 + 4\varepsilon_m^2\left[1 + \frac{9\varepsilon_m^2}{[\mathrm{Im}\,\varepsilon(\omega)]^2}\right] \quad \text{.....21}$$

We will now estimate the resonance frequency and the enhancement factor using the experimentally measured real and imaginary part of the dielectric function of silver (shown in figure 1.5) which is taken from Johnson and Christy's data [33].

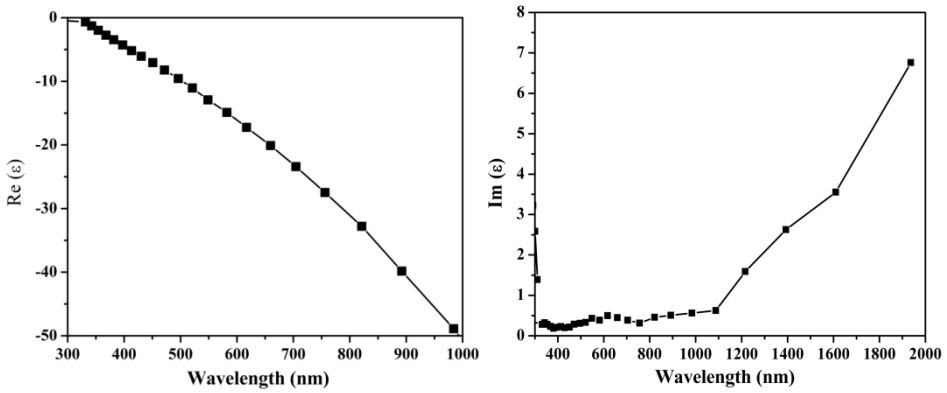


*Figure 1.5: Real and imaginary part of dielectric function of Silver as a function of wavelength [from 33].*

Surface Plasmon peaks which appear in our experimental data of Ag nanoclusters deposited on different substrates are shown in table 1.1 (the results are discussed in chapter 4). These are compared with the estimated values of resonance frequency using Johnson and Christy's experimental data for $\mathrm{Re}\,\varepsilon(\omega)$.

*Table 1.1: Plasmon resonance peak comparison with estimates using Johnson and Christy's data [33].*

| Substrate on which Ag nano clusters were deposited | Observed Plasmon peak | Plasmon peaks estimated using $\mathrm{Re}\,\varepsilon(\omega)$ data of Johnson and Christy |
|---|---|---|
| Glass | 470 nm | 486 nm |
| Alumina | 414 nm | 432 nm |
| Si | 400 nm | 460 nm (using $\mathrm{Re}\,\varepsilon(\omega)$ of $SiO_2$) 704 nm (using $\mathrm{Re}\,\varepsilon(\omega)$ of Silicon) |

From the table we can say that Plasmon frequencies for Ag nanoclusters on glass and alumina substrates are in good agreement with the estimates from Johnson and Christy's data whereas the observed frequency for Si is in better agreement with the estimates using the dielectric constant of $SiO_2$ rather than the Si. This is expected because the surface of Si tends to develop a small oxide layer when exposed to air.

The electromagnetic enhancement factors were estimated using equation 21 and the experimental values of $(\mathrm{Im}\,\varepsilon(\omega))$ from Johnson and Christy (figure 1.5). The estimated electromagnetic enhancement factors for glass, alumina and $SiO_2$ are $1 \times 10^5$, $8 \times 10^4$ and $1 \times 10^5$, respectively.

### 1.2.2 Chemical enhancement:

The other enhancement mechanism which occurs in SERS is chemical enhancement (CE) and this requires the analyte to be chemically bound to the SERS substrate. It is basically related to electronic properties of adsorbed molecule. Two kinds of chemical enhancement processes are possible, one is Raman scattering cross-section enhancement due to polarizability changes by adsorption of molecule and other the one is photo-driven charge transfer (CT) between metal substrate and adsorbed molecule [6]. Charge transfer is considered to be as a Resonance Raman like enhancement. Schematic representation of CT mechanism is shown in figure 1.6.

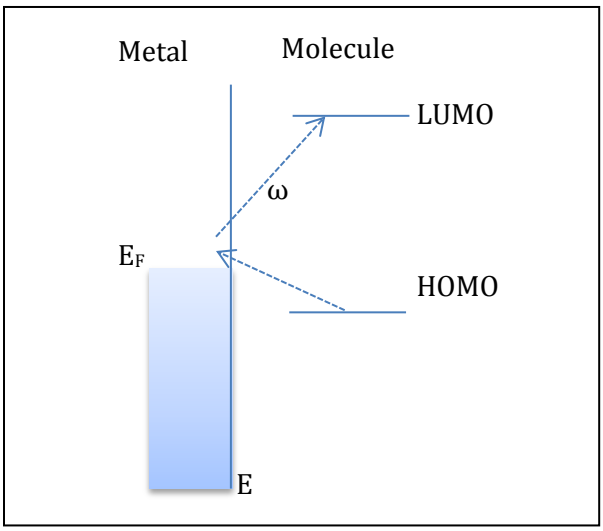


*Figure 1.6: Schematic representation of Charge Transfer (CT) mechanism.*

The CT can occur from the Fermi energy level of metal to lowest unoccupied molecular orbital (LUMO) of the adsorbed molecule or from highest occupied molecular orbital (HOMO) of adsorbed molecule to the

Fermi energy of the metal. CE is also associated with the bond strength between adsorbed molecules and the metal atoms at the surface active sites. The molecules which have high affinity to metals will adsorb on it and have greater enhancement.

CE brings changes in the SERS spectrum viz. frequency shift and relative intensity of the spectral bands. The contribution in the enhancement factor from the CE enhancement (typically 1-3 orders of magnitude) is smaller as compared to the EM enhancement [34].

### 1.3 Resonance Raman scattering:

When the excitation laser light frequency falls within an electronic absorption band of a molecule, resonance will occur, which enhances the intensity of some Raman lines and is called Resonance Raman Scattering (RRS). This is shown schematically in the figure 1.7.

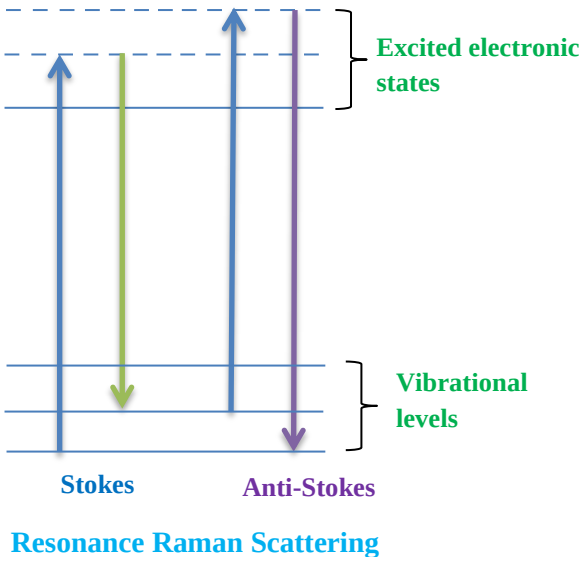


*Figure 1.7: Schematic representations of resonant Raman effects.*

## 1.4 SERS substrates:

Methods of preparation of SERS-active substrates are active field of research. SERS substrates with uniformity and high enhancement factors are important for practical application. The SERS active substrates are classified into three main categories: (i) metal nanoparticle in colloidal solutions (ii) metal electrodes and (iii) metal nanoparticles on planar substrates. Metal electrodes were used in the early development of SERS in fact, orders of magnitude enhancement of normal Raman signal was observed on the Ag electrode [6]. Later on, their importance was diminished due to not much enhancement achievable as compared to other methods. Most of the methods are aimed at preparing nanoparticles which can show high enhancement factors. Mostly Ag and Au nanoparticles are used in SERS as these are the metals that have optical properties which can support Plasmon resonances in the visible and near infrared wavelengths which are of interest to SERS [35]. The Ag and Au nanoparticles can be prepared in colloidal form with different chemical routes [36, 37] or by laser ablation [38, 39]. Other methods to prepare substrates are by roughening the metallic surfaces by means of etching. Nanolithography is another method to produce uniform and reproducible SERS substrates. In this method structure of the substrate is controlled by lithography techniques. This provides an opportunity to match the experimental results with theoretical predictions because of high degree of control of substrate structure [40]. Focused Ion beam milling and electron beam nanolithography were mostly used in nanolithography techniques [41, 42]. In the present thesis we have used DC magnetron sputtering technique which produces contamination-free metal

nanoparticles. The techniques of substrate preparation used in this work are given in chapter 2.

### 1.5 SERS applications:

SERS has overcome the intrinsic limitation of low Raman scattering cross-section by enhancing the Raman signal which makes enables the possibility to carry out ultrasensitive measurements with this technique. SERS is a versatile spectroscopic technique tool for identification and structural characterization of molecules [4, 43]. SERS has applications in the field of analytical chemistry [44-48], biological sciences [49, 50], explosive identification and monitoring [51], forensic science [52], biomedical diagnostic e.g. cancer diagnostic [53], target detecting (e.g. DNA [54], protein [55] and bacteria [56, 57]), art and archeology [58] and glucose detection [59].

### 1.6 Thesis outline:

Objective of the present thesis was to prepare reproducible, sensitive SERS-active substrates with high enhancement factors and quantitative detection of molecules and bio-molecules using these substrates.

The thesis is organized as follows:

After having given a basic introduction to Surface Enhanced Raman Scattering (SERS) and explaining the enhancement mechanisms for SERS in Chapter 1, we describe in Chapter 2, the working principles of the experimental techniques used in the thesis viz. Nano-cluster Deposition system, tubular furnace, field emission scanning electron microscopy

(FESEM), atomic force microscopy (AFM), glove box, UV-Vis spectrophotometer and micro-Raman spectrometer.

In chapter 3, we describe the preparation methods of the SERS substrates by deposition of silver nanocluster films and the optimization of nanocluster deposition time and annealing temperature to get the best SERS substrates. We also discuss the sensitivity and reproducibility of the substrates. In order to get optimum distance between the clusters, Ag nanoclusters on glass substrates were deposited for 7, 8, 9 and 10 minute deposition times. To find the optimum deposition time and annealing temperature through SERS, we used Rhodamine 6G (R6G) and Crystal Violet (CV) dyes as probe molecules. Aqueous solutions of these analytes in the range $10^{-3}$ M-$10^{-18}$ M concentrations were prepared by sequential dilution method. We have chosen characteristic Raman lines of these dye molecules as reference lines to compare the sensitivity of these substrates. We observed that 8 minutes deposited substrates annealed at 300 $^{o}$C gave the best SERS signals. Further measurements were carried out with these optimum preparation conditions. The dye molecules R6G and CV could be detected up to $10^{-16}$ M and 3.2x$10^{-18}$ M concentrations respectively and the enhancements factors for these dye molecules were ~$10^{12}$. The intensities of the characteristic lines were plotted as a function of molar concentration of the analytes which resulted in a good linear relationship between intensity and molar concentration. The substrates were also highly reproducible.

SERS intensity depends on the size, shape and inter particle separation of metal nanoparticles. The dielectric constant of the substrate also influences the signal. So we have chosen three different dielectric substrates viz. glass, silicon and alumina. Ag nanoclusters were deposited on

these substrates and annealed at 300 ºC for 2 hours in the presence of argon atmosphere. The SERS efficiencies of these substrates were evaluated with Rhodamine B (RhB) dye molecule. We observed that the SERS signal intensity on glass substrate was more as compared to the other substrates. The uniformity of the substrates was measured by calculating relative standard deviation of intensities of Raman lines. The above aspects are covered in Chapter 4 of the thesis.

In chapter 5, we discuss the applications of our sensitive and reproducible SERS-active substrates in glucose sensing. In order to measure the blood glucose levels in diabetic patients one needs to draw blood from patients body which is a painful procedure. However, studies have also detected presence of glucose in the urine and saliva samples of diabetic patients. So there is an urgent need to develop non-invasive or minimally invasive methods for frequent glucose monitoring. Accurate quantitative detection and evaluation of glucose has not been possible from urine and saliva samples due to lack of a sensitive and molecule specific method. We show here that it is possible in principle to detect quantitatively glucose levels in aqueous glucose solutions at very low level in the micro-molar concentration range.

SERS detection of glucose is limited by two factors. One factor is the low Raman scattering cross-section of the glucose molecule and the second one is the poor affinity of glucose molecules to be adsorbed on metal surfaces. Many approaches have been taken to address the aforementioned challenges. Van Duyne's group came up with the idea to modify the metal surface chemically with alkane thiol so that the alkane molecules sticking out of the metal surface form a partition layer that traps the glucose

molecule close to the metal surface. In this work we have adopted a new method wherein 2-Thienylboronic acid was used as a linker molecule that attaches directly to both the metal surface and to the glucose molecule without any other intermediate molecule for functionalization. A new intense Raman line was observed at 986 $cm^{-1}$ in the SERS spectrum. The intensity of this line was used to quantify the D-glucose concentration in the molar concentration range of 1 to 500 micromoles. A good correlation was observed between the intensity of the Raman line and molar concentration of D-glucose. This result can be very significant in developing a sensor for non-invasive detection of glucose in diabetic patients using the urine or saliva samples. A patent application (3146/CHE/2015) has been filed for this work.

Chapter 6 describes SERS measurements on L-amino acids. Amino acids are the basic structural units of proteins and enzymes. In order to understand the protein interaction on metal nanoparticle surface, it is necessary to have a fundamental understanding of the individual amino acid interaction with metal nanoparticle surfaces. In this chapter, we describe the SERS measurements of 19 L-amino acids and suggest a method for quantitative analysis. A linear correlation was found between intensities of the characteristic Raman lines and molar concentrations of the amino acids. These results would have promising applications in detection of these amino acids in more complex molecules. The 19 L-amino acids studied were L-Phenylalanine (L-Phe), L-Tryptophan (L-Trp), L-Tyrosine (L-Tyr), L-Alanine (L-Ala), L-Glycine (L-Gly), L-Isoleucine (L-ILe), L-Leucine (L-Leu), L-Proline (L-Pro), L-Valine (L-Val), L-Aspartic acid (L-Asp), L-Glutamic acid (L-Glu), L-Arginine (L-Arg), L-Histidine (L-His), L-Lysine (Lys), L-Serine (L-Ser), L-

Threonine (L-Thr), L-Methionine (L-Met)], L-Asparginine (L-Asn) and L-Glutamine (L-Gln).

Chapter 7 gives the scope of future work arising out of this thesis.

**References:**

[1] C.V. Raman and K.S. Krishnan, "A new type of secondary radiation" *Nature 121 (1928) 501.*

[2] R.S. Krishnan and R.K. Shankar, "Raman effect: history of the discovery" *J. Raman Spectrosc. 10 (1981) 1.*

[3] J.R. Ferraro, K. Nakamoto and C.W. Brown. *Introductory Raman spectroscopy. Academic Press, 2003.*

[4] K. Kneipp, H. Kneipp, I. Itzkan, R.R. Dasari and M.S. Feld, "Surface enhanced Raman scattering and biophysics" *J. Phys: Condens. Matter 14 (2002) R597.*

[5] Raju Botta, G. Upender, R. Sathyavathi, D. Narayana Rao and C. Bansal, "Silver nanocluster films for single molecule detection using Surface Enhanced Raman Scattering (SERS)" *Mater. Chem. Phys. 137 (2013) 699.*

[6] P.J. Hendra, M. Fleischmann and A.J. MecQuillan, "Raman spectra of pyridine adsorbed at a silver electrode" *Chem. Phys. Lett. 26 (1974) 163.*

[7] D.L. Jeanmaire and R.P. Van Duyne, "Surface Enhanced Spectroelctrochemistry Part I Hetero cyclic, Aromatic, and Aliphatic Amines adsorbed on the Anodized Silver Electrode" *J. Electroanal. Chem. 84 (1977) 1.*

[8] M.G. Albrecht and J.A. Creighton, "Anomalously Intense Raman Spectra of Pyridine at a Silver Electrode" *J. Am. Chem. Soc. 99 (1977) 5215.*

[9] M. Moskovits, "Surface-enhanced spectroscopy" *Rev. Mod. Phys. 57 (1985) 783.*

[10] G. Sauer, G. Brehm, S. Schneider, H. Graener, G. Seifert, K. Neilsch, J. Choi, P. Goring, U. Gosele, P. Miclea and R.B. Wehrspohn, "Surface-enhanced Raman spectroscopy employing monodisperse nickel nanowire arrays" *Appl. Phys. Lett. 88 (2006) 023106.*

[11] H. Guo, L. Ding, T. Zhang and Y. Mo, "4-Mercaptopyridine adsorbed on pure palladium island films: A combined SERS and DFT investigation" *J. Mol. Struct. 1035 (2013) 231.*

[12] R. Aroca, Surface-enhanced vibrational spectroscopy. John Wiley and Sons, Chichester, (2006).

[13] G. Upender, R. Satyavathi, B. Raju, K. Shadak Alee, D. Narayana Rao and C. Bansal, 'Silver cluster films as novel SERS substrates for ultrasensitive detection of molecules' *Chem. Phys. Lett. 511 (2011) 309.*

[14] M. Moskovits, "Surface roughness and the enhanced intensity of Raman scattering by molecules adsorbed on metals" *J. Chem. Phys. 69 (1978) 4159.*

[15] J. Gersten and A. Nitzan, "Electromagnetic theory of enhanced Raman scattering by molecules adsorbed on rough surfaces" *J. Chem. Phys. 73 (1980) 3023.*

[16] M. Inoue and K. Ohtaka, "Surface Enhanced Raman Scattering by Metal Spheres. I. Cluster Effect" *J. Phys. Soc. Jpn. 52 (1983) 3853.*

[17] F.J. Garcia-Vidal and J.B. Pendry "Collective Theory for Surface Enhanced Raman Scattering" *Phys. Rev. Lett. 77 (1996) 1163.*

[18] H. Xu, J. Aizpurua, M. Käll and P. Apell "Electromagnetic contributions to single-molecule sensitivity in surface-enhanced Raman scattering" *Phys. Rev. E 62 (2000) 4318.*

[19] S. Corni and J. Tomasi, ‘‘Surface enhanced Raman scattering from a single molecule adsorbed on a metal particle aggregate: A theoretical study’’ *J. Chem. Phys. 116 (2002) 1156*

[20] K. Li, M.I. Stockman and D.J. Bergman “Self-Similar Chain of Metal Nanospheres as an Efficient Nanolens” *Phys. Rev. Lett. 91 (2003) 227402.*

[21] A.M. Michaels, M. Nirmal and L.E. Brus “Surface Enhanced Raman Spectroscopy of Individual Rhodamine 6G Molecules on Large Ag Nanocrystals” *J. Am. Chem. Soc. 121 (1999) 9932.*

[22] B.N.J. Persson, “On theory of Surface-enhanced Raman Scattering” *Chem. Phys. Lett. 82 (1981) 561.*

[23] B. Pettinger, “Light scattering by adsorbates at Ag particles: Quantummechanical approach for energy transfer induced interfacial optical processes involving surface plasmons, multipoles, and electronhole pairs” *J. Chem. Phys. 85 (1986) 7442.*

[24] A. Otto, T. Bornemann, Ü. Ertürk, I. Mrozek and C. Pettenkofer “Model of electronically enhanced Raman scattering from adsorbates on cold-deposited silver” *Surf. Sci. 210 (1989) 363.*

[25] A. Otto “What is observed in single molecule SERS, and why?” *J. Raman Spectrosc. 33 (2002) 593.*

[26] Chapter 14, Introduction to solid State Physics, by C. Kittel, VIII Edition.

[27] Optical Properties of Solids by Mark Fox, Oxford University Press, New York, 2001, p 181.

[28] Principles of Optics by Max Born and Emil Wolf, p 750.

[29] R.H. Ritchie, “Plasma Losses by Fast Electrons in Thin Films” *Phys. Rev. 106 (1957) 874.*

[30] P.L. Stiles, J.A. Dieringer, N.C. Shah and R.P. Van Duyne, "Surface-Enhanced Raman Spectroscopy" *Annu. Rev. Anal. Chem. 1 (2008) 601.*

[31] S. Schluker, "Surface-Enhanced Raman Spectroscopy: Concepts and Chemical Applications" *Angew. Chem., Int. Ed., 53 (2014) 4756.*

[32] Classical Electrodynamics by J.D. Jackson, 3rd edition, 1999.

[33] P.B. Johnson and R.W. Christy, "Optical Constants of the Noble Metals" *Phys. Rev. B 6 (1972) 4370.*

[34] Linlin, L. Jenson, G.C. Schatz, "Pyridine Ag-20 Cluster: A Model System for Studying Surface-Enhanced Raman Scattering" *J. Am. Chem. Soc. 128 (2006) 2911.*

[35] E.C. Le Ru and P.G. Etchegoin, *Principles of Surface-Enhanced RamanSpectroscopy and Related Plasmonic Effects*. Elsevier, 2009.

[36] J.A. Creighton, C.G. Blatchford and M.G. Albrecht "Plasma resonance enhancement of Raman scattering by pyridine adsorbed on silver or gold sol particles of size comparable to the excitation wavelength" *J. Chem. Soc., Faraday Transactions 75 (1979) 790.*

[37] P.C. Lee and D. Meisel, "Adsorption and surface-enhanced Raman of dyes on silver and gold sols" *J. Phys. Chem. 86 (1982) 3391.*

[38] A. Henglein, "Physicochemical properties of small metal particles in solution:"microelectrode" reactions, chemisorption, composite metal particles, and the atom-to-metal transition" *J. Phys. Chem. 97 (1993) 5457.*

[39] M. Prochazka, J. Stepaneka, B. Vickova, I. Srnova and P. Maly "Laser ablation: Preparation of "chemically pure" Ag colloids for surface enhanced Raman scattering spectroscopy" *J. Mol. Struct. 410 (1997) 213.*

[40] E.C. Le Ru, P.G. Etchegoin, J. Grand, N. Felidj, J. Aubard, G. Levi, A. Hohenau and J. Krenn, "Surface enhanced Raman spectroscopy on nanolithography-prepared substrates" *Current App. Phys. 8 (2008) 467.*

[41] N. Felidj, J. Aubard, G. Lvi, J.R. Krenn, M. Salerno, G. Schider, B. Lamprecht, A. Leitner and F.R. Aussenegg, "Controlling the optical response of regular arrays of gold particles for surface-enhanced Raman scattering" *Phys. Rev. B 65 (2002) 075419.*

[42] A.G. Brolo, E. Arctander, R. Gordon, B. Leathem and K.L. Kavanagh, "Nanohole-Enhanced Raman scattering" *Nano Lett. 4 (2004) 2015.*

[43] S.M. Nie and S.R. Emory, 'Probing single molecules and single nanoparticles by Surface-Enhanced Raman Scattering' *Science 275 (1997) 1102.*

[44] R. Aroca, Surface enhanced vibrational spectroscopy, Wiley, Hoboken, NJ, 2006.

[45] J.P. Camden, J.A. Dieringer, J. Zhao and R.P. Van Duyane, "Controlled plasmonic nanostructures for Surface-Enhanced spectroscopy and sensing" *Acc. Chem. Res. 41 (2008) 1653.*

[46] G.A. Baker, D.S. Moore, "Progress in plasmonic engineering of surface-enhanced Raman-scattering substrates toward ultra-trace analysis" *Anal. Bioanal. Chem. 382 (2005) 1751.*

[47] M. Moskovits, "Surface-enhanced Raman spectroscopy: a brief retrospective" *J. Raman Spectrosc. 36 (2005) 485.*

[48] M.D. Porter, R.J. Lipert, L.M. Siperko, G. Wang and R. Narayana, "SERS as a bioassay platform: fundamentals, design, and application" *Chem. Soc. Rev. 37 (2008) 1001.*

[49] S.Q. Liu and Z.Y. Tang, "Nanoparticle assemblies for biological and chemical sensing" *J. Mater. Chem. 20 (2010) 24.*

[50] Y. Wang, J. Irudayaraj, "Surface-Enhanced Raman Spectroscopy at Single-Molecule Scale and Its implications in Biology" *Phil. Trans. R. Soc. B 368 (2013) 20120026.*

[51] M.K.K. Oo, C.F. Chang, Y. Sun, X. Fan, "Rapid, sensitive DNT vapour detection with UV- assisted photo-chemically synthesized gold nanoparticle SERS substrates" *Analyst 136 (2011) 2811.*

[52] S. Boyd, M.F. Bertino, D. Ye, L.S. White and S.J. Seashols, "Highly sensitive detection of blood by Surface enhanced Raman Scattering" *J. Forensic. Sci. 58 (2013) 753.*

[53] X.M. Qian, X.H. Peng, D.O. Ansari, Q. Yin-Goen, G.Z. Chen, D.M. Shin, L. Yang, A.N. Young, M.D. Wang and S.M. Nie, "In vivo tumor targeting and spectroscopic detection with surface-enhanced Raman nanoparticle tags" *Nat. Biotechnol. 26 (2008) 83.*

[54] A.J. Bonham, G. Braun, I. Pavel, M. Moskovits and N.O. Reich, "Detection of sequence-specific protein-DNA interactions via surface enhanced Resonance Raman scattering" *J. Am. Chem. Soc. 129 (2007) 14572.*

[55] J.K. Daniels and G. Chumanov, "Nanoparticle-mirror sandwich substrates for surface-enhaced Raman scattering" *J. Phys. Chem. B 109 (2005) 17936.*

[56] H.W. Cheng, S.Y. Huan, H.L. Wu, G.L. Shen and R.Q. Yu, "Surface-enhanced Raman spectroscopic detection of a bacteria biomarker using gold nanoparticle immobilized substrates" *Anal. Chem. 81 (2009) 9902.*

[57] R.M. Jarvis, A. Brooker and R. Goodacre, "Surface-enhanced Raman Scattering for the rapid discrimination of bacteria" *Faraday Discuss. 132 (2006) 281.*

[58] Marco Leona 'Surface enhanced Raman scattering in art and archeology' *Proc. SPIE 5993, Advanced Environmental, Chemical, and Biological sensing Technologies III, 59930L.*

[59] D.A. Stuart, J.M. Yuen, N. Shah, O. Lyandres, C.R. Yonzon, M.R. Glucksberg, J.T. Walsh and R.P. Van Duyne, "In vivo glucose measurement by Surface-enhanced Raman spectroscopy" *Anal. Chem. 78 (2006) 7211.*

# Chapter 2

# Experimental Techniques

## 2.1 Introduction:

The present chapter gives the details of experimental methodology involved in this doctoral work. We discuss the sample preparation methods used for making the Surface enhanced Raman scattering (SERS) substrates, the sample characterization techniques, and the SERS measurements and data analysis methods.

## 2.2 Nanocluster deposition system:

As discussed in the previous chapter the technique of SERS requires the adsorption of the analyte molecule near the surface of a metal particle. We have used for the first time SERS substrates consisting of silver nanocluster films prepared by a nanocluster deposition system (Nanodep60 from Oxford Applied Research, UK), originally designed by Haberland [1, 2]. This system is mainly designed for the preparation of nanocluster (NC) films under ultra-high vacuum (UHV) conditions and works on the principle of inert gas phase condensation method. The NC deposition system is built around a nanocluster source (NC200U) which is comprised of a DC magnetron and aggregation chamber. The NC deposition system also has the deposition chamber or main chamber, a DC ion source, sources for internal bake out and pumping, an EPICentre substrate holder, pressure gauges and mass flow controllers. The block diagram of the NC deposition system is shown in figure 2.1. Description about nanocluster source,

deposition chamber and operation of the nanocluster deposition is given in the following sections.

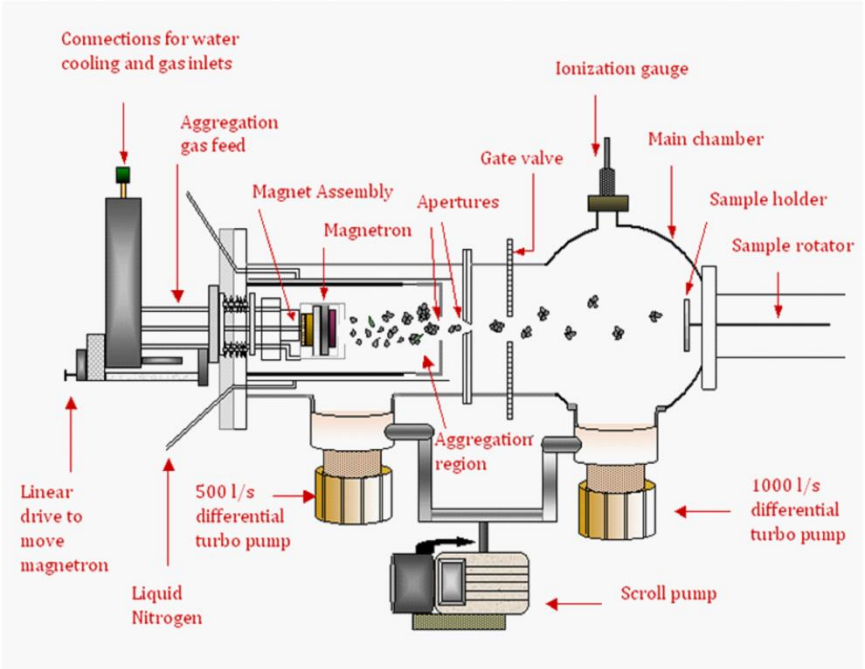


*Figure 2.1: Block diagram of nanocluster deposition system.*

The standard dimensions for the sputter targets are 2" dia (50.8 mm) and 2 mm (5 mm) thickness for magnetic materials (non-magnetic materials) of a planar type. Argon (Ar) gas is used as working gas to sputter the desired targets. Dense plasma is produced inside the magnetron by a continuous electric discharge in the Ar gas. Ar gas is also introduced over the target through the holes present in the magnetron cover. There are two gas inlets to the aggregation zone, one for the Helium (He) gas and another for the Ar gas. The Magnetron is situated on a linear motion drive which enables us to vary aggregation zone space by moving the magnetron back and forth.

The nanocluster source NC200U is shown in figure 2.2 in enlarged view. NC200U consists of magnetron which is mounted on linear drive, aggregation region, a T-piece which is a differential pumping port, pressure gauge flange and apertures opening of clusters to the deposition chamber.

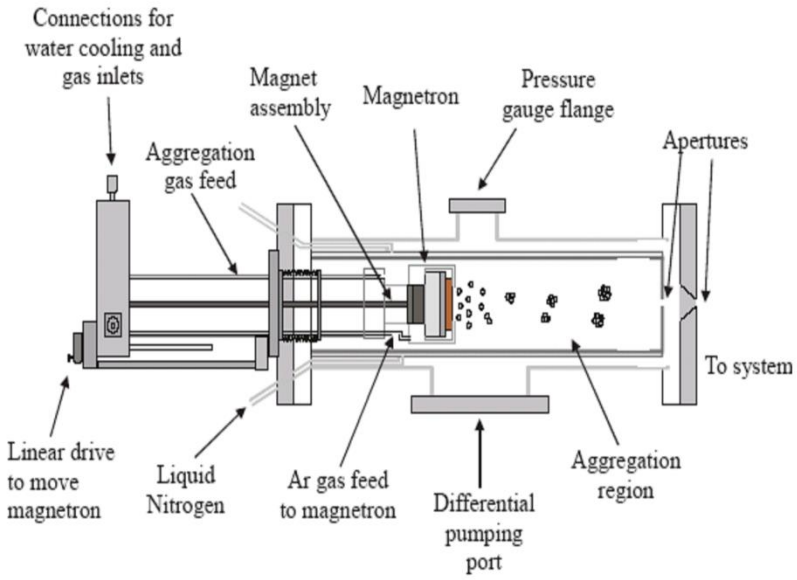


*Figure 2.2: Schematic diagram of enlarged view of nanocluster source NC200U.*

The change of resident time of nanoclusters leads to the changes in the cluster size. Ar and He are connected to magnetron through mass flow controllers (MKS instruments). When a sufficiently large voltage is applied between cathode and anode of magnetron, a glow discharge is formed, causing acceleration of ions towards target holder which is electrically isolated from the target and acts as anode. A system of small ring magnets is arranged behind the sputter target in such a way that the magnetic lines of force (perpendicular to the electric filed) act on electrons on a circular race-track over the sputter target. As a result of this, comparatively higher sputter

erosion takes place over an angular ring while in other parts the erosions are smaller. Figure 2.3 shows the Ag target with impression of heavy sputtering along the race track.

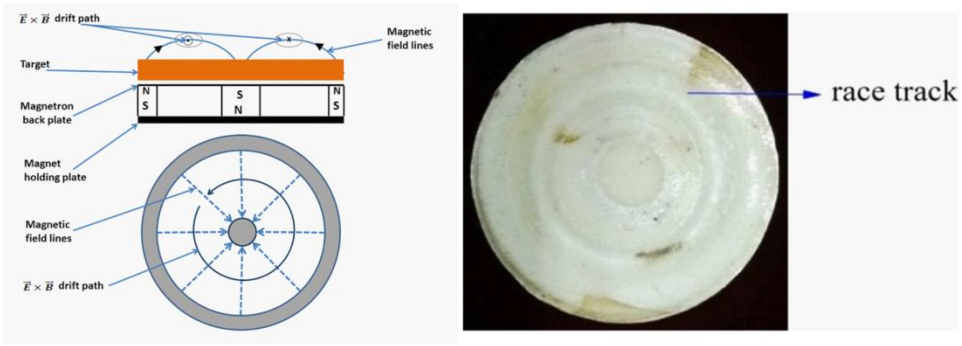


*Figure 2.3: Schematic representation of sputtering principle in planar magnetron target [3] and Silver sputter target with strong impression of erosion.*

The normal separation between the target cap and magnetron cover is 0.3 mm and it is reduced to 0.2 mm for the magnetic target materials. A 500 l/s pumping rate turbo pump is attached to the T-piece to reduce the gas load in the aggregation chamber. The percentage of ionized clusters produced by NC200U is very high (> 30% for Cu). The ionized clusters can be manipulated electrostatically. Ionized cluster beam can be accelerated towards the substrate by biasing them to form highly adherent and uniform coatings [1]. The cluster source is capable of producing clusters consisting of a few tens of atoms up to cluster diameter of more than 10 nm. The compound clusters can also be made by alloy targets or adding appropriate gases into the aggregation tube during the operation. The cluster size depends on the parameters of aggregation length, magnetron power and aggregation gas flow rate.

### 2.2.1 Descriptions of deposition chamber and differential pumping:

Deposition chamber is connected to a 1000 l/s turbo molecular pump to evacuate the gas whereas a 500 l/s turbo pumps the T-piece of nanocluster source. These two turbo pumps are backed by a scroll pump. The deposition chamber is maintained at lower pressure by the higher pumping speed of the deposition chamber pump as compared to the pump of the aggregation chamber. The nanocluster deposition system is able to produce a base pressure of $10^{-8}$ mbar. The apertures in the aggregation region control the gas flow between the aggregation and deposition region. The aperture sizes are in the range of 3-6 mm. Aggregation chamber and deposition chamber are separated by gate valve and this can be operated by hand. The deposition chamber is having EPICentre sample holder, DC ion source, heater, ionization gauge and multiple ports for analysis tools. The EPICentre controller is capable of sample heating, biasing and rotating the sample. Samples can be heated up to 800 $^{o}$C. If the clusters are ionized, the applied bias voltage on the substrates can direct the paths. This can be used to direct the clusters on to the substrate in a uniform fashion. The ionized clusters fly from the target in straight-line paths when the target is biased, resulting in energetic cluster impact on substrate.

### 2.2.2 Operation of nanocluster deposition system:

The turbo molecular pumps are connected to aggregation region as well as deposition chamber and are capable of producing the vacuum of $10^{-8}$ mbar. After getting desired vacuum, Ar gas is introduced and target material is sputtered by DC magnetron with Ar plasma. Ar or He gas is introduced into the aggregation region, then the pressure in the aggregation

region goes from $10^{-3}$ mbar to $10^{-1}$ mbar whereas it goes from $10^{-7}$ mbar to $10^{-5}$ mbar in the deposition chamber. This is maintained by differential pumping. The DC magnetron sputters the target material into the high pressure aggregation region in which sputtered atoms collides with large population of inert gas atoms of Ar or He (or both) that acts as moderators and move diffusively in the direction of flow gas and condense by transferring kinetic energy to the inert gas atoms. During the condensation they start aggregating and forms nanosized clusters. The clusters are channeled through the apertures into the deposition chamber due to low pressure maintained there by differential pumping. Cooled water is circulated around the aggregation region in the nanocluster source which stabilizes the deposition as well as reduces the mean cluster size. The temperature of chilled water is maintained at 18 °C and the flow rate minimum of 3 l/min at a pressure of 2-3 bars. The nanocluster source can be baked up to 150 °C temperature and bake out should extended to 4-5 hours for optimum results. Various parameters of NC200U nanocluster source influence the cluster size viz. aggregation region length, aggregation chamber temperature, inlet gases flow rates (Ar and He), magnetron power, aperture size. The relationship between aggregation length and cluster size is quite complex. However, increasing the aggregation region length increases the cluster size by increasing the resident time of clusters in the aggregation region. The cluster source specifications are given in the table 2.1.

*Table 2.1: Cluster source specifications.*

| Material source | 1kW DC magnetron power supply |
|---|---|
| Target Diameter | 2" or 50.8 mm |
| Target thickness | 2-5 mm |
| Ar flow rate | 10-100 sccm |
| Beam diameter | 5-40 mm (at a source-sample distance of 100 mm) |
| Aggregation length | 65-205 mm |
| Maximum bake out temperature | 150 $^0$C |

## 2.3 Field emission scanning electron microscopy:

Field emission scanning electron microscopy (FESEM) is a surface characterization technique in which an electron gun is raster scanning the specimen of the sample surface to probe its topography and composition or conductivity. When a beam of electron interacts with a specimen (figure 2.4),

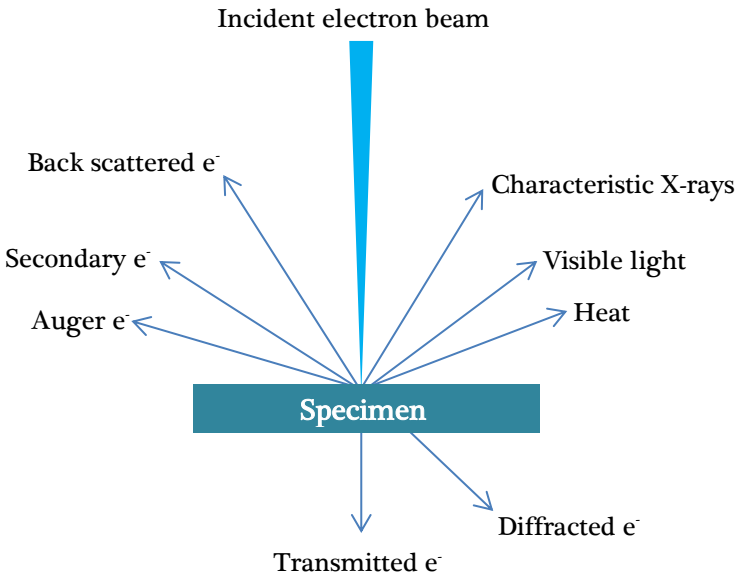


*Figure 2.4: Interaction of a beam of electrons with matter.*

the electrons interact with the atoms of the sample, which results in the emission of back scattered electrons, secondary electrons, Auger electrons,

diffracted and transmitted electrons etc. The secondary electrons signals are detected mostly to get the image. The back scattered electrons are used to invoke distribution of different elements in the sample [4]. The characteristic X-rays reveal the information about the composition and also measure the abundance of elements in the sample. It is difficult to construct the equipment that would have all the possible signals. So SEM is commonly equipped with secondary and back scattered electron detectors.

The FESEM was introduced to improve the resolution of the image with tungsten source. It consists of an electron source, electromagnetic lenses and in-lens detector. In order to reduce the work function and to enhance the emission, tungsten is covered by a layer of zirconium oxide ($ZrO_2$). The beam scans in a raster scan pattern. Secondary detector and back scatter detector detect secondary and back-scattered electrons emitted from the sample and convert to a voltage signal. When the amplified voltage is applied to the cathode ray tube it appears as variations in the brightness which results in an image which is a distribution map of the intensity of the signal that is being emitted from the scanned area of the sample.

FESEM also has energy-dispersive X-ray (EDX) spectrometer, which detects the characteristic X-rays originating from the sample irradiation with electron beam. This method is to detect elementary composition analysis of the sample. In our studies we have used FESEM of Carl Zeiss Ultra 55 system model to observe geometry, size and separation of nanoclusters deposited on the substrates viz. glass, silicon and alumina. Pictorial image and schematic representation of FESEM are depicted in figures 2.5 and 2.6, respectively.

*Figure 2.5: Image of field emission scanning electron microscope.*

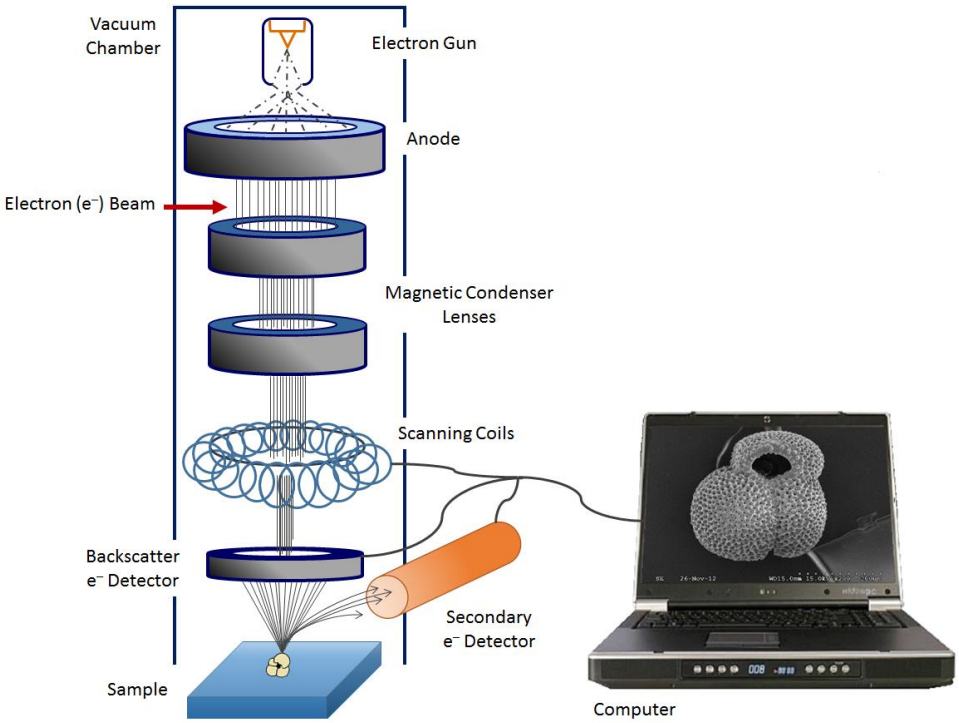


*Figure 2.6: Schematic representation of field emission scanning electron microscope.*

## 2.4 Atomic force microscopy:

Atomic force microscopy (AFM) is a high-resolution microscopy technique which produces precise topographic images of a sample by scanning the surface with a nanometer-scale probe. A unique advantage of AFM is that it enables imaging with minimal sample preparation, in air or liquid environment. AFM operates by measuring repulsive (contact mode) or attractive forces (noncontact mode) between a tip and the sample. The tips are made up of silicon (Si).

In contact mode AFM the tip makes a soft physical contact with the sample surface. The tip is attached to the end of a cantilever with a low spring constant, lower than the spring constant holding the atoms together in a sample. As the scanner gently traces the sample under the tip, the contact force causes the cantilever to bend to accommodate changes in topography. The resolution of AFM depends mainly on the sharpness of the tip.

In the non-contact mode the cantilever is held less than a few angstroms from the sample surface. The attractive probe-sample interaction changes the spring constant of the cantilever and this modifies its resonant frequency. A modification of the resonant frequency will result in a change of the probe's oscillation amplitude which is fed to a feedback loop which in turn controls the movement of the tube scanner.

Different modes of operation are chosen based on the surface characteristics of interest and on the hardness or stickiness of the sample. Contact mode is most useful for hard surfaces whereas non-contact

mode is for soft surfaces. The nanocluster films in the present work were scanned in the contact mode using the model SPA 400 of Seiko Instruments.

## 2.5 Ultraviolet-Visible spectrophotometer:

Ultraviolet (UV)-Visible (Vis) spectroscopy is the simplest optical technique to measure the optical properties of materials. The image of the spectrophotometer is shown in figure 2.7.

*Figure 2.7: Pictorial image of UV-Vis Spectrophotometer(Jasco V-670).*

It uses two light sources, one deuterium lamp which can produce light in the range 187 nm-350 nm and the other one is halogen lamp for visible and NIR region (range of 330 nm-2700 nm). It utilizes a unique, single monochromator design covering the entire region from 190 nm to 2700 nm. The monochromator has two gratings, one is 1200 groves/mm for UV/Vis range and the other one is 300 grooves/mm for NIR range. It also has two detectors to detect the data in the different regions. A photomultiplier tube (PMT) detector is used to detect in the UV/Vis region and Petlier-cooled lead sulphide (PbS) in the NIR region. Both detectors and gratings are automatically exchanged within the user selectable range from 750 nm to 900 nm. An optical spectrometer has three different accessories

for measurements (i) variable angle transmission, (ii) fixed angle and (iii) variable angle reflectance. The beam path schematic is shown in figure 2.8.

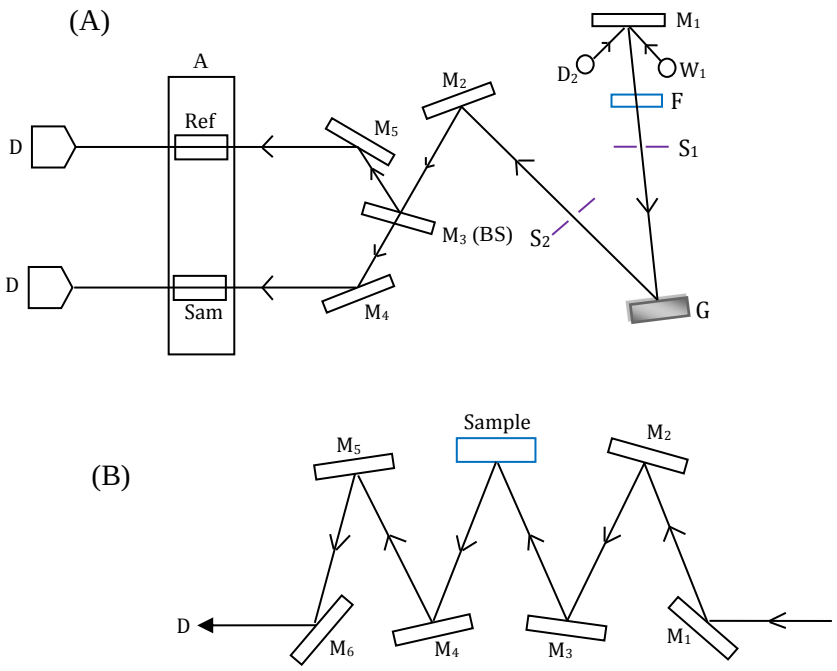


*Figure 2.8: Schematic representation of UV-Vis Spectrophotometer (A) absorption (B) fixed angle (5°) reflection geometry: $M_1$-$M_6$ are mirrors, F is filter, $S_1$ and $S_2$ are slits, G is grating, D is detector, BS is beam splitter,$W_1$ is halogen lamp, $D_2$ is deuterium lamp, A is accessary, Ref is reference, Sam is sample.*

The lamp light reflected from mirror $M_1$ goes through the slit $S_1$ and is projected on the grating G. The grating can be rotated to allow the particular wavelength to be selected. The filter F is used to eliminate the higher order unwanted diffraction beam. At any angular variations of grating only single wavelength (monochromatic light) can be successfully passed through slit $S_2$. After second reflection from the mirror $M_2$ the light is passed on to the beam splitter (BS) where half of the monochromatic light is

transmitted on to the mirror $M_4$ and the other half gets reflected and pass on to the mirror $M_5$. One of the reflected beams passes through the reference sample (it can be air or some other medium) and transmitted light passes through the sample. The intensities of the beam collected at the end using detector are shown in the figure 2.8. The photometer computes the intensities ratio of sample signal to reference signal ($I/I_0$) to obtain the transmittance or absorbance. The absorption and reflection spectra were carried out by commercial UV-Vis spectrophotometer manufactured from JASCO V-670.

## 2.6 Micro-Raman spectrometer:

The basic principle of Raman effect is inelastic scattering of light. When light is illuminated on the sample a fraction of the light is scattered differently compared to incident light. This differential scattering is known as inelastic scattering. Very intense excitation line is required to get Raman signals because Raman scattering cross-section is very low. One in $10^{-6}$ molecules of incident light will emerge inelastically. Monochromatic and collimated laser light is used in Raman measurements.


*Figure 2.9: (A) Image of micro-Raman spectrometer (Horiba LabRam HR 800).*

Raman measurements were performed using Horiba Lab Ram HR 800 micro-Raman spectrometer manufactured from Jobin Yvon. The spectrometer contains three laser excitation wavelengths viz. 514.5 nm ($Ar^+$ laser), 632.8 nm (He-Ne laser) and 785 nm (Diode laser). The image and black diagram of Raman spectrometer is shown in figure 2.9.

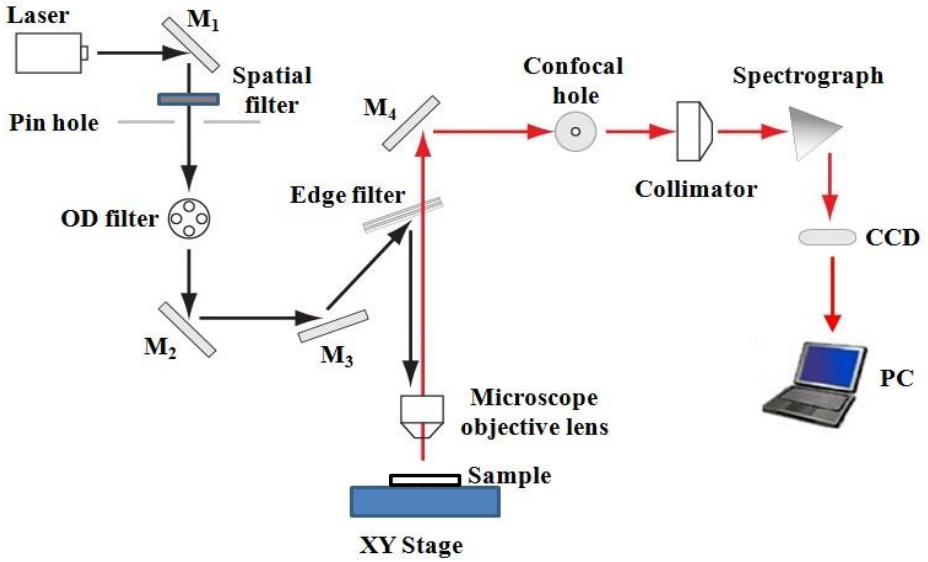


*Figure 2.9: (B) Schematic representation of micro-Raman spectrometer.*

Laser light comes through several optical components such as spatial filter, optical density filter and edge filter. In the present technique scattered light is collected in back scattering geometry (or 180° geometry). Collimated laser light is focused on the sample surface through objective lens and sample was mounted on the X-Y motorized stage. This stage can move in X-Y direction to get Raman signal at each and every site of the sample. Same objective lenses were used to collect the scattered data. Here we have different optical objectives viz. 10X, 50X and 100X with numerical aperture 0.25, 0.75 and 0.90 respectively. The numerical aperture has influence on the Raman signal. The signal is proportional to square of the numerical

aperture. A controllable slit and confocal hole are used before the scattered light reaches the spectrograph. Spectrograph uses two gratings 600 l/mm and 1800 l/mm. Spectrograph focuses the laser light on the charge coupled device (CCD) camera. All these optical components are controlled with user graphical interface on a computer attached to the system.

## 2.7 High temperature tubular furnace:

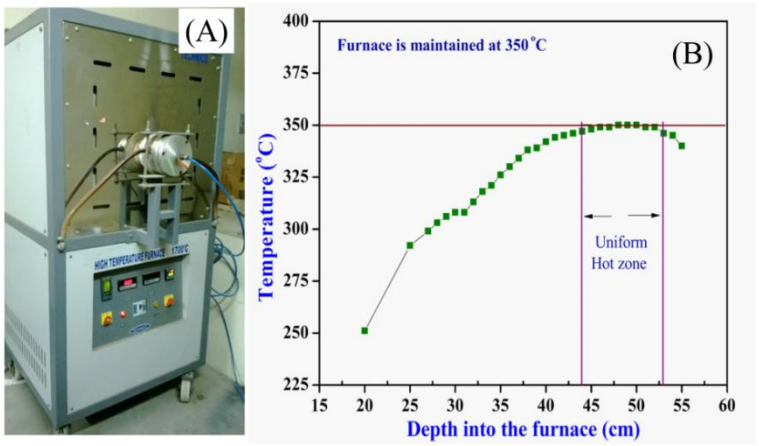


*Figure 2.10: (A) pictorial image of high temperature tubular furnace (B) profile of the tubular furnace hot zone.*

Ag nanocluster films were heat treated in a high temperature tubular furnace (TECHNICO make). Image of tubular furnace is shown in figure 2.10(A). This furnace contains temperature controller of EUROTHERM and safety controller. It also associates with gas flow controllers which control the inlet gas flow rate. The furnace is equipped with chiller to circulate chilled water. In order to avoid heating up at uneven temperatures, samples have to be kept inside the uniform hot zone of the sample holder.

To find the uniform hot zone we kept the furnace at 350 °C for 4 hours and measured the temperature in the furnace with external thermocouple with respect to the depth into the furnace. The uniform "hot zone" profile is shown in figure 2.10(B). The hot zone is situated between 44 to 53 cm.

## 2.8 Glove box:

As soon as substrates are brought out to ambient atmosphere the nanocluster substrates will be oxidized. To remove the oxidation of the substrates we again heat treated the substrates in a glove box (MBRAUN, Germany) at 200 °C for 30 minutes. The image of glove box is shown in figure 2.11(A).


*Figure 2.11: (A) Pictorial image of Glove box (MBraun, 20G).*

Glove box is a hermetically sealed enclosure. It provides a working space inside the box that is segregated from the outside. Inside the box an artificial atmosphere which typically contains moisture ($H_2O$) and oxygen ($O_2$) in the range of < 1ppm levels is maintained. This protects the product from unwanted reaction with $O_2$ or $H_2O$ vapor. The glove box is maintained

under ultra-high pure (UHP) inert gas (Ar) atmosphere. The glove box has two boxes, one is meant for oven and the other one for spin coater. Each box is having one mini load-lock chamber to carry the samples inside the box through it. One main chamber is connected to both the boxes. These boxes are operated using SIEMENS simatic touch panel. All these are connected to main controller which is situated in between two boxes. This is connected to a recirculation chiller to reduce the temperature of the gas molecules. The whole system is connected to a vacuum pump. The block diagram of glove box is shown in figure 2.11(B).

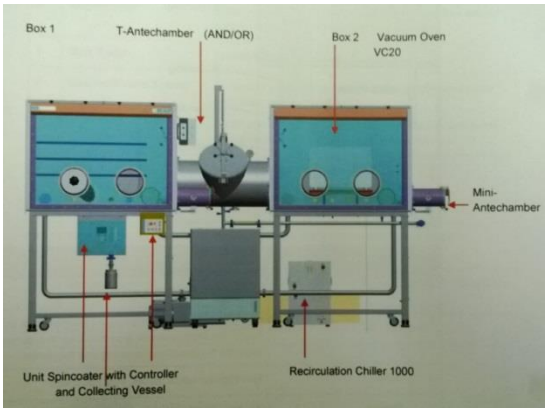


*Figure 2.11: (B) Block diagram of glove box.*

The glove box contains several ports: gloves, antechambers, vacuum pump, gas purification system, foot switch for increasing or decreasing the box pressure, flow meter, dust filter, electropneumatical valves, box filter and blower.

**References:**

[1] H. Haberland, M. Karrais, M. Mall and Y. Thurner, "Thin films from energetic cluster impact: A feasibility study" *J. Vac. Sci. Technol. A 10 (1992) 3266.*

[2] H. Haberland, Clusters of atoms and molecules I: Theory, Experiment and Clusters Atoms, *Springer Series in Chemical Physics Vol. 52 (Springer-Verlag, New York, 1994).*

[3] S. Mondal and S.R. Battacharyya, "Performance of a size-selected nanocluster deposition facility and in situ characterization of grown films by x-ray photoelectron spectroscopy" *Rev. Sci. Instrum. 85 (2014) 065109.*

[4] G. Lawes, Scanning Electron Microscopy and X-ray Microanalysis, John Wiley & Sons, Inc, New York, 1987.

# Chapter 3

## Optimization of SERS substrates and studies on organic dyes: Rhodamine 6G and Crystal Violet

*In this chapter we will discuss the methods used for optimization of the SERS substrates for the measurements presented in subsequent chapters of this thesis. The SERS activities of these substrates were analyzed using two organic dyes viz. Rhodamine 6G (R6G) and Crystal Violet (CV). The SERS enhancement factors were calculated and observed to be 12 orders of magnitude. The SERS spectra were highly reproducible. The lowest detection limits of R6G and CV were $10^{-16}$ M and $10^{-18}$ M, respectively using our SERS substrates. These results were published in Chemical Physics Letters[1] and Materials Chemistry and Physics[2].*

[1]*G. Upender, R. Satyavathi, B. Raju, K Shadak Alee, D. Narayana Rao and C. Bansal, Chem. Phys. Lett., 511 (2011) 309.*

[2]*Raju Botta, G. Upender, R. Sathyavathi, D. Narayana Rao and C. Bansal, Mater. Chem. Phys., 137 (2013) 699.*

## 3.1 Introduction:

One of the major challenges in the field of SERS is the difficulty in producing efficient SERS substrates with large enhancement factors and with reproducibility as well as uniformity over the whole substrate [1, 2]. It is also desirable that the substrates are easy to fabricate and store. The most commonly used SERS-active substrates are made from aggregated Ag and Au colloids [3-5]. These metal colloid solutions of Ag or Au nanoparticles have shown high enhancement factors. The SERS spectrum of a single R6G molecule has also been reported [6]. However, the stability of the colloidal solution and reproducibility of aggregation are two major problems for nano-Ag/Au substrates [7].

To meet the above challenges the present work was carried out to fabricate SERS substrates using magnetron cluster deposition method and to show that these substrates play an important role in reproducible and highly efficient SERS measurements. As mentioned earlier it is well established that the SERS intensity depends on the excitation of localized surface plasmons (LSP), which in turn depends on particle size and density. These parameters were optimized for Ag nanoclusters using a cluster deposition system and suitable heat treatments. We will show here that this technique is better than the chemical techniques reported so far since there is no contamination of the metal nanoclusters by residual chemicals.

## 3.2 Optimization of Ag nanocluster substrate:

In our cluster deposition system the areal density of clusters (number of clusters per unit area of the substrate) depends on the deposition time (the details of the cluster deposition system were presented in chapter

2). We therefore deposited Ag nanoclusters for different deposition times of 7, 8, 9 and 10 minutes. Figure 3.1 shows the FESEM image of the as-deposited nanocluster film for a deposition time of 8 minutes. This figure evidences the nanoclusters are distributed randomly with a size in the range 10 nm - 20 nm but the surface morphology of the clusters is not well defined.

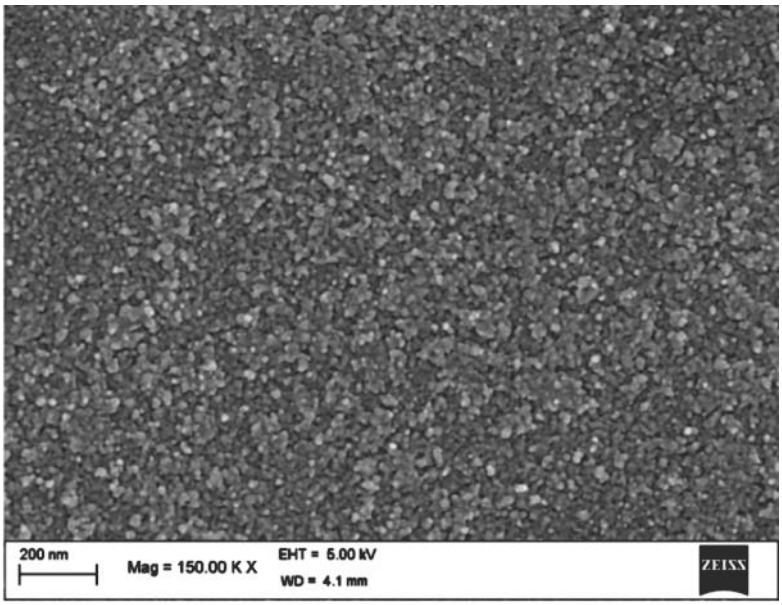


*Figure 3.1: FESEM image of as-deposited Ag nanoclusters on glass substrate.*

The optical absorption of the as-deposited films showed a broad absorption but did not show any well-defined plasmon absorption peaks. We therefore carried heat treatments at different temperatures to see if it improves the substrates. The annealing temperatures used were 100 $^{o}$C, 200 $^{o}$C, 300 $^{o}$C and 400 $^{o}$C and the heat treatments were carried out for 2 hours at these temperatures in an argon atmosphere. The corresponding FESEM images of annealed nanocluster films are shown in figure 3.2. The deposition time for these films was 8 minutes.

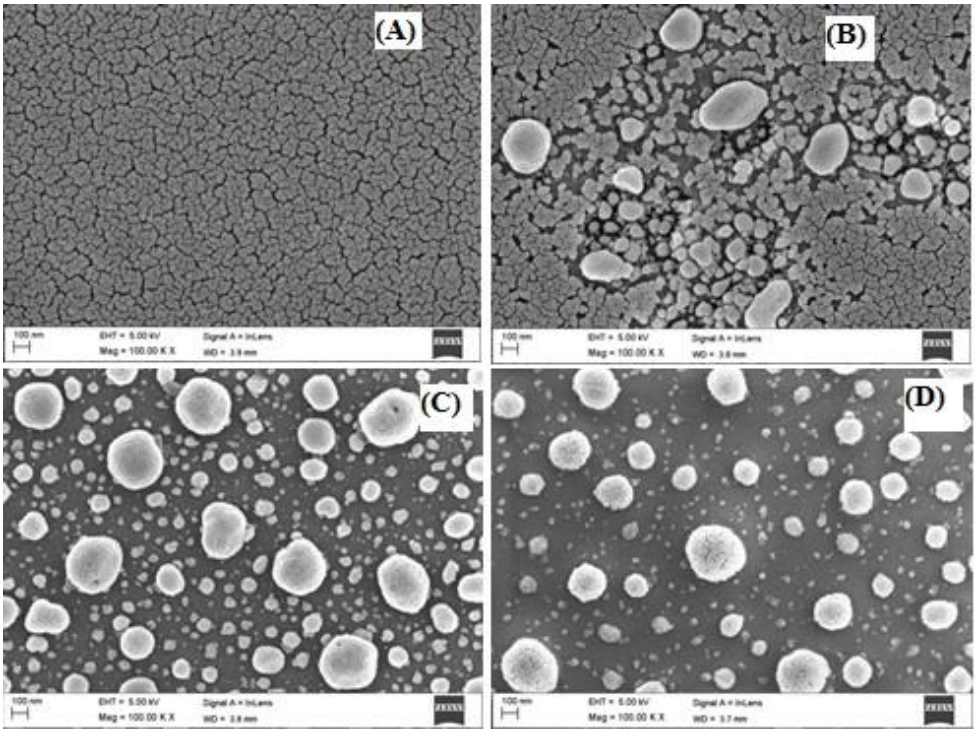


*Figure 3.2: FESEM images of Ag nanocluster substrates (8 minutes deposited films) heat treated at (A) 100 °C (B) 200 °C (C) 300 °C and (D) 400 °C for 2 hours in an argon atmosphere.*

From the FESEM images one can see that at 100 °C Ag nanoclusters are not separated out but at 200 °C they have just started forming separated island-like structures. At 300 °C the islands are well separated and there are two distinct sizes of the particles. At 400 °C inter cluster separation is more as compared to 300 °C and the size of the clusters is bigger. To find the optimum annealing temperature we did SERS measurements on these films with Crystal Violet (CV) as a probe molecule.

Aqueous solution of $10^{-4}$ M of CV were prepared by sequential dilution method. 20 μL droplet of the solution was dropped on these substrates and allowed to dry in ambient atmosphere. SERS measurements

were carried out with laser excitation wavelength of 514.5 nm. One of the SERS spectrum of $10^{-4}$ M of CV adsorbed on these substrates is displayed in figure 3.3. The peaks present in the spectrum are in good agreement with the previous reports [8, 9].

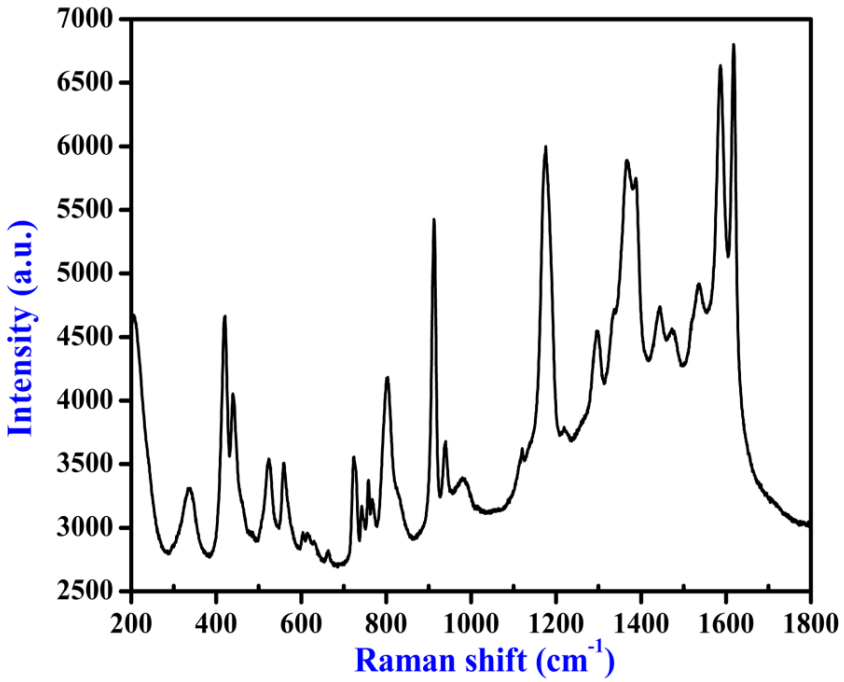


*Figure 3.3: SERS spectrum of $10^{-4}$M CV adsorbed on the Ag nanocluster substrate.*

The Raman lines at 1618 $cm^{-1}$, 1586 $cm^{-1}$, 1534 $cm^{-1}$, 1445 $cm^{-1}$ and 1370 $cm^{-1}$ are due to aromatic C-C stretching. The Raman lines at 1177 $cm^{-1}$ is due to C-H in-plane bending vibration, and lines at 913 $cm^{-1}$ and 803 $cm^{-1}$ are assigned to C-H out of plane bend. The 421 $cm^{-1}$ line is due to C-C-C out of plane bend and 338 $cm^{-1}$ is central-C-phenyl in-plane bending vibrations.

*Table 3.1: SERS intensity variation of the 1177* $cm^{-1}$ line *with annealing temperature of Ag nanocluster substrates.*

| Temperature (°C) | Intensity (a. u.) |
|---|---|
| 100 | 51256±456 |
| 200 | 60431±921 |
| 300 | 94849±1589 |
| 400 | 35597±456 |

The characteristic Raman line of CV at 1177 $cm^{-1}$ was chosen to compare the intensity values for the different substrates. The observed Raman line intensities are given in table 3.1.

From this study it is observed that the annealing temperature of 300 °C gave good results as compared to other annealing temperatures. In the earlier studies it has been observed that for metal cluster films annealed at 1/3 melting point of the metal [10], the surface oxidation layer, if any, is removed and it also assists in atom diffusion. Our experimental observation of 300 °C as an optimum annealing temperature is in conformity with 1/3 melting point of Ag (961.8 °C). Further, SERS measurements were carried out with this optimized annealing temperature to verify the sensitivity and uniformity of the SERS-active substrate.

The effect of the 300 °C, 2 hour heat treatments for films deposited for different periods of time is shown in the FESEM images given in figure 3.4. From these micrographs we observe that nanoclusters on 7 minute deposited substrates were closely packed whereas there were isolated nanoclusters on other substrates.

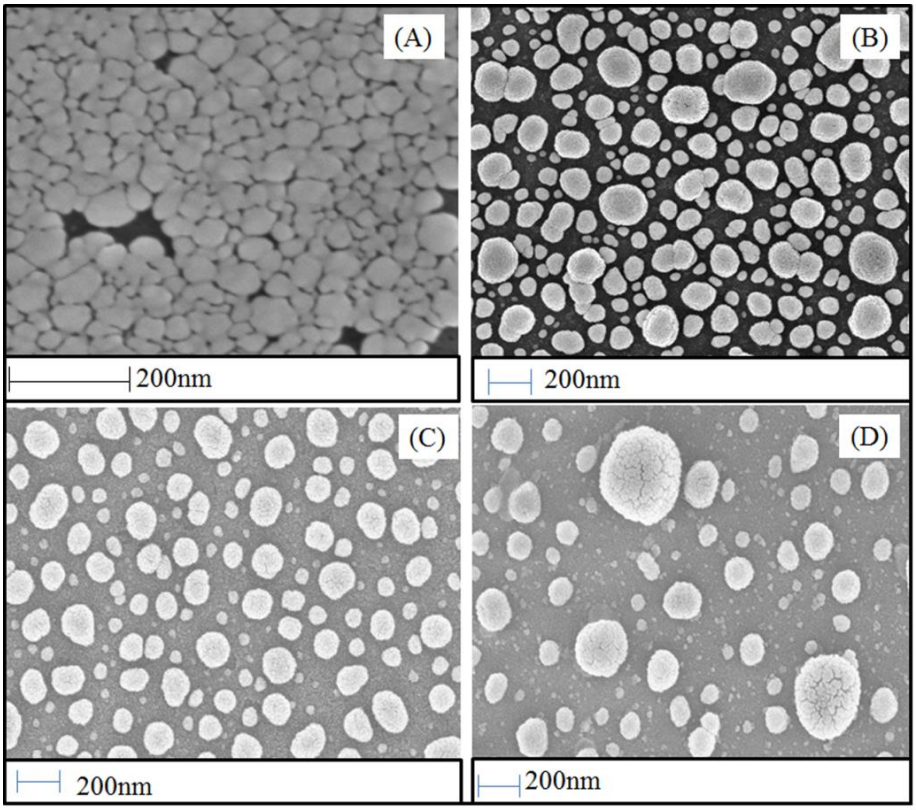


*Figure 3.4: FESEM image of annealed Ag nanocluster films at 300 °C for 2 hrs. for different cluster deposition times (A)7 (B) 8 (C) 9 and (D) 10 minutes.*

Figure 3.5 shows the absorption spectra of annealed Ag nanocluster substrates. It is observed that surface plasmon peaks are in the range 365 nm - 470 nm. There are two absorption peaks in each curve. It is also observed that the absorption peaks of the nanoclusters are broad in nature which is due to a large distributions of particle sizes and shapes. The absorption spectra also support the fact that there are two different size distributions present in the substrates as seen in the FESEM micrographs. The peaks in the region from 434 nm to 470 nm are due to dipolar oscillations whereas the peaks in the lower wavelength region of 365 nm to 385 nm are due to quadrupolar oscillations [11]. Dipolar oscillations are due

to small metal nanoclusters (< 100 nm) and quadrupolar oscillations are due to larger size nanoclusters (>100 nm) [11]. The dipolar oscillations are situated in longer wavelengths with respect to quadrupole or multi polar concentration.

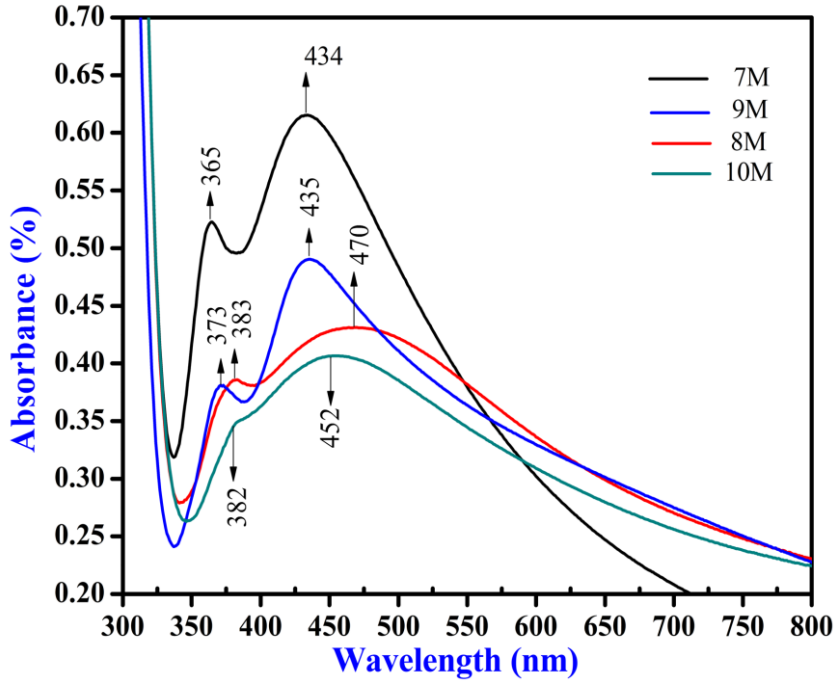


*Figure 3.5: UV-Vis absorption spectrum of Ag nanoclusters of different deposition time substrates.*

The cross-sectional area distribution of the nanoclusters was measured using ImageJ software and is shown in figure 3.6. The distributions could be fitted to two lognormal peaks. The average diameters of the clusters deduced from the areas of the peaks were 60 nm and 150 nm with standard deviations of the areal log-normal distributions being 0.69 and 0.29 respectively.

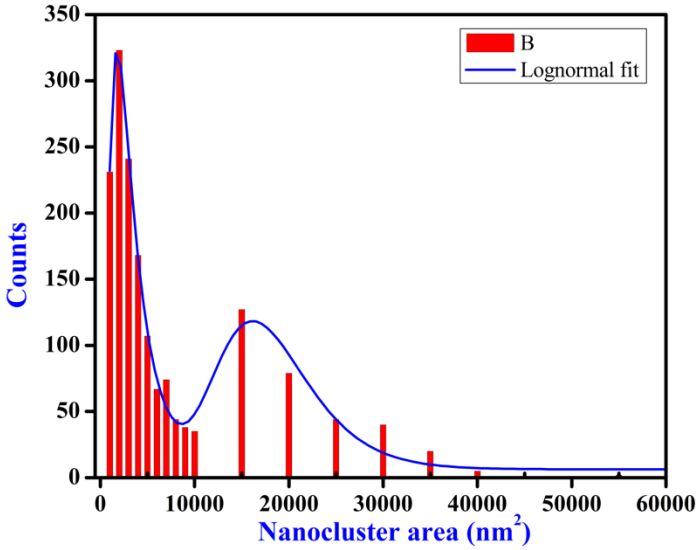


*Figure 3.6: Cross-sectional area distribution of nanoclusters for an 8 minute deposited film that was heat treated at 300 $^{o}$C for 2 hours (the optimum heat treatment that gave the best SERS intensities).*

Rhodamine 6G (R6G) molecule was taken as another probe molecule for SERS studies. Different molar concentrations ($10^{-3}$ M-$10^{-18}$ M) of aqueous solutions of R6G were prepared by sequential dilution method. The laser excitation (514.5 nm) wavelength is such that it falls within the surface plasmon resonance (SPR) absorption band of the nanoclusters and is also in resonance with the R6G electronic absorption which occurs at 520 nm. This would give rise to a Resonant Raman Scattering (RRS) as discussed in Chapter 1. We also used other laser excitation wavelengths 632.8 nm and 785 nm but these are away from the electronic absorption band of R6G resulting in non-resonant Raman scattering. Experimentally we observed that the Raman intensities at 632.8 nm were much weaker as compared to 514.5 nm whereas at 785 nm there were no observable Raman intensities. Subsequent Raman studies were carried out using the 514.5 nm laser wavelength.

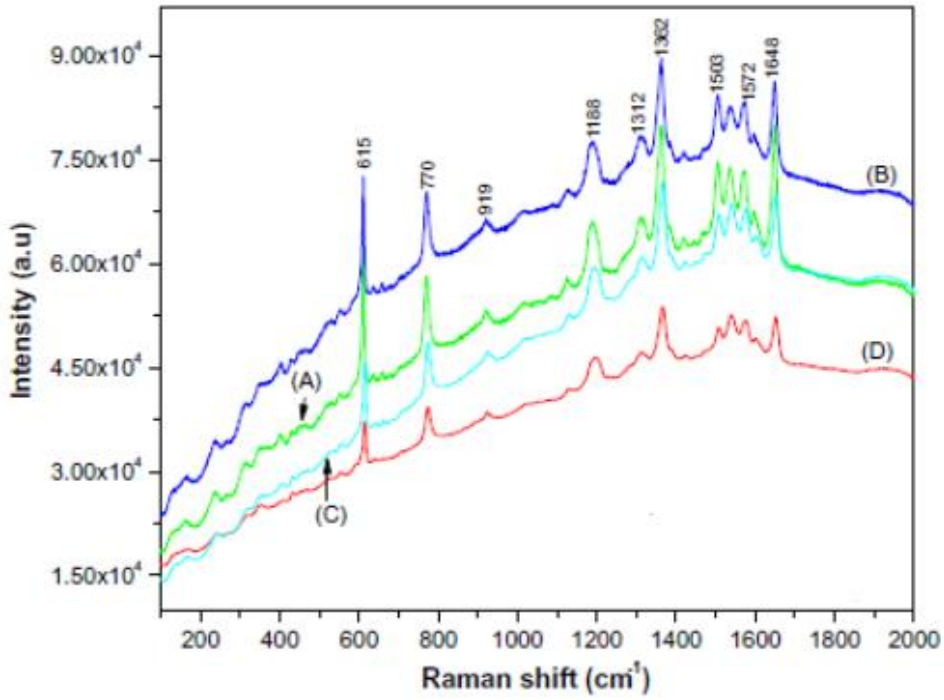


*Figure 3.7: SERS spectra of $10^{-4}$ M R6G molecule on (A) 7 (B) 8 (C) 9 and (D) 10 minutes deposited substrates.*

Figure 3.7 shows the SERS spectra for R6G recorded for substrates deposited at different times but with the optimum heat treatment of 300 °C for two hours. The peaks at 615 $cm^{-1}$, 770 $cm^{-1}$, and 1188 $cm^{-1}$ are associated with C-C-C ring in-plane, C-H out of plane bend mode and C-C stretching vibrations, respectively. The peaks at 1312 $cm^{-1}$, 1362 $cm^{-1}$, 1503 $cm^{-1}$, 1572 $cm^{-1}$ and 1648 $cm^{-1}$ arise from symmetric modes of in-plane C-C stretching vibrations of R6G. The peaks are characteristic Raman lines of R6G [6, 12-16].

The Raman line at 1648 $cm^{-1}$ was taken as a reference line to find the intensity of this line on different substrates. The intensities were calculated

by carrying out a Lorentzian fit to the lines and the corresponding data are given in table 3.2.

*Table 3.2: Intensity variation of Raman line at 1648 $cm^{-1}$ on different substrates.*

| Deposition time (minute) | Intensity (a. u.) |
|---|---|
| 7 | 82500±1253 |
| 8 | 86250±1453 |
| 9 | 67500±856 |
| 10 | 50725±752 |

From the above data we can say that 8 minute deposition substrates are giving good signals as compared to other substrates.

In the SERS spectra, the band at around 230 $cm^{-1}$ provides additional information about the nature of the interaction between R6G and the Ag surface. This band is assigned to Ag-N stretching vibration of the Ag-R6G via the ethyl amino group [13]. This confirms the adsorption of R6G on the metal surface via an Ag-N bond. Because of this strong bond, SERS spectral signatures were found even after a chemical cleaning procedure several times or ultrasonic cleaning. Therefore we believe that the chemical effect plays an important role for SERS in the present study at low concentration [17]. It shows the sensitivity of the technique to detect and identify even a small concentration of molecules.

### 3.3 Substrates sensitivity:

Figures 3.8 and 3.9 show the SERS spectra of CV and R6G in the range of $10^{-4}$ M to $10^{-18}$ M. The spectra are in good agreement with previous reports [8, 9, 18]. It was observed that the Raman peaks were sharper with

decreasing concentration.

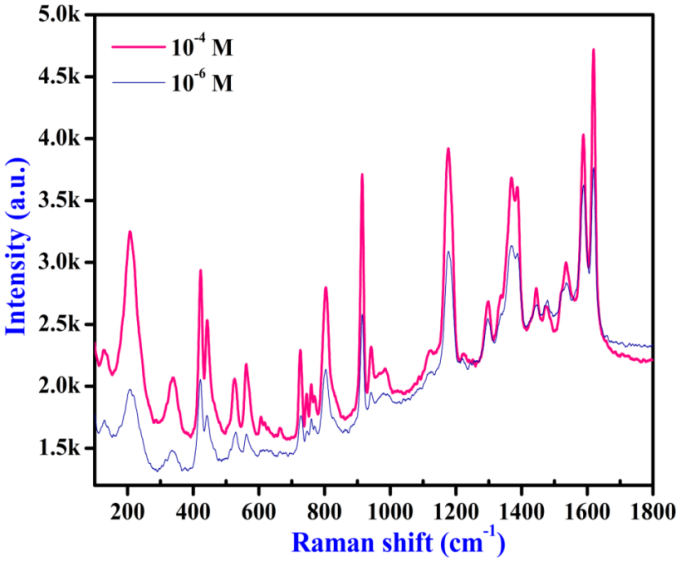


*Figure 3.8A: SERS spectra of $10^{-4}$M and $10^{-6}$M of CV on the Ag nanocluster substrates.*

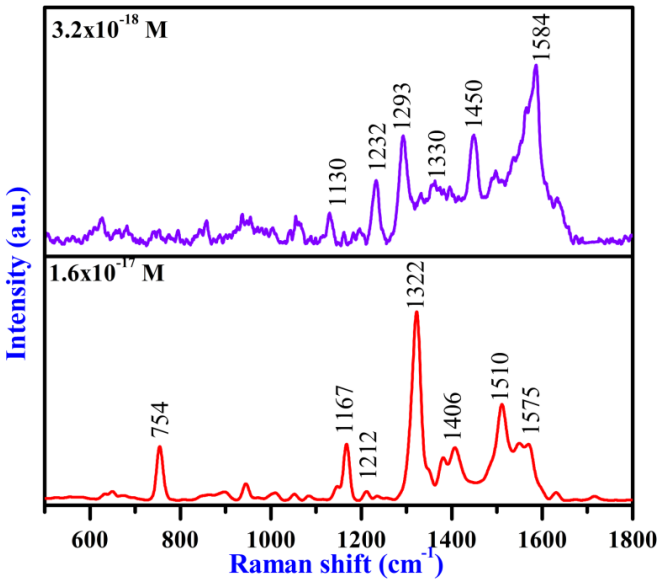


*Figure 3.8B: SERS spectra of 1.6 x $10^{-17}$M and 3.2 x $10^{-18}$M of CV adsorbed on the Ag nanocluster substrates.*

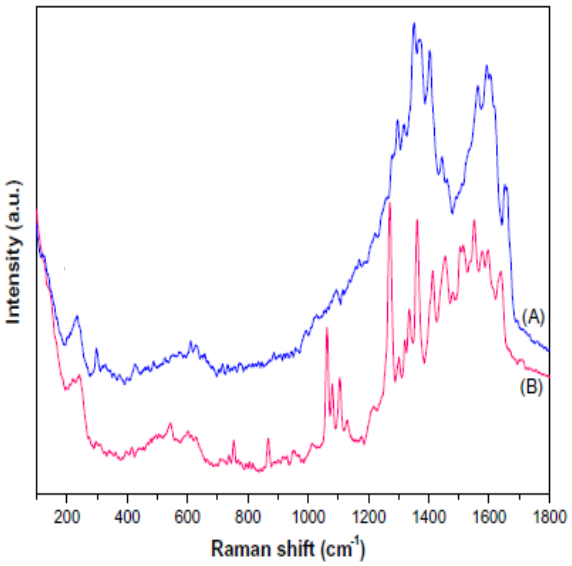


*Figure 3.9: SERS spectra of R6G with concentration of (A) 1x $10^{-14}$ M and (B) 1x$10^{-16}$ M.*

The analytical enhancement factor (AEF) was calculated using the following formula [19].

$$AEF = \frac{I_{SERS} / C_{SERS}}{I_{RS} / C_{RS}} \quad \text{.....1}$$

where $I_{SERS}$ corresponds to the Raman intensity obtained for the SERS substrate under a certain concentration of $C_{SERS}$, and $I_{RS}$ corresponding to the Raman intensity obtained under non-SERS conditions at an analyte concentration of $C_{RS}$. In the present study, $I_{SERS}$ and $I_{RS}$ were determined using the 1584 $cm^{-1}$ as the reference peak. The CV concentrations of 1x$10^{-4}$ M and 3.2 x $10^{-18}$ M were taken as $C_{RS}$ and $C_{SERS}$, respectively. The enhancement

factor (EF) obtained was 6.7 x $10^{12}$. The lowest concentration for which SERS signals could be detected was 3.2 x $10^{-18}$ M. So, the limit of detection (LOD) of CV is 3.2 x $10^{-18}$ M. The enhancement factor obtained for R6G was 2 x $10^{12}$. R6G was detected up to 1x$10^{-16}$ M. So the LOD of R6G is $10^{-16}$ M.

Recently, F.A. Harraz et al. [20] compared the enhancement factors of different substrates with CV molecule. He has also included our result [24, 29] in the table which is reproduced here (table 3.3). The enhancement factors obtained by our SERS substrates are very high as compared to all other reported values. This gives us confidence in our SERS substrate preparation techniques.

*Table 3.3: Comparison of analytical enhancement factors (AEF) and limit of detection (LOD) of various SERS substrates for the detection of CV* as done by *F.A. Harraz et al. [20]*.

| SERS substrate | Reference | LOD | AEF |
|---|---|---|---|
| AgNPs/meso-Psi | [20] | $10^{-10}$M | 1.3x $10^{6}$ |
| Au/macro-Psi | [21] | $10^{-12}$M | $10^{8}$ |
| Ag/buoyant silica | [22] | 7.5 x $10^{-9}$M | 6.9 x$10^{8}$ |
| Colloidal AgNPs | [23] | $10^{-15}$M | 1.3x $10^{8}$ |
| Ag nanoclusters/glass | [24] | 3.2x $10^{-18}$M | 6.7x $10^{12}$ |
| Ag encapsulated Fe@$SiO_2$ | [25] | $10^{-10}$ | n/a |
| Ag colloids | [26] | n/a | 1.8 x $10^{3}$ |
| AgNPs/porous polymer | [27] | $10^{-7}$M | ~ $10^{8}$ |
| Single crystal Ag slices | [28] | $10^{-5}$M | 2.6 x $10^{3}$ |
| Ag nanorods/glass | [29] | $10^{-10}$M | NA |
| 2D nanostructure AuNPs | [30] | n/a | $10^{8}$ |
| Ag nanocluster/glass or Si | [31] | $10^{-8}$M (Ag/glass) | n/a |

### 3.4 Single molecule detection:

SERS has been suggested for single molecule detection (SMD) and it has attracted enormous amount of interest in recent years [32-39]. So there is a need to do further work towards SMD using stable, reproducible and uniform SERS-active substrates. According to many theoretical and experimental results [11, 40] it has been observed that hot-spots are required for SMD. The junction between two nanoparticles acts as a hot-spot for the detection of a single molecule. The reason for this is as follows: as two large nanoparticles approach each other, their transition dipoles, composed of oscillating ballistic carriers in each particle, couple [12].

Classical electromagnetic theory predicts that the enhanced field around each particle coherently interferes [41]. As the distance between the nanoparticles decreases, the coupled Plasmon resonance shifts to the red and the enhanced electromagnetic field increases in the junction between the particles. The junction can therefore act as an electromagnetic hot spot. The field intensity at these hot spots is maximum, which will lead to strong Raman signal of the adsorbed molecules. Our substrates also have uniform hot-spots on it as shown in the FESEM image of a single nanocluster in figure 3.10.

The Ag nanocluster surface is not smooth and there exists an interconnected porous bi-continuous structure of metal and empty spaces. The gap between the surfaces of the metal ligaments is of 2-5 nm. These gaps serve as an ideal hot-spot for electric field enhancement where the molecules can sit.

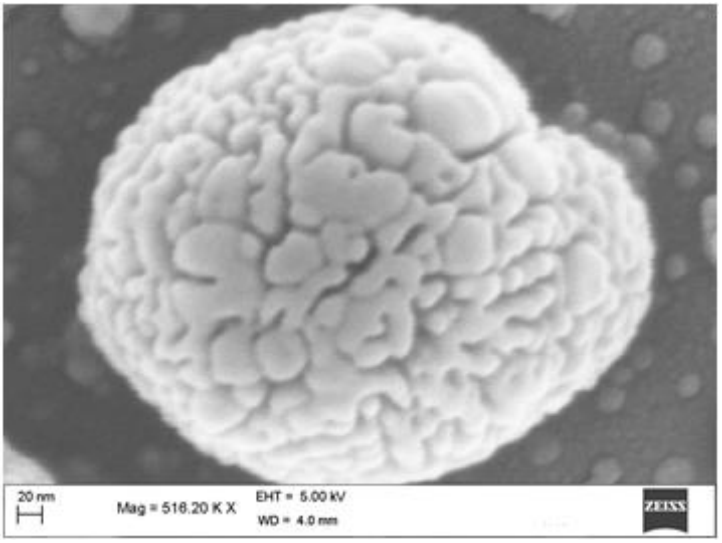


*Figure 3.10: FESEM image of single Ag nanocluster on glass substrate.*

One can notice from figure 3.8 the highly resolved Raman spectral characteristics of CV molecule at $10^{-18}$ M concentration in comparison to the higher concentrations. One also observes from figure 3.8 that the peaks are shifted by a few wavenumbers, and one can also see the appearance of new Raman lines. Many reports [6, 42] suggest that these wavenumber fluctuations also known as blinking effect are characteristic of single molecule SERS. This effect has been called as hallmark of single molecular detection [17]. Y. Sharaabi et al. [43] and H. Liu et al. [37] reported SMD of molecules and they have shown in their reports that the spectrum which is coming from dye concentration of below $10^{-8}$ M is the single molecule spectrum. Thus the observed features of SERS spectra (Figure 3.8) indicate that the present substrate can detect a single molecule of CV. The estimated probability of a molecule being present in the laser beam of spot size 1μM for a 10 μL solution of molar concentration 3.2 x $10^{-18}$ M spread out uniformly over an area of 700 $\mu M^2$ is only 2 percent. The laser beam

therefore had to be moved to several positions before a Raman signal could be detected thereby indirectly confirming that the Raman signal was coming from a single molecule.

### 3.5 Quantitative analysis of molecules using SERS:

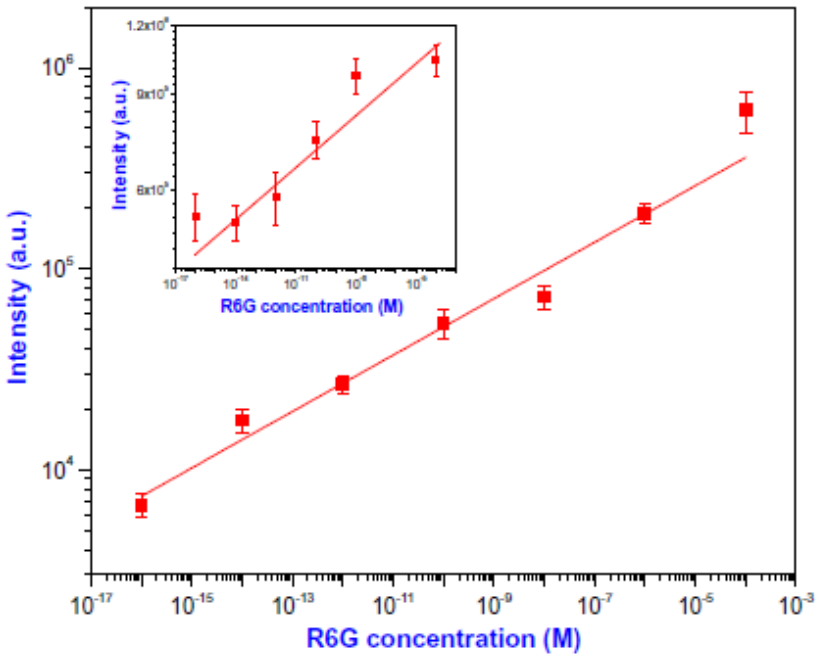


*Figure 3.11: Intensity variation of the Raman peak at 1570 $cm^{-1}$ with R6G molar concentration. Inset shows intensity variation of Raman peak at 230 $cm^{-1}$ with molar concentration.*

For quantitative analysis we need to identify the characteristic Raman lines for the molecules so that these lines could be used as reference lines for intensity comparison. The Raman lines at 1570 $cm^{-1}$ for R6G and 1584 $cm^{-1}$ for CV were taken as reference lines since these have the highest intensity. The intensities of these lines were obtained by carrying out Lorentzian fits to these peaks. The intensity values of these lines were

plotted against the molar concentrations. The data are illustrated in figures 3.11 and 3.12. A linear fit was made to these data points with a good correlation ($R^2$ values are 0.948, 0.964 for CV and R6G, respectively) between intensity and concentrations of R6G and CV, which provides a calibration curve for quantitative detection of R6G and CV.

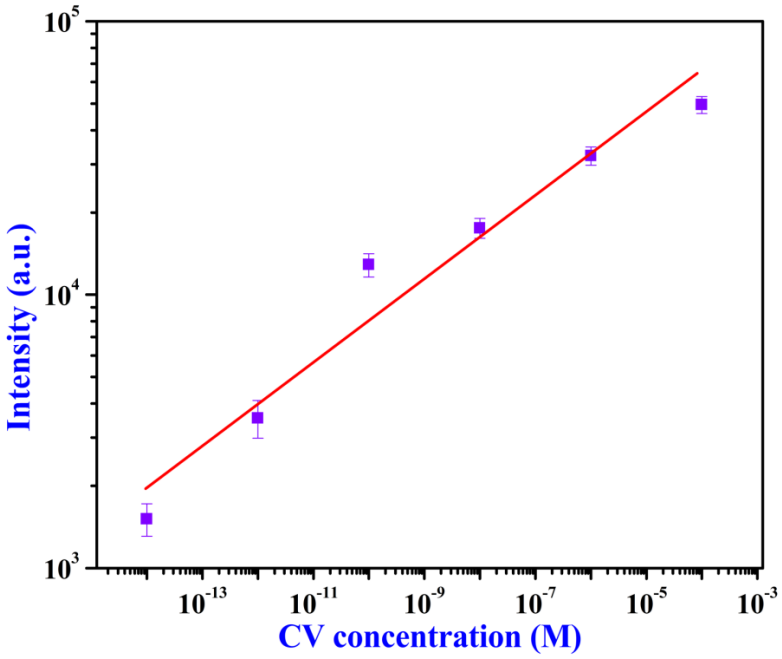


*Figure 3.12: Intensity variation of the Raman peak at 1584 $cm^{-1}$ for SERS spectra of CV as a function of molar concentration.*

Also the inset of figure 3.11 depicts the intensity of the Ag-N binding peak that was taken to indicate the attachment of the analyte molecule to the silver surface. The intensity of this line also correlates well with the molar concentration of the analyte which indicates that all the analyte molecules attach to the surface of the nanoparticle.

### 3.6 Reproducibility of signal over the SERS substrates:

Reproducibility refers to the ability to produce enhanced signal for different substrates and at various locations of the same substrate with a minimum intensity variation. The spectra would be reproducible only when the molecules are oriented in a particular direction at all hot spots. That could happen only when the molecules are chemically attached to the metal nanoparticles and there is a uniform distribution of hot-spots on the substrates. We recorded the SERS spectra on several substrates and at several positions on the same substrate for a particular concentration of CV.

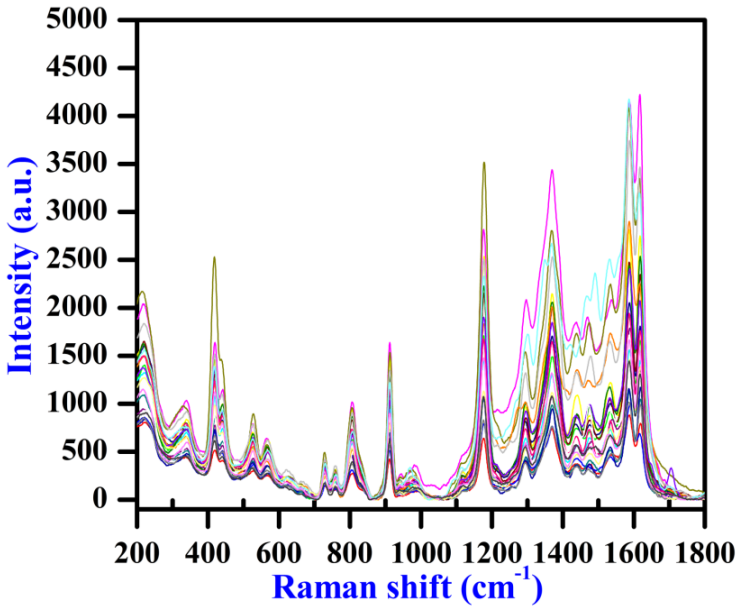


*Figure 3.13: Reproducible SERS spectra of $10^{-6}$M of CV adsorbed Ag nanocluster surface. The spectra are measured at different locations on the same substrate.*

The reproducible SERS spectra for 1μM concentration of CV are depicted in figure 3.13. This shows that our nanocluster substrates give good reproducible measurements.

## 3.7 Conclusions:

We have been able to synthesize very efficient SERS-active substrates using a cluster deposition system based on inert gas phase condensation technique. We observed that SERS substrates prepared by an 8 minute nanocluster deposition time followed by a heat treatment of 300 $^{o}$C for two hours gave the best Raman signal enhancement. The analytical enhancement factor for these substrates was found to be $10^{12}$ which is the best enhancement factor obtained so far by any group. The limits of detection of R6G and CV molecules using these substrates were $10^{-16}$ M and $10^{-18}$ M, respectively. Quantitative measurements were also carried out on these substrates for these two dye molecules in the concentration range $10^{-4}$ M to $10^{-16}$ M. The results show a linear correlation between intensity and molar concentration. The present substrates have also shown good reproducibility.

## References:

[1] D.K. Lim, K.S. Jeon, J.H. Hwang, H. Kim, S. Kwon, Y.D. Suh and J.M. Nam, "Highly uniform and reproducible surface-enhanced Raman scattering from DNA-tailorable nanoparticles with 1-nm interior gap" *Nat. Nanotechnol. 6 (2011) 452.*

[2] X. Liu, Y. Shao, Y. Tang and K.F. Yao, "Highly Uniform and Reproducible Surface Enhanced Raman Scattering on Air-stable Metallic Glassy Nanowire Array" *Sci. Rep. 4 (2014) 5835.*

[3] M. Mandal, N.R. Jana, S. Kundu, S.K. Gosh, M. Panigrahi and T. Pal, "Synthesis of $Au_{core}$-$Ag_{shell}$ type metallic nanoparticles for single molecule detection in solution by SERS method" *J. Nanopart. Res. 6 (2004) 53.*

[4] L. Rivas, S. Sanchez-Cortes, J.V. Garcia-Ramos and G. Morcillo, "Growth of Silver Colloidal Particles Obtained by Citrate Reduction to Increase Surface Enhancement Factor" *Langmuir 17 (2001) 574.*

[5] U. Nickel, A. Castell, K. Pöppl and S. Schneider, "A Silver Colloid Produced by Reduction with Hydrazine as Support for Highly Sensitive Surface-Enhanced Raman Spectroscopy" *Langmuir 16 (2000) 9087.*

[6] S. Nie and S. Emory, "Probing Single Molecules and Single Nanoparticles by Surface-Enhanced Raman Scattering" *Science 275 (1997) 1102.*

[7] X.X. Han, G.G. Huang, B. Zhao and Y. Ozaki, "Label-Free Highly Sensitive Detection of Proteins in Aqueous Solutions Using Surface Enhanced Raman Scattering" *Anal. Chem. 81 (2009) 3329.*

[8] M.W. Shao, L. Lu, H. Wang, S. Wang, M.L. Zhang, D.M. Dorothy and S.T. Lee, "An ultrasensitive method: surface-enhanced Raman scattering of Ag nanoparticles from β- silver vanadate and copper" *Chem. Commun. 20 (2008) 2310.*

[9] S.L. Kleinman, E. Ringe, N. Valley, K.L. Wustholz, E. Philips, K.A. Scheidt, G.C. Schatz and R.P. Van Duyne, "Single-Molecule Surface-Enhanced Raman Spectroscopy of Crystal Violet Isotopologues: Theory and Experiment" *J. Am. Chem. Soc. 133 (2011) 4115*.

[10] T. Vystavel, G. Palasantzas, S.A. Koch and J.Th.M. De Hosson, "Nanosized iron clusters investigated *in situ* transmission electron microscopy" *Mater. Chem. Phys. 64 (2000) 241.*

[11] T.K. Sau, A.L. Rogach, F. Jäckel, T.A. Klar and J. Feldmann, "Properties and Applications of Colloidal Nanospherical Noble Metal Nanoparticles" *Adv. Mater. 22 (2010)1805.*

[12] A.M. Michaels, J. Jiang and L. Brus, "Ag Nanocrystal Junction as the Site for Surface-Enhanced Raman Scattering of Single Rhodamine 6G Molecules" *J. Phys. Chem. B 104 (2000) 11965.*

[13] P. Hildebrandt and M. Stockburger, "Surface-Enhanced Resonance Raman Spectroscopy of Rhodamine 6G adsorbed on Colloidal Silver" *J. Phys. Chem. 88 (1984) 5935.*

[14] B. Mondal and S.K. Saha, "Fabrication of SERS substrate using nanoporous anodic alumina template decorated by silver nanoparticles" *Chem. Phys. Lett. 497 (2010) 89.*

[15] N. Horimoto, N. Ishikawa and A. Nakajima, "Preparation of a SERS substrate using vacuum-synthesized silver nanoparticles" *Chem. Phys. Lett. 413 (2005) 78.*

[16] A. Kudelski, "Raman studies of rhodamine 6G and crystal violet sub-monolayers on electrochemically roughened silver substrates: Do dye molecules adsorb preferentially on highly SERS-active sites?" *Chem. Phys. Lett. 414 (2005) 271.*

[17] K. Kneipp and H. Kneipp, "Single Molecule Raman Scattering" *Appl. Spectrosc. 60 (2006) 322A.*

[18] J.A. Dieringer, K.L. Wustholz, D.J. Masiello, J.P. Camden, S.L.Kleinman, G.C. Schatz and R.P. Van Duyne, "Surface-Enhanced Raman Excitation Spectroscopy of a Single Rhodamine 6G Molecule" *J. Am. Chem. Soc. 131 (2009) 849.*

[19] E.C. Le Ru, E. Blackie, M. Meyer and P.G. Etchegoin, "Surface Enhanced Raman Scattering Enhancement Factors: A Comprehensive Study" *J. Phys. Chem. C 111 (2007)13794.*

[20] F.A Harraz, A.A. Ismail, H. Bouzid, S.A. Al-Sayari, A. Al-Hajry and M.S. Al-Assiri, "Surface-enhanced Raman Scattering (SERS)-active substrates

from silver plated-porous silicon for detection of crystal violet" *Appl. Surf. Sci. 331 (2015) 241.*

[21] K.J. Khajehpour, T. Williams, L. Bourgeois and S. Adeloju, "Gold nanothorns–macroporous silicon hybrid structure: a simple and ultrasensitive platform for SERS" *Chem. Commun. 48 (2012) 5349.*

[22] J. Jiang, L. Ou-Yang, L. Zhu, J. Zou and H. Tang, "Novel one-pot fabrication of lab-on a-bubble@Ag substrate without coupling-agent for surface enhanced Raman scattering" *Sci. Rep. 4 (2014) 3942.*

[23] R.M. Liu, Y.P. Kang, X.F. Zi, M.J. Feng, M. Cheng and M.Z. Si, "The ultratrace detection of crystal violet using surface enhanced Raman scattering on colloidal Ag nanoparticles prepared by electrolysis" *Chin. Chem. Lett. 20 (2009) 711.*

[24] Raju Botta, G. Upender, R. Sathyavathi, D. Narayana Rao and C. Bansal, "Silver nanoclusters films for single molecule detection using Surface Enhanced Raman Scattering (SERS)" *Mater. Chem. Phys. 137 (2013) 699.*

[25] S. Senapati, S.K. Srivastava, S.B. Singh and A.R. Kulkarni, "SERS active Ag encapsulated Fe@SiO2 nanorods in electromagnetic wave absorption and crystal violet detection" *Environ. Res. 135 (2014) 95.*

[26] W. Meng, F. Hub, L.-Y. Zhang, X.-H. Jiang, L.-D. Lu and X. Wang, "SERS and DFT study of crystal violet" *J. Mol. Struc. 1035 (2013) 326.*

[27] C. Liu, S. Wang, G. Chen, S. Xu, Q. Jia, J. Zhou and W. Xu, "A surface-enhanced Raman scattering (SERS)-active optical fiber sensor based on a three-dimensional sensing layer" *Sens. Bio-Sens. Res. 1 (2014) 8.*

[28] D. Zhang, X. Liu and X. Wang, "Synthesis of single-crystal silver slices with predominant (1 1 1) facet and their SERS effect" *J. Mol. Str. 985 (2011) 82.*

[29] R. Sancı and M.Volkan, "Surface-enhanced Raman scattering (SERS) studies on silver nanorod substrates" *Sens. Actuators B 139 (2009) 150.*

[30] M.K. Hossain, K. Shibamoto, K. Ishioka, M. Kitajima, T. Mitani and S. Nakashima, "2D nanostructure of gold nanoparticles: an approach to SERS-active substrate" *J. Lumin. 122–123 (2007) 792.*

[31] G. Upender, R. Sathyavathi, B. Raju, C. Bansal and D. Narayana Rao, "SERS study of molecules on Ag nanocluster films deposited on glass and silicon substrates by cluster deposition method" *J. Mol. Struc. 1012 (2012) 5.*

[32] K. Kneipp, Y. Wang, H. Kneipp, L.T. Perelman, I. Itzkan, R.R. Dasari, and M.S. Feld, "Single Molecule Detection Using Surface-Enhanced Raman Scattering (SERS)" *Phy. Rev. Lett. 78 (1997) 1667.*

[33] A. Otto, "What is observed in single molecule SERS, and why?" *J. Raman. Spectrosc. 33 (2002) 593.*

[34] P.G. Etchegion, M. Meyer and E.C. Le Ru, "Statistics of single molecule SERS signals: is there a Poisson distribution of intensities?" *Phys. Chem. Chem. Phys. 9 (2007) 3006.*

[35] A.M. Michaels, M. Nirmal and L.E. Brus, "Surface Enhanced Raman Spectroscopy of Individual Rhodamine 6G Molecules on Large Ag Nanocrystals" *J. Am. Chem. Soc. 121 (1999) 9932.*

[36] C.J.L. Constantino, T. Lemma, P.A. Antunes and R. Aroca, "Single-Molecule Detection Using Surface-Enhanced Resonance Raman Scattering and Langmuir−Blodgett Monolayers" *Anal. Chem. 73 (2001) 3674.*

[37] H. Liu, L. Zhang, X. Lang, Y. Yamaguchi, H. Iwasaki, Y. Inouye, Q. Xue and M. Chen, "Single molecule detection from a large-scale SERS-active Au79Ag21 substrate" *Sci. Rep. 112 (2011) 1.*

[38] M. Futamata, Y. Maruyama and M. Ishikawa, "Metal nanostructures with single molecule sensitivity in surface enhanced Raman scattering" *Vib. Spectrosc. 35 (2004) 121.*

[39] G. Haran, "Single-Molecule Raman Spectroscopy: A Probe of Surface Dynamics and Plasmonic Fields" *Acc. Chem. Res. 43 (2010) 1135.*

[40] M. Futamata, Y. Maruyama and M. Ishikawa, "Adsorbed Sites of Individual Molecules on Ag Nanoparticles in Single Molecule Sensitivity-Surface-Enhanced Raman Scattering" *J. Phys. Chem. B 108 (2004) 13119.*

[41] Z.Q. Tian, Z.L. Yang, B. Ren, J.F. Li, Y. Zhang, X.F. Lin, J.W. Hu and D.W. Wu, "Surface-enhanced Raman scattering from transition metals with special surface morphology and nanoparticle shape" *Faraday Discuss. 132 (2006) 159.*

[42] M. Futamata, Y. Maruyama and M. Ishikawa, "Critical importance of the junction in touching Ag particles for single molecule sensitivity in SERS" *J. Mol. Struct. 735 (2005) 75.*

[43] Y. Sharaabi, T. Shegai and G. Haran, "Two-state analysis of single-molecule Raman spectra of crystal violet" *Chem. Phys. Lett. 318 (2005) 44.*

# Chapter 4

## SERS activity of Ag nanoclusters on different substrates

*In this chapter we would like to present our work on SERS activity of the Ag nanoclusters on different substrates viz. glass, alumina and silicon. SERS activities on these substrates were evaluated by Rhodamine B (RhB) dye molecule. The various factors for SERS enhancement such as nature of substrate, nanoclusters size and shape and roughness of the substrate are discussed. It has been concluded that the SERS enhancement is greater for glass substrate as compared to other substrates. Some of the results are published in Journal of Molecular structure*[1].

[1] *G. Upender, R. Satyavathi, B. Raju, C. Bansal and D. Narayana Rao, J. Mol. Struc. 1012 (2012)56.*

## 4.1 Introduction:

In the previous chapter, we have discussed the optimization methods for preparation of nanoclusters substrate by varying the deposition time and annealing temperature. As discussed in chapter 1, the SERS intensity depends on the localized surface Plasmon resonance (LSPR), which is dependent on nanoparticle size, shape, interparticle separation and dielectric environment [1]. These factors have to be chosen carefully to ensure high enhancement factors of the substrates.

Very few studies have been published on the influence of the type and nature of the substrates on SERS measurements [2, 3]. In the present chapter we will discuss the effect of the substrate: glass, alumina ($Al_2O_3$) and p-type silicon (Si) wafer on SERS signal enhancement. Comparisons of signal enhancements, reproducibility and uniformity of the substrates are discussed in this chapter.

## 4.2 SERS-active substrates preparation and surface morphological studies:

Ag nanoclusters were deposited on glass, alumina and silicon substrates using the cluster deposition system based on inert gas phase condensation method discussed earlier. All the substrates were annealed at 300 °C for 2 hours in the presence of argon atmosphere. FESEM images of annealed Ag nanoclusters on glass, alumina and silicon substrates are displayed in figure 4.1.

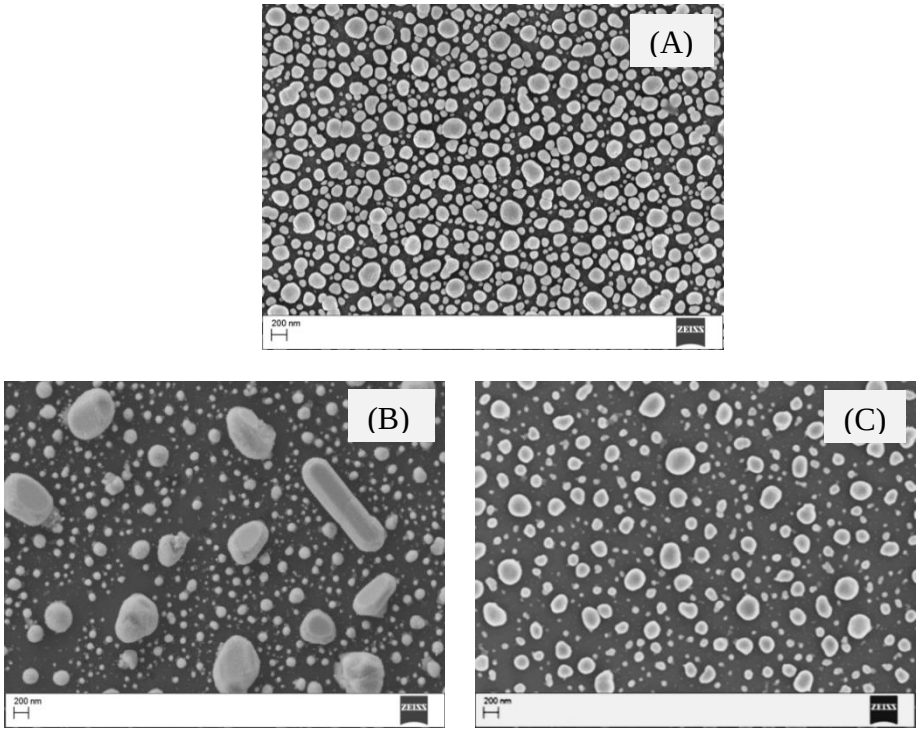


*Figure 4.1: FESEM image of annealed Ag nanoclusters on (A) glass (B) alumina and (C) silicon substrates.*

From these micrographs we observe that different nanocluster shapes and sizes are present on these substrates. Especially, alumina substrate contains different shapes like nanorods and spheroids with different sizes. The substrates have irregular cluster shapes or consist of aggregates with a large size distribution. Nanoclusters on silicon substrates (Figure 4.1(C)) are less dispersive compared to other substrates.

Surface roughness also plays a role in signal enhancement. The surface roughness of the substrates was measured using Atomic Force Microscopy (AFM). Figure 4.2 evidences the micrographs of the bare substrates (without nanoclusters on substrates) surface employing AFM. From these micrographs it is observed that the surface roughness of silicon

is smooth compare to other substrates.

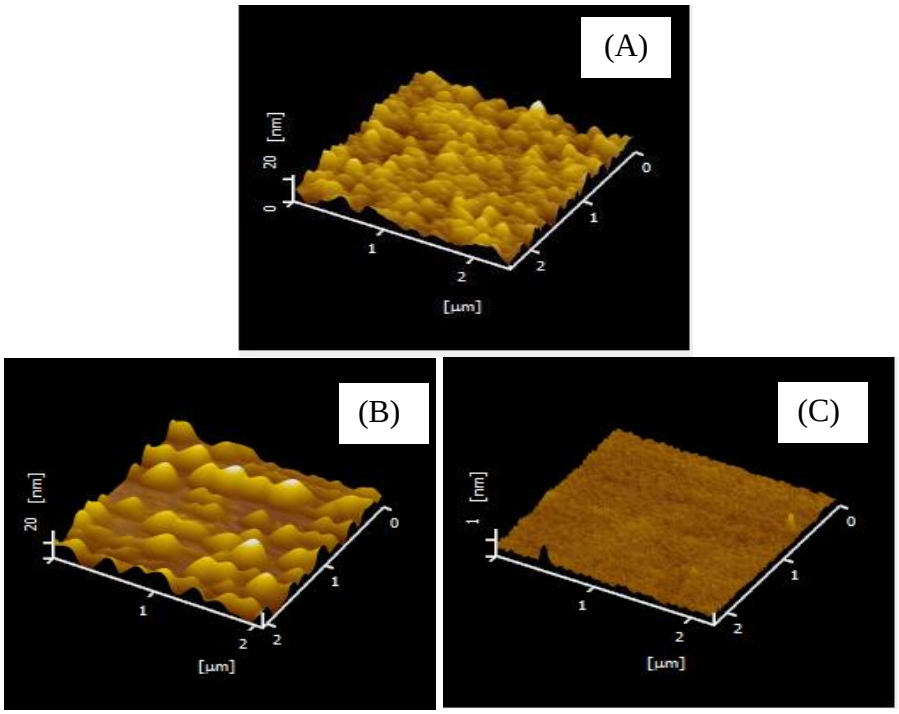


*Figure 4.2: AFM images of (A)gGlass (B) alumina and (C) silicon bare substrates.*

Optical measurements were carried out on these substrates using UV-Vis spectrophotometer. Figure 4.3 illustrates the absorption spectrum obtained for these samples. Panel (A) of this figure depicts this spectrum, for the nanoclusters observed on glass substrates, highlights two peaks at 470 nm and 380 nm and the former is due to dipolar oscillations arising from smaller size nanoclusters whereas the latter is due to quadrupolar oscillation of bigger size nanoclusters [4]. As the silicon and alumina substrates have reflecting surface, we have recorded the reflectance spectra for them. Absorbance *(A)* was calculated from the reflectance *(R)* using the formula *A=1-R*, assuming transmittance *(T)* is zero.

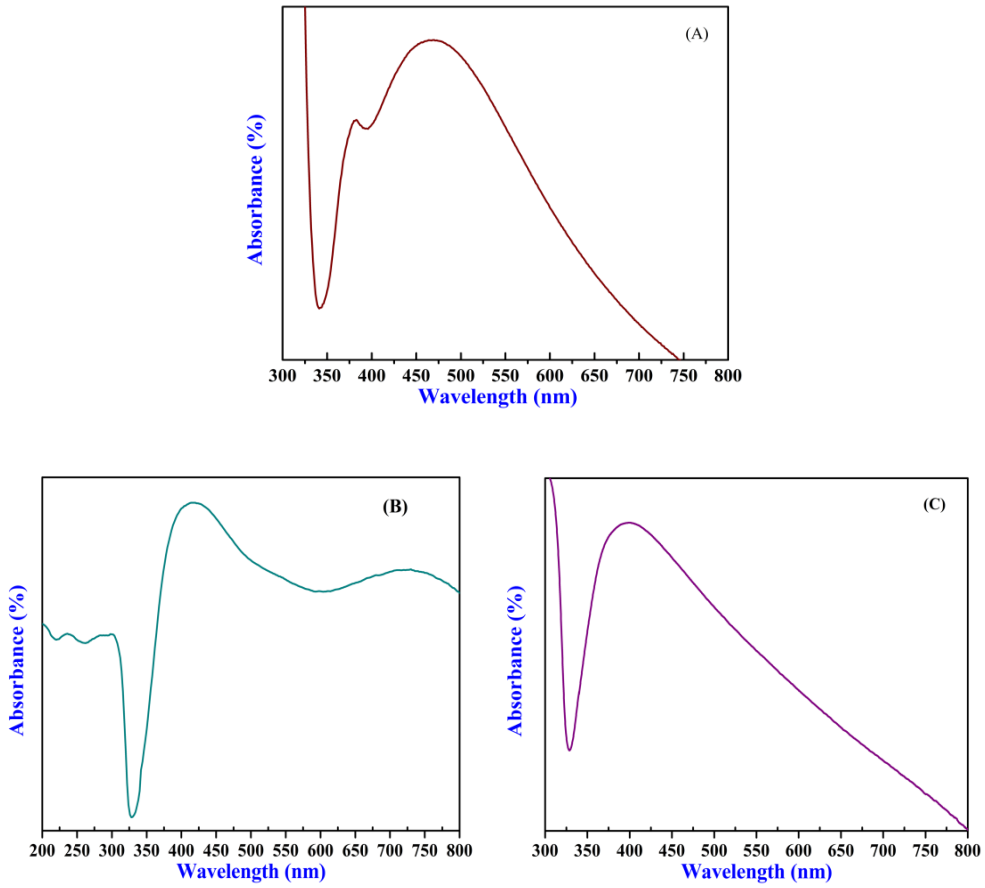


*Figure 4.3: Absorbance spectrum of Ag nanoclusters on (A) glass (B) alumina and (C) silicon substrates.*

Frequency of the surface plasmon modes are excited depending on factors such as the particle shape and size, electron density, electron effective mass, the dielectric constant of the particle and the dielectric constant of the medium in which the particle is situated. These effects have been taken into account separately by different authors [5-7]. The plasmon peaks in the alumina substrate are considerably broadened and occur at 414 nm and 730 nm for the quadrupolar and dipolar resonances, respectively. Thus there is a red shift with increase in the dielectric constant of the medium. As a

contrast, in case of silicon substrate the absorption spectrum is broad and no clear peaks are observed. This is due to the large dielectric constant of silicon and as explained by Noguez [5] this causes a large red shift and also a broadening of the plasmon resonance.

### 4.3 Comparison of SERS efficiencies of the substrates:

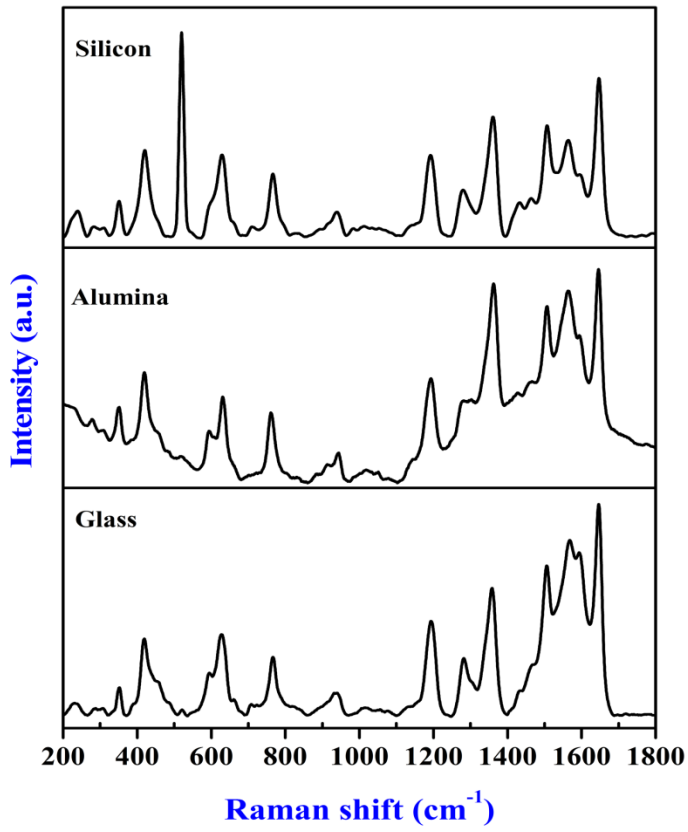


*Figure 4.4: SERS spectra of 1μM RhB adsorbed on different substrates and recorded with laser excitation wavelength of 514.5 nm.*

A 1μM aqueous solution of Rhodamine B (RhB) was used as an analyte to test the SERS efficiencies on these substrates. 10 μL of the analyte was dropped on these substrates and allowed to dry. Raman measurements were carried out at laser excitation wavelength of 514.5 nm.

SERS spectra of RhB for the three substrates are shown in figure 4.4. The peaks appearing at 630 $cm^{-1}$, 1194 $cm^{-1}$, 1284 $cm^{-1}$, 1361 $cm^{-1}$, 1504 $cm^{-1}$ and 1643 $cm^{-1}$ are the characteristic Raman lines of RhB and in good agreement with the previous reports [8, 9]. The intense Raman lines in the spectra are mostly aromatic C-C stretching vibrations. The complete peak assignments are summarized in the table 4.1.

*Table 4.1: Peak assignments of RhB molecule.*

| Raman line ($cm^{-1}$) | Assignment |
|---|---|
| **623** | Aromatic bending |
| **1194** | Aromatic C-H bending |
| **1284** | C-C bridge bands stretching |
| **1361** | Aromatic C-C stretching |
| **1504** | Aromatic C-C stretching |
| **1643** | Aromatic C-C stretching |

To study the SERS efficiencies of the substrates we compared the intensities of the Raman lines at 1359 $cm^{-1}$, 1504 $cm^{-1}$ and 1646 $cm^{-1}$ on the different substrates. The intensities of these Raman lines were obtained by fitting the Lorentzian to the peaks and finding the areas under them. A comparison of Raman lines intensities on these substrates is depicted in figure 4.5 from which we observe that nanoclusters on glass and alumina substrates show higher enhancement compared to silicon. But when it is compared with alumina, glass has the highest enhancement. The reason for higher enhancement for glass and alumina as compared to Si is due to the relative conductivity of the substrates. Silicon has a higher conductivity as compared to glass and alumina. The localized surface plasmons of a metal

particle located on a conducting substrate can propagate along the conducting surface and reduce the localization and coupling of the local electromagnetic field. This leads to a weakening of the enhancement of Raman intensity [10]. The enhancement also depends to some extent on the surface roughness of the substrate (Figure 4.2). A rough surface can accommodate a larger number of clusters due to an increase in the effective surface area. The glass and alumina surfaces are observed to have a higher surface roughness and give a better signal enhancement as compared to silicon.

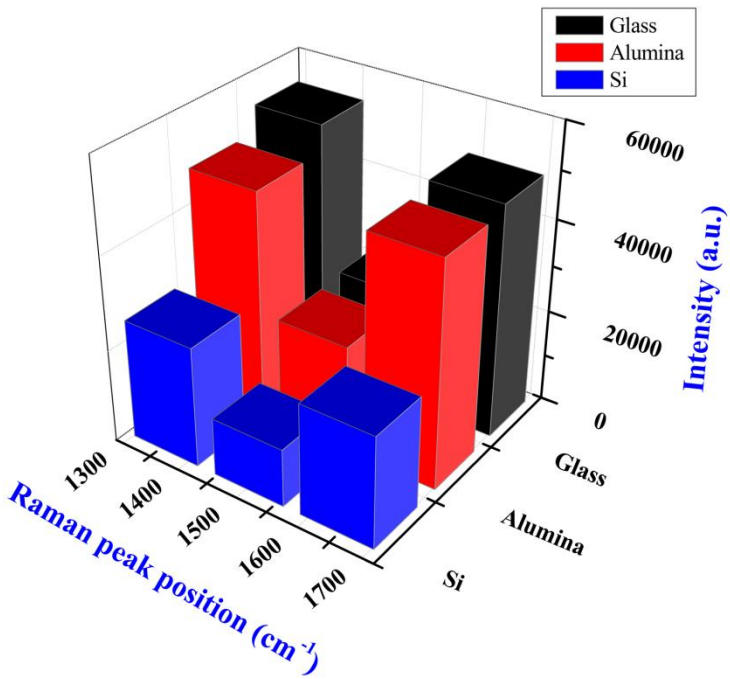


*Figure 4.5: Comparison of intensities of Raman lines at 1359 $cm^{-1}$, 1504$cm^{-1}$ and 1643 $cm^{-1}$ of RhB adsorbed on glass, alumina and silicon substrates.*

Since, nanoclusters on glass substrates give the best signal enhancement as compared to the other substrates glass substrates were used in all the studies.

### 4.4 Reproducibility of the signal over the substrates:

In the field of SERS, reproducibility (the ability to produce minimum variations in SERS signal intensities from place to place) and repeatability are two challenging things. Reproducibility of these substrates was measured by recording the Raman spectra at different locations on these substrates. Figures 4.6 - 4.8 show the spectra of recorded data at different places on the substrates. Each curve in the spectra reveals the strong characteristic peaks of RhB at 1μM and it demonstrates the outstanding reproducibility and uniformity of the substrate.

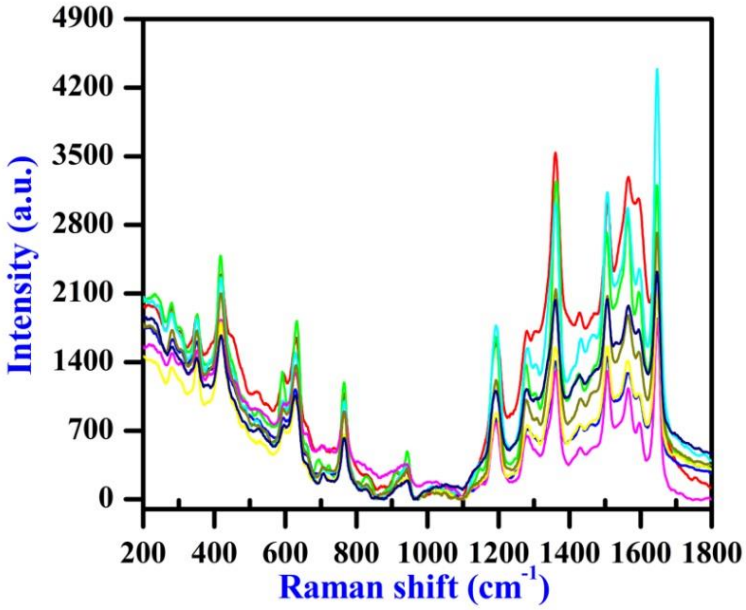


*Figure 4.6: Reproducible SERS spectra of 1μM RhB on glass substrate, at different locations on the substrate.*

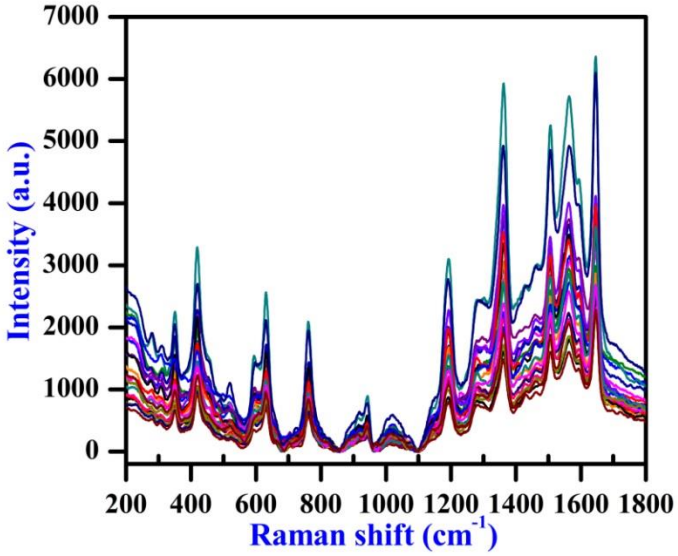


*Figure 4.7: Reproducible SERS spectra of 1μM RhB on alumina substrate, at different locations on the substrate.*

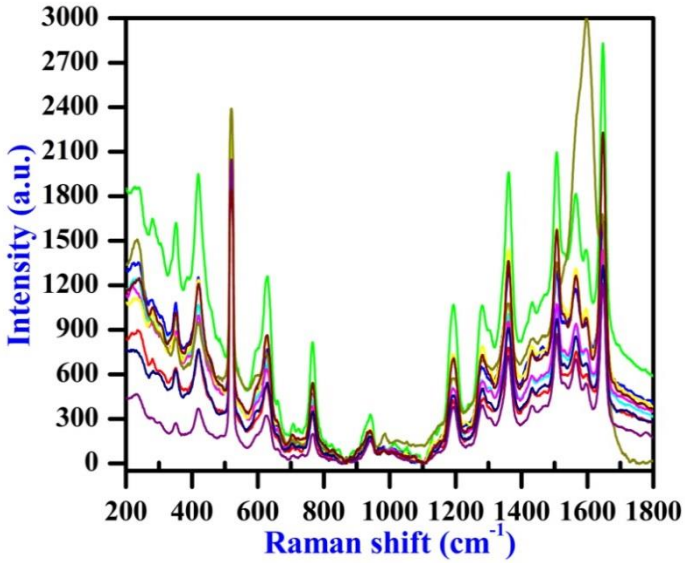


*Figure 4.8: Reproducible SERS spectra of 1μM RhB on silicon substrate, at different points on the substrate.*

To assess quantitatively the reproducibility and uniformity of these SERS signals, the relative standard deviation (RSD) of the dominant characteristic peaks intensity was calculated. The intense Raman lines at 630 $cm^{-1}$, 1194 $cm^{-1}$, 1360 $cm^{-1}$, 1504 $cm^{-1}$, and 1643 $cm^{-1}$ were taken as a reference lines to calculate RSD. The intensities of these Raman lines were calculated by carrying out a Lorentzian fit to the peaks and finding the areas under the peaks. From the intensity values we calculated the RSD and these values are displayed in table 4.2.

*Table 4.2: Relative standard deviation (RSD) of Raman intensities of intense vibrational modes of RhB at 630 $cm^{-1}$, 1194 $cm^{-1}$, 1360 $cm^{-1}$, 1504 $cm^{-1}$ and 1643 $cm^{-1}$ on the substrates.*

| Substrate | Raman Peak | | | | |
|---|---|---|---|---|---|
| | 630 $cm^{-1}$ | 1194 $cm^{-1}$ | 1360 $cm^{-1}$ | 1504 $cm^{-1}$ | 1643 $cm^{-1}$ |
| | RSD (%) | RSD (%) | RSD (%) | RSD (%) | RSD (%) |
| glass | 15.4 | 17.46 | 18.94 | 12.56 | 12.58 |
| alumina | 21.46 | 20.97 | 26.38 | 22.22 | 19.84 |
| silicon | 14.92 | 19.70 | 23.21 | 18.49 | 14.78 |

From the above table, we see that the glass substrates have the lowest RSD values and therefore are the best suited for SERS measurements.

## 4.5 Conclusions:

Ag nanoclusters were deposited on glass, alumina and silicon substrates under the same conditions. The glass substrates were found to be the most appropriate substrates for signal enhancement, reproducibility and uniformity.

## References

[1] G. Das, F. Mecarini, F. Gentile, F.D. Angelis, Mohan Kumar HG, P. Candeloro, C. Liberale, G. Cuda and E.D. Fabrizio, "Nano-patterned SERS substrate: Application forprotein analysis vs. temperature" *Biosens. Bioelectron. 24 (2009) 1693.*

[2] L.C. Shoute, A.J. Bergren, A.M. Mahmoud, K.D. Harris and R.L. McCreery, "Optical Interference Effects in the Design of Substrates for Surface-Enhanced Raman Spectroscopy" *Appl. Spectrosc. 63 (2009) 133.*

[3] A. Merlen, V. Chevallier, J.C. Valmalette, L. Patrone, P. Torchio, S. Vedraine, F. Flory and G. Moula, "Surface enhanced spectroscopy with gold nanostructures on silicon and glass substrates" *Surf. Sci. 605 (2011) 1214.*

[4] T.K. Sau, A.L. Rogach, F. Jäckel, T.A. Klar and J. Feldmann, "Properties and Applications of Colloidal Nanospherical Noble Metal Nanoparticles" *Adv. Mater. 22 (2010)1805.*

[5] C. Noguez, "Surface Plasmons on Metal Nanoparticles: The Influence of Shape and Physical Environment" *J. Phys. Chem. C 111 (2007) 3806.*

[6] K.A. Willets and R.P. Van Duyne, "Localized Surface Plasmon Resonance Spectroscopy and Sensing" *Annu. Rev. Phys. Chem. 58 (2007)267.*

[7] E. Ringe et. al, "Plasmon Length: A Universal Parameter to Describe Size Effects in Gold Nanoparticles" *J. Phys. Chem. Lett. 3 (2012) 1479.*

[8] J. Zhang, X. Li, X. Sun and Y. Li, "Surface enhanced Raman scattering effects of silver colloids with different shapes" *J. Phys. Chem. B 109 (2005) 12544.*

[9] B. Guo, G. Han, M. Li and S. Zhao, "Deposition of the fractal-like gold particles onto electrospun polymethylmethacrylate fibrous mats and their application in surface-enhanced Raman scattering" *Thin Solid*

*Films 518 (2010) 3228.*

[10] H. Qian, Z. Xiao-Dan, Z. He, X. Shao-Zhen, G. Wei-Dong, G. Xin-Hua and Z. Ying, "Influence of local environment on the intensity of the localized surface plasmon polariton of Ag nanoparticles" *Chin. Phys. B 19 (2010) 047304.*

# Chapter 5

## SERS application in D-glucose sensing and quantification

*Direct detection of glucose by SERS is a highly challenging problem because of a small Raman scattering cross-section for glucose and its low affinity towards attachment on metal nanoparticle surface. In this chapter we describe how to attach glucose molecule to the metal nanoparticle surface by using 2-Thienylboronic acid as a linker molecule. SERS measurements were carried out using a laser excitation wavelength of 632.8 nm. Glucose molecules were detected down to micro molar concentrations. It is shown here that it is possible to quantify the glucose concentration through the intensity of a new Raman line that develops in the Raman Spectrum of (D-glucose+2TBA). These results would help in the development of a sensor for non-invasive glucose sensing.*

## 5.1. Introduction:

Diabetes is a metabolic disease which affects millions of people worldwide resulting in long-term health disorders, mainly cardiovascular diseases and blindness [1]. It is one of the most leading causes for death in the world, according to the IDF Diabetes Atlas published by the International Diabetes Federation in 2013 [2], over 380 Million people were affected with Diabetes across the world (68 Million in India), and it caused around 5.1 Million deaths in 2013 i.e., every six seconds a person died from diabetes. More than 21 Million live births were affected by diabetes during pregnancy in 2013. It is also estimated that people living with diabetes will increase to 55% by 2035, (figure 5.1).

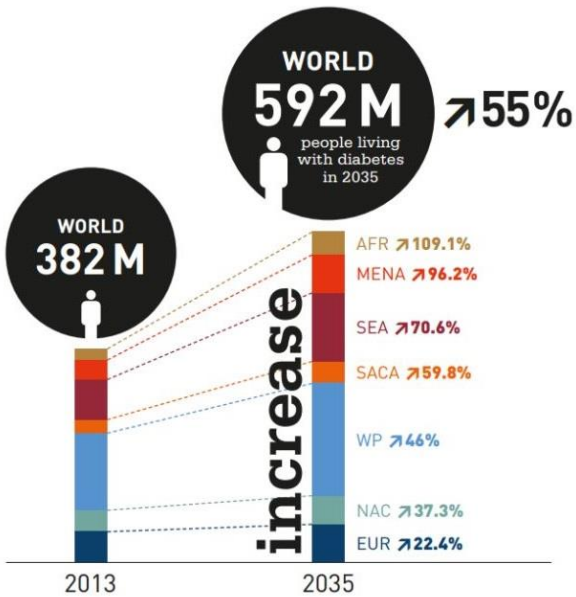


*Figure 5.1: World population living with diabetes increment in 2035. Source: IDF Diabetes Atlas Sixth Edition, International Diabetes Federation 2013, AFR: Africa, MENA: Middle East and North Africa, SEA: South-East Asia, SACA: South and Central America, WP: Western Pacific, NAC: North America and Caribbean, EUR: Europe*

Glucose levels in blood or other body fluids in humans have to be monitored in order to control the glucose levels and avoid the associated medical risks. Various kinds of devices are available in the market for detection of glucose in blood. Such devices are based on the electrochemical [3], colorimetric [4], optical [5] and fluorescence methods [6]. Among these, electrochemical method have attracted more attention compared to others due to high sensitivity, reasonable selectivity, low cost and low limit of detection [7]. Selectivity and biocompatibility is increased by the modification of electrodes with polymeric membrane [8], fullerene-$C_{60}$ [9, 10], carbon nanotubes [11-13], and graphene materials [14-16]. Hydrophilic oxidants like ascorbic acid and uric acids are present in the human blood plasma and interfere with electrochemical signal and hydrogen peroxide also inactivates the electrode [17, 18]. This affects the sensitivity and reliability of the electrochemical glucose sensors [19]. Moreover the existing method of acquiring blood samples by finger-prick is painful (invasive) and needs specific tools [20]. To reduce the invasive nature, body fluids like sweat, tears, urine and saliva can be considered as alternative samples for the D-glucose detection [21-23]. Glucose concentration levels in the body fluids are very low compared to the levels in the blood and hence, it is highly challenging to measure the glucose concentration in the body fluids. The glucose levels in saliva are about 80 μM for normal persons and about 200 μM for diabetic patients [24]. In urine the glucose concentration level varies from 50 μM to 800 μM for normal persons [25] and increases when the blood glucose level increases for diabetic patients. There is therefore a need to develop a glucose biosensor for body fluids by improving the lower limit of detection and reliability of the sensing.

Optical biosensors have been considered as an alternative option to determine glucose concentration because they have many advantages like low-cost, relatively high molecular specificity and lesser invasive character [26, 27]. However, it has some drawbacks like high limit of detection, false positive signals, and vulnerability to interferences particularly by mid infra-red wavelengths. Raman sensors can overcome the interference problem with aqueous solution, but its sensitivity is very low due to inefficient Raman scattering for trace analyte detection. Nanostructured materials have erased this insufficient Raman scattering by generating Surface Enhanced Raman Scattering (SERS). Nanostructured-based SERS sensors are attractive due to their simple sample preparation methods. In SERS the background signal of water that is usually present in the IR spectroscopy is eliminated and a high sensitivity resulting from plasmonic nanostructures is achieved. One important application of SERS is bio sensing, particularly glucose sensing, which has a high impact in bio sensing research. Therefore, extensive efforts have been made towards the development of SERS based glucose sensors [28-40].

Direct glucose detection by Raman Spectroscopy is very difficult due to the low scattering cross-section of glucose molecule, so if we want to exploit the signal enhancement by SERS we have to bring the analyte molecule in close proximity to a metal nanoparticle surface. Richard P. Van Duyne's research group proposed a method to bring the glucose molecules close to the metal nanoparticle surface or within the field enhancement of localized surface plasmon resonance (LSPR) by partitioning the surface with alkanethiol aggregated on Ag film over nanosphere [30]. Further, decanthiol was mixed with mercaptohexanol [41] partition layer and it improved the

temporal stability, reversibility, and ease of control and allowed *in vivo* monitoring of glucose concentration in the interstitial fluids of rats [34, 36, 42].

The problem of low Raman cross section of glucose was also addressed by using carbohydrate recognition molecules such as boronic acids and placing the molecule complex in the alkane thiol partition layers. In another method alkyne functionalized boronic acid molecule and 4-mercaptophenyl boronic acid [43] were used to form a complex with the D-glucose molecule to attach with the silver deposited on polystyrene spheres. The Raman signals from the alkyne radical were measurable only up to 0.5 mM concentration levels.

These methods have some disadvantages. The first method measures the SERS signals from the D-glucose concentrated near the metal surface. However, the D-glucose Raman signal is still very weak and cannot be used to quantify D-glucose concentration. The drawback of the other method is that the SERS signals from the alkyne group are measured and it is therefore an indirect method of measuring the D-glucose concentration.

We chose 2-Thienylboronic acid (2-TBA) (see figure 5a for the structure of this molecule) as a linker molecule that allows us to attach the sulfur atom of the thienyl group to the silver surface and the OH-B-OH part of the molecule to the D-glucose molecule. The proposed interaction mechanism is shown in figure 5.2. The two hydroxyl groups of 2-TBA attach to the two carbon atoms of D-glucose and form 2-thienylboroglucose molecule via ester linkage. This method is a direct detection method as the

D-glucose molecule is attaching and influencing the properties of the linker molecule directly and enhancing the Raman signal intensity.

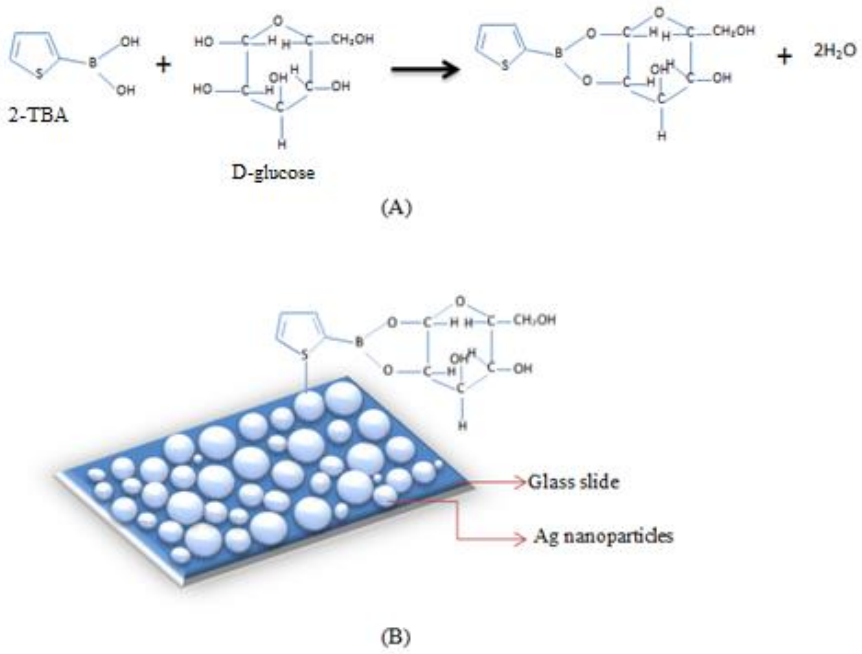


*Figure 5.2: Schematic diagrams depicting (A) the bonding between the 2-TBA and D-glucose and (B) the attachment of the 2-TBA+D-glucose molecule to the silver surface via. Ag-S bond.*

## 5.2 Material and Methods:

2-TBA and D-glucose powders were purchased from Sigma Aldrich and used without further purification. First, a 0.1 M stock solution of 2-TBA was prepared and stored. Different molar concentrations (500 μM to 1 μM) of D-glucose were prepared by sequential dilution method starting with a 0.1 mM solution. Analyte solutions were prepared by mixing 500 μL of the 0.1 M 2-TBA solution and 250 μL solutions of D-glucose solutions of different molar concentrations. 50 μL of the analyte solution was dropped on the Ag nanocluster substrate and allowed to dry under ambient conditions.

## 5.3 Results and Discussion:

We first carried out SERS measurements on different molar concentrations of 2-TBA (decimole to micromole) and D-glucose (millimole to micromole). From these measurements we observed that 0.1 M concentration of 2TBA with different molar concentrations of D-glucose showed all the characteristic peaks of D-glucose. The possible reason for this is that the surface coverage of 2-TBA on Ag nanoclusters may be optimum at this concentration. All subsequent measurements were carried out by using 0.1 M concentrations of 2-TBA as constant and varying the D-glucose concentration from 500 μM to 1 μM.

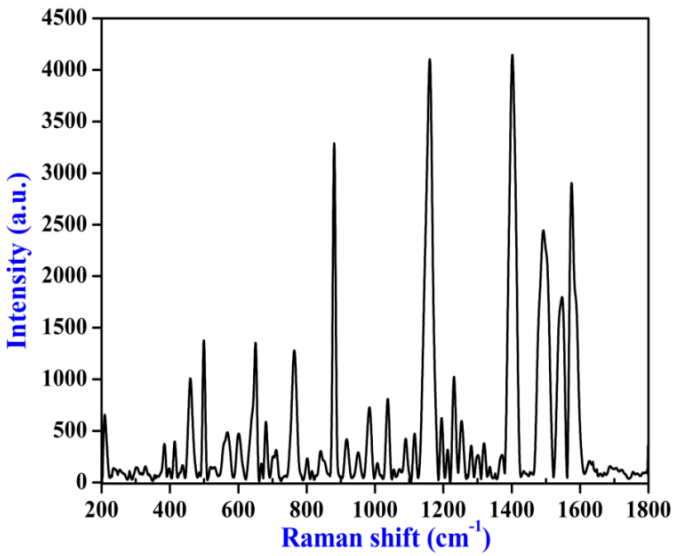


*Figure 5.3: SERS spectrum of 0.1M 2-TBA adsorbed on Ag nanocluster with laser excitation wavelength of 632.8 nm.*

The SERS spectrum of the 0.1 M base solution of 2-TBA is shown in figure 5.3. The intense Raman line at 880 $cm^{-1}$ is assigned to C-H out of-plane bending mode and 1160 $cm^{-1}$ line is assigned to C-H in-plane bending

mode. The Raman line at 209 $cm^{-1}$ is attributed to Ag-S bond [44] and this confirms that 2-TBA attaches to the Ag nanocluster surface through sulphur atom. Detailed Raman peak assignments are shown in table 5.1.

*Table 5.1 Peak assignments of SERS peaks of 2-TBA spectrum.*

| Assignment | SERS (Peak height) |
|---|---|
| Ag-S | 209 (655) |
| CBO in-plane bending | 383(372) |
| | 413(395) |
| | 459(1007) |
| B-O torsion | 499(1376) |
| | 568(485) |
| | 601(472) |
| | 650(1353) |
| | 681(588) |
| | 763(1279) |
| | 801(233) |
| | 841(304) |
| C-H out of-plane bending | 880(3287) |
| | 917(418) |
| B-O stretching | 950(290) |
| | 983(728) |
| | 1037(809) |
| | 1089(423) |
| | 1115(471) |
| C-H in-plane bending | 1160(4102) |
| | 1194(624) |
| | 1212(316) |
| | 1231(1023) |
| | 1253(595) |
| | 1281(355) |
| | 1301(264) |
| C-C stretching | 1319(378) |
| | 1371(266) |
| | 1401(4145) |

| | |
|---|---|
| | 1492(2443) |
| | 1547(1795) |
| | 1575(2901) |

Figure 5.4 shows the SERS spectrum of 0.1 M 2-TBA + 100 μM D-glucose solution which displays the characteristic Raman lines of glucose. This spectrum is an average of spectra from 10 different locations on the same SERS-active substrate. In addition to the Raman lines of 2TBA the Raman lines of D-glucose are also observed.

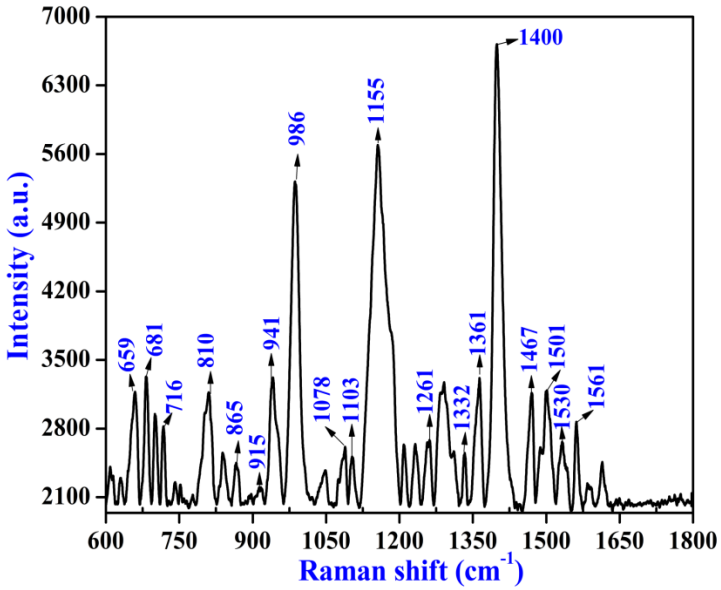


*Figure 5.4: SERS spectrum of 0.1 M 2-TBA + 100 μM D-glucose with laser excitation wavelength of 632.8 nm.*

The characteristic Raman lines of D-glucose seen at 1363 $cm^{-1}$ and 1078 $cm^{-1}$ are due to wagging mode of $CH_2$ and CO stretching mode, respectively. The peak at 1332 $cm^{-1}$ is due to $CH_2$ wagging mode. The peak assignments are shown in table 5.2.

*Table 5.2 Peak assignments of SERS peaks of (2-TBA+ D-glucose) spectrum.*

| Assignment | Normal Raman (Peak height) | SERS (Peak height) |
|---|---|---|
| | 233(89) | |
| (COC) bending mode | 363(62) | |
| | 396(170) | |
| (CCC) bending mode | 424(73) | |
| (CCC) bending mode | 440(117) | |
| | | 531 (898) |
| | 540(355) | 545(259) |
| | | 560 (326) |
| | | 629 (269) |
| Liberation ($H_2O$) | 653(59) | 659 (1145) |
| Due to 2TBA | | 681(1301) |
| | | 717(784) |
| | | 741(221) |
| | 773(91) | 752(195) |
| | | 810(1139) |
| (C-C) stretching mode | 842(249) | 838(523) |
| | | 866(420) |
| (C-H) bending mode | 915(118) | 917(265) |
| | | 941(221) |
| Due to 2TBA+D-glucose | | 986(3290) |
| (C-O) bending mode | 1022(74) | |
| | 1054(96) | 1048(345) |
| (C-O) stretching mode | 1075(205) | 1088(585) |
| | 1107(147) | 1103(482) |
| (COH) bending mode | 1121(137) | |
| | 1151(61) | 1155(3661) |
| Due to 2TBA | | 1208(606) |
| Due to 2TBA | | 1232(610) |
| ($CH_2$) twisting mode | 1272(78) | 1261(652) |
| | | 1291(1242) |
| ($CH_2$) wagging mode | 1330(92) | 1333(521) |

| | | |
|---|---|---|
| ($CH_2$) wagging mode | 1346(115) | 1363(1283) |
| Due to 2TBA | | 1399(4688) |
| $CH_2$ bending mode | 1459(81) | 1470(1131) |
| Due to 2TBA | | 1501(1159) |
| Due to 2TBA | | 1532(633) |
| Due to 2TBA | | 1561(836) |
| | | 1614(427) |

Interestingly there occurs a new intense peak at 986 $cm^{-1}$ which does not exist in the Raman spectrum of D-glucose although there is a much weaker line at about 983 $cm^{-1}$ in the Raman spectrum of 2-TBA which is due to the B-O stretching in 2-TBA. The second interesting feature of this new line is that it scales with the D-glucose concentration and we can use it to quantify the D-glucose concentration. We therefore carried out glucose concentration dependent studies and quantified the concentration using this characteristic line down to 1 micromole D-glucose concentration levels.

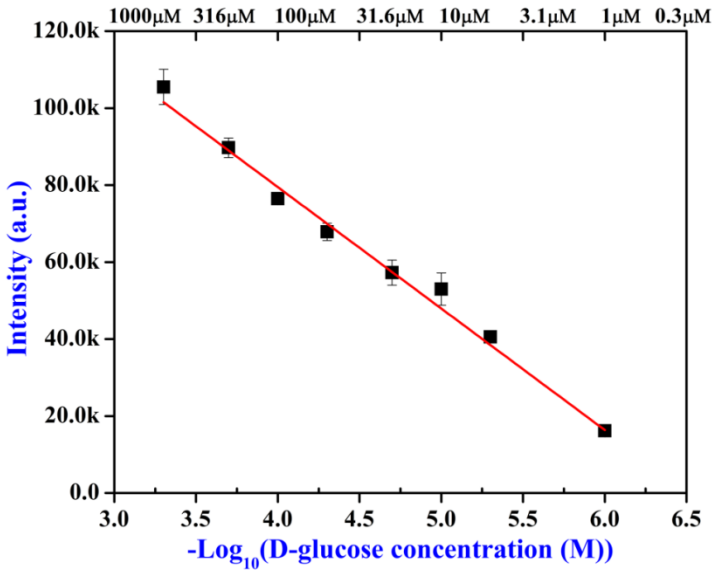


*Figure 5.5: Intensity variation of Raman line at 986 $cm^{-1}$ as a function of D-glucose concentration.*

We determined the area under the 986 $cm^{-1}$ peak by using a Lorentzian fit to the peak. The peak intensity as a function of D-glucose molar concentration is depicted in figure 5.5. A good correlation between the intensity of the peak and the D-glucose concentration is observed.

The measurements were repeated on newly prepared SERS substrates under the same preparation conditions. The results are depicted in figure 5.6 together with the earlier results. The second data set follows the similar trend as the first data set showing that the results are reproducible.

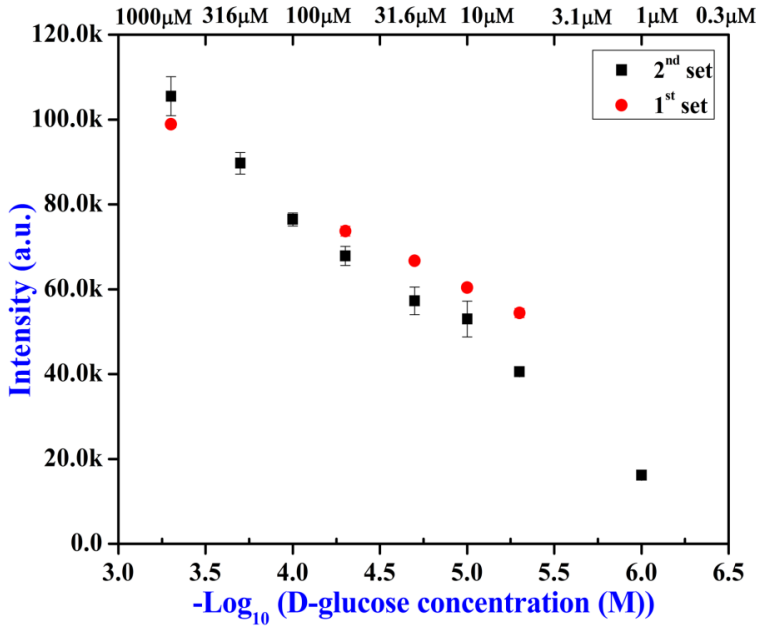


*Figure 5.6: Intensity variation of 986 $cm^{-1}$ Raman line with molar concentration of D-glucose done in two runs to test the reproducibility of results.*

## 5.4 Conclusion:

2-Thienylboronic acid was used as a linker molecule that attached to the silver surface on one side and to the D-glucose molecule on the other side. A strong Raman line was observed at 986 $cm^{-1}$ in the SERS spectrum.

The intensity of this line was used to quantify the D-glucose concentration in the molar concentration range of 1 to 500 micromoles. A good correlation was observed between the intensity of the Raman line and molar concentration of D-glucose. This result can be very significant in developing a sensor for non-invasive detection of D-glucose in diabetic patients using the urine or saliva samples. A patent application (3146/CHE/2015) has been filed for this work.

## References

[1] N.A. Calcutt, M.E. Cooper, T.S. Kern and A.M. Schmidt, "Therapies for hyperglycaemia-induced diabetic complications: from animal models to clinical trials" *Nat. Rev. Drug Discov. 8 (2009) 417.*

[2] IDF Diabetes Atlas Sixth Edition, International Diabetes Federation 2013.

[3] Y. Wang, H. Xu, J. Zhang and G. Li, "Electrochemical Sensors for Clinic Analysis" Sensors 8 (2008) 2043.

[4] M. Morikawa, N. Kimizuka, M. Yoshihara and T. Endo, "New Colorimetric Detection of Glucose by Means of Electron-Accepting Indicators: Ligand Substitution of $[Fe(acac)_{3-n}(phen)_n]^{n+}$ Complexes Triggered by Electron Transfer from Glucose Oxidase" *Chem. Eur. J. 8* (2002) 5580.

[5] S. Mansouri and J.S. Schultz, "A Miniature Optical Glucose Sensor Based on Affinity Binding" *Nature Biotech. 2 (*1984) 885.

[6] J.C. Pickup, F. Hussain, N.D. Evans, O.J. Rolinski and D.J.S. Birch, "Fluorescence-based glucose sensors" *Biosens. Bioelectron. 20 (2005)* 2555.

[7] M. Li, R. Li, M.C. Li and N. Q. Wu, "Electrochemical and optical biosensors based on nanomaterials and nanostructures: A Review" *Front. Biosci. 3 (2011) 1308.*

[8] V.K. Gupta, A. K. Singh, S. Mehtab and B. Gupta, "A Cobalt (II)-selective PVC membrane based on a Schiff base complex of N,N-bis(salicylidene)-3, 4-diaminotolune" *Anal. Chim. Acta 566 (2006) 5.*

[9] R.N. Goyal, V.K. Gupta and N. Bachheti, "Fullerene-$C_{60}$-modified electrode as a sensitive voltammetric sensor for detection of nandrolone-An anabolic steroid using in doping" *Anal. Chim. Acta 597 (2007) 82.*

[10] R.N. Goyal, V.K. Gupta and S. Chatterjee, "Fullerene-$C_{60}$-modified edge plane pyrolytic graphite electrode for the determination of dexamethasone in pharmaceutical formulations and human biological fluids" *Biosens. Bioelctron. 24 (2009) 1649.*

[11] M. Musameha, J. Wang, A. Merkocia and Y. Lin, "Low-potential stable NADH detection at carbon-nanotube-modified glassy carbon electrodes" *Electrochem. Commun. 4 (2002) 743.*

[12] Z. Wang, J. Liu, Q. Liang, Y. Wang and G. Luo, "Carbon nanotube-modified electrodes for the simultaneous determination of dopamine and ascorbic acid" *Analyst 127 (2002) 653.*

[13] R.N. Goyal, V.K. Gupta and S. Chatterjee, "A sensitive voltammetric sensor for determination of synthetic corticosteroid triamcinolone, abused for doping" *Biosens. Bioelctron. 24 (2009) 3562.*

[14] Y. Wang, Y. Li, L. Tang, J. Lu and J. Li, "Application of graphene-modified electrode for selective detection of dopamine" *Electrochem. Commun. 11 (2009) 889.*

[15] X. Kang, J. Wang, H. Wu, I.A. Aksay, J. Liu and Y. Lin, "Glucose Oxidase-graphene-chitosan modified for direct electrochemistry and glucose sensing" *Biosens. Bioelctron. 25 (2009) 901.*

[16] D.A.C. Brownson, C.W. Foster and C.E. Banks, "The electrochemical performance of graphene modified electrodes: An analytical perspective" *Analyst 137 (2012) 1815.*

[17] H. Ernst, B. Roß and M. Knoll, "Reliable glucose monitoring through the use of microsystem technology" *Anal. Bioanal. Chem. 373 (2002) 758.*

[18] X. Huang, S. Li, J. Schultz, Q. Wang and Q. Lin, "A Capacitive MEMES Viscometric Sensor for Affinity Detection fo Glucose" *J. Microelectromech. Syst. 18 (2009) 1246.*

[19] A. Heller, "Implanted Electrochemical Glucose Sensors for the Management of Diabetes" *Annu. Rev. Biomed. Eng. 1 (1999) 153.*

[20] J.C. Pickup 2003. Glucose sensors: Present and Future. International Textbook of Diabetes Mellitus.

[21] C.R. Taormina, J.T. Baca, S.A. Asher and J.J. Grabowski, "Analysis of tear glucose concentration with electrospray ionization mass spectrometry" *J. Am. Soc. Mass Spectrom. 18 (2007) 332.*

[22] J.C. Claussen, A. Kumar, D.B. Jaroch, M.H. Khawaja, A.B. Hibbard, D.M. Porterfield and T.S. Fisher, "Nanostructuring Platinum nanoparticles on Multilayered Graphene Petal Nanosheets for Electrochemical Biosensing" *Adv. Funt. Mater. 22 (2012) 3399.*

[23] Q. Yan, B. Peng, G. Su, B.E. Cohan, T.C. Major and M.E. Meyerhoff, "Measurement of Tear Glucose Levels with Amperometric Glucose Biosensor/Capillary Tube Configuration" *Anal. Chem. 83 (2011) 8341.*

[24] C. Jurysta, N. Bulur, B. Oguzhan, I. Satman, T.M. Yilmaz, W. J. Malaisee and A. Sener, "Salivary Glucose Concentration and Excretion in Normal and Diabetic Subjects" *J. Biomed. Biotechnol. Vol 2009, Article ID430426, 6 pages, 2009. doi:10.1155/2009/430426.*

[25] J.I. Peterson, "Urinary Glucose Measurement" *Clinical Chem. 15 (1968) 513.*

[26] Y. Wang, B. Yan and L. Chen, "SRS Tags: Novel optical Nanoprobes for Bioanalysis" *Chem. Rev. 113 (2013) 1391.*

[27] B. Sharma, R.R. Frontiera, A-L. Henry, E. Ringe and R.P. Van Duyne, "SERS: Materials, applications, and the future" *Mater. Today 15 (2012) 1.*

[28] J.P. Camden, J.A. Dieringer, J. Zhao and R.P. Van Duyne, "Controlled plasmonic nanostructures for surface-enhanced spectroscopy and sensing" *Acc. Res. 41 (2008) 1653.*

[29] J.A. Dieringer, A.D. McFarland, N.C. Shah, D.A. Stuart, A.V. Whitney, C.R. Yonzon, M.A. Young, X. Y. Zhang and R.P. Van Duyne, "Surface enhanced Raman spectroscopy: new materials, concepts, characterization tools, and applications" *Faraday Discuss. 132 (2006) 9.*

[30] C.L. Haynes, C. R. Yonzon, X. Y. Zhang and R.P. Van Duyne, "Surface-enhanced Raman sensors: early history and the development of sensors for quantitative biowarfare agent and glucose detection" *J. Raman Spectrosc. 36 (2005) 471.*

[31] O. Lyandres, R.P. Van Duyne, J.T. Walsh, M.R. Glucksberg and S. Mehrotra, "Prediction range estimation from noisy Raman spectra with robust optimization" *Analyst 135 (2010) 2111.*

[32] K. Ma, J.M. Yuen, N.C. Shah, J.T. Walsh, M.R. Glucksberg and R.P. Van Duyne, "In Vivo, Transcutaneous Glucose Sensing Using Surface-Enhanced Spatially Offset Raman Spectroscopy: Multiple Rats, Improved Hypoglycemic Accuracy, Low Incident Power, and Continuous Monitoring for Greater than 17 Days" *Anal. Chem. 83 (2011) 9146.*

[33] K.E. Shafer-Peltier, C. L. Haynes, M. R. Glucksberg and R. P. Van Duyne, "Toward a Glucose Biosensor on surface-enhanced Raman scattering" *J. Am. Chem. Soc. 125 (2003) 588.*

[34] D.A. Stuart, C.R. Yonzon, X.Y. Zhang, O. Lyandres, N.C. Shah, M.R. Glucksberg, J.T. Walsh and R.P. Van Duyne, "Glucose sensing using near-infrared surface-enhanced Raman spectroscopy: gold surfaces, 10-day stability, and improved accuracy" *Anal. Chem. 77 (2005) 4013.*

[35] D.A. Stuart, J.M. Yuen, N.S.O. Lyandres C.R. Yonzon, M.R. Glucksberg, J.T. Walsh and R.P. Van Duyne, "In Vivo Glucose Measurement by Surface-Enhanced Raman Spectroscopy" *Anal. Chem. 78 (2006) 7211.*

[36] K. Vangala, M. Yanney, C.T. Hsiao, W.W. Wu, R.F. Shen, S.G. Zou, A. Sygula and D.M. Zhang, "Sensitive Carbohydrate Detection using Surface Enhanced Raman Tagging" *Anal. Chem. 82 (2010) 10164.*

[37] C.R. Yonzon, C.L. Haynes, X.Y. Zhang, J.T. Walsh and R.P. Van Duyne, "A Glucose Biosensor Based on Surface-Enhanced Raman Scattering: Improved Partition Layer, Temporal Stability, Reversibility, and Resistance to Serum Protein Interference" *Annal. Chem 76 (2004) 78.*

[38] C.R .Yonzon, O. Lyandres, N.C. Shah, J.A. Dieringer and R.P. Van Duyne, 2006. Glucose Sensing with Surface-Enhanced Raman Spectroscopy. Springer, New York.

[39] J.M. Yuen, N.C. Shah, J.T. Walsh, M.R. Glucksberg and R.P. Van Duyne, "Transcutaneous Glucose Sensing by Surface-Enhanced Spatially Offset Raman Spectroscopy in a Rat Model" *Annal. Chem. 82 (2010) 8382.*

[40] X. Zhang, N.C. Shah and R.P. Van Duyne, "Sensitive and selective chem/bio sensing based on surface-enhanced Raman spectroscopy (SERS)" *Vib. Spectrosc. 42 (2006) 2.*

[41] O. Lyandres, N. C. Shah, C. R. Yonzon, J. T. Walsh Jr., M. R. Glucksberg and R. P. Van Duyne, "Real-Time Glucose Sensing by Surface-Enhanced Raman Spectroscopy in Bovine Plasma Facilitated by a Mixed Decanethiol/Mercaptohexanol Partition Layer" *Anal. Chem. 77 (2005) 6134.*

[42] U.S. Dinish, F.C. Yaw, A. Agarwal and M. Olivo, "Development of highly reproducible nanogap SERS substrates: Comparative performance analysis and its application for glucose sensing" *Biosens. Bioelectron. 26 (2011) 1987.*

[43] K.V. Kong, C.J.H. Ho, T. Gong, W.K.O. Lau and M. Olivo, "Sensitive SERS glucose sensing in biological media using alkyne functionalized boronic acid on planar studies" *Biosens. Bioelectron. 56 (2014) 186.*

[44] L. ŠKantárová, A. Oriňák, R. Oriňáková and F. Lofaj, "4-Aminothiophenol Strong SERS Signal Enhancement at Electrodeposited Silver Surface" *Nano-Micro Lett. 4 (2012) 184.*

# Chapter 6

# SERS studies on L-Amino Acids

*Amino acids are the basic structural units of proteins and enzymes. In order to understand the protein SERS spectra, it is necessary to have a fundamental understanding of the individual amino acid SERS spectra. In this chapter, we describe the SERS measurements of 19 L-amino acids and suggest a method for quantitative analysis. A linear correlation was found between intensities of the characteristic Raman lines and molar concentrations of the amino acids. These results would have promising applications in detection of these amino acids in more complex molecules. The results of this study are published in Chemical Physics Letters*[1].

[1]*Raju Botta, A. Rajanikanth, C. Bansal, Chem. Phys. Lett. 618 (2015) 14.*

## 6.1 Introduction:

Amino acids are basic building blocks of proteins and enzymes. They are composed of the amine (-$NH_2$) and the carboxylic group (COOH) functional groups with a side chain R specific to each amino acid. The basic structure of an amino acid is $NH_2$-CH(R)-COOH. There are more than 500 known amino acids and can be classified into many categories. The classification is on the basis of the core structural functional group location viz. alpha (α), beta (β), and gamma (γ) or delta (δ). In addition to this, there are further classifications related to pH level, polarity and side-chain group type viz. aromatic, aliphatic, acidic, basic, amidic, hydroxylic and sulphur containing amino acids. 23 proteinogenic (protein building) amino acids combine into peptide chains to form proteins. These are all L-stereoisomers but some D-isomers are found in bacterial envelopes and some antibiotics. 20 of the 23 proteinogenic amino acids are directly encoded by triplet codons in the genetic code and are known as the standard amino acids. The other three are non-standard or non-canonical amino acids, which are selenocysteine, pyrrolysine and N-formylmethionine.

The 20 standard amino acids are classified according to the different side-chains or functional groups in them: Aliphatic amino acids [L-Alanine (L-Ala), L-Glycine (L-Gly), L-Isoleucine (L-ILe), L-Leucine (L-Leu), L-Proline (L-Pro) and L-Valine (L-Val)], Aromatic amino acids [L-Phenylalanine (L-Phe), L-Tryptophan (L-Trp) and L-Tyrosine (L-Tyr)], Acidic amino acids [L-Aspartic acid (L-Asp), L-Glutamic acid (L-Glu)], Basic amino acids [L-Arginine (L-Arg), L-Histidine (L-His), and L-Lysine (Lys)], Hydroxylic [L-Serine (L-Ser) and L-Threonine (L-Thr)], Sulphur containing amino acids [L-Cysteine (L-Cys) and L-Methionine (L-Met)] and Amidic amino acids

[L-Asparagine (L-Asn) and L-Glutamine (L-Gln)]. These are further classified as essential (human body cannot produce these amino acids by itself), semi-essential (in some cases these are essential) and non-essential (human body can produce within itself) amino acids. The classification of amino acids is shown in the flow chart below (figure 6.1).

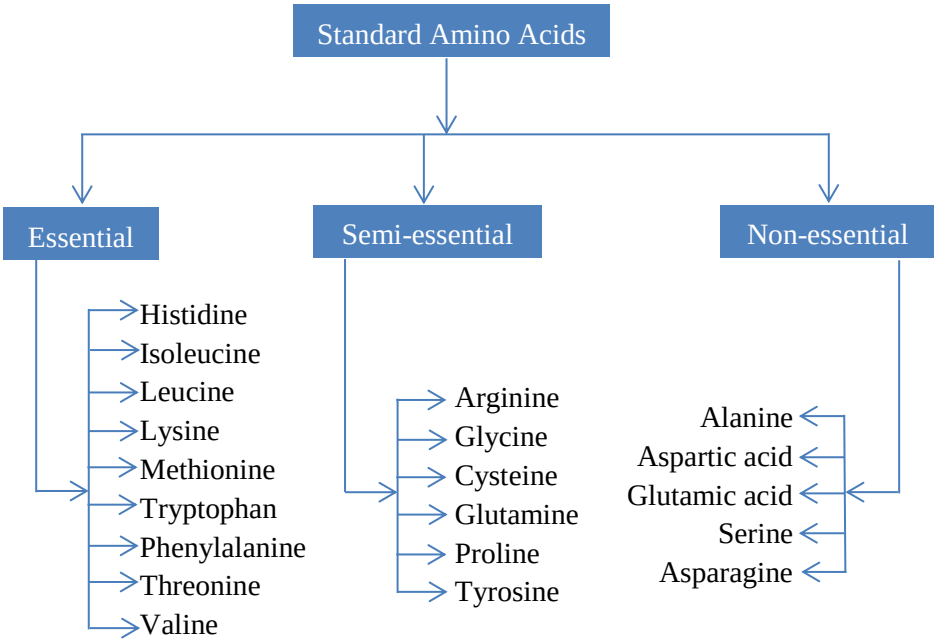


*Figure 6.1: Flow chart of L-amino acids classification.*

Various methods are there for the analysis of amino acids viz. high-performance liquid chromatography (HPLC), paper and thin layer chromatography, gas chromatography (GC) and mass spectrometry (MS). These are effective techniques, however, they require a time consuming pretreatment process [1]. Therefore, there is a need to develop rapid method to monitor amino acids. Raman spectroscopy is one method to analyze amino acids rapidly without pretreatment process. Some reports on amino

acids are documented in the literature [2-9] through Raman and SERS methods.

First report of SERS on amino acids adsorbed on metal surfaces was by Nabiev et al. in 1981 [10]. Most of the studies reported in the literature are on the adsorption behavior of amino acids on metal (Ag, Au) surface with the pH of the solution and some are on the homo and dipeptides [3, 4]. In this chapter, we discuss the quantitative measurements of 19 L-Amino acids adsorbed on silver nanocluster substrates.

Wide ranges of aqueous solutions (millimole – micromole) of amino acids were prepared by sequential dilution method. 40 μL aqueous solutions of amino acids were dropped on 1x1 $cm^2$ Ag nanocluster surfaces and allowed to dry. Raman measurements were carried out on these substrates at a laser excitation wavelength of 514.5 nm. A detailed discussion on the normal Raman and SERS spectra of L-amino acids is given in the following sections.

### 6.2 Aromatic Amino Acids:

There are three aromatic amino acids, namely L-Phenylalanine (L-Phe), L-Tryptophan (L-Trp) and L-Tyrosine (L-Tyr). The chemical structures of these amino acids are illustrated in figure 6.2.

L-Phe is an essential amino acid. L-Phe is found naturally in breast milk of mammals. It is sold as a nutritional supplement and it is a direct precursor to the neuromodulator phenylmethylamine. Phenylketonuria (PKU) is a genetic disorder; it is caused due to the inability to metabolize phenylalanine. People suffering from PKU are known as phenylketonurics.

Phenylketonurics must regulate intake of protein to control the buildup of Phe as their bodies convert protein into its component amino acids. Phe can be diagnosed through blood tests and usually reported in units of mg/dL and μg/dL. In addition to food source there is non-food source of Phe called artificial sweetener Aspartame. Aspartame metabolized by the body converts into several chemical byproducts including Phe.

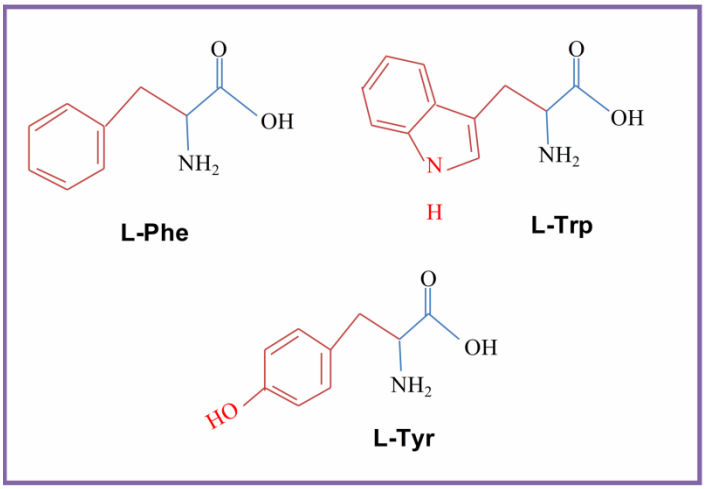


*Figure 6.2: L-Phe, L-Trp and L-Tyr chemical structures.*

L-Phe has a phenol ring in its side chain. A preliminary work was reported on Raman and SERS studies of L-Phe [3, 11-13]. Normal Raman (NR) spectrum of L-Phe as-received powder form is shown in figure 6.3. The weak Raman line at 619 $cm^{-1}$ is assigned to the ring deformation mode of mono substituted benzene ring. The intense Raman line at 1000 $cm^{-1}$ and slightly weaker one at 1031 $cm^{-1}$ are due to mono substituted benzene ring or ring breathing mode.

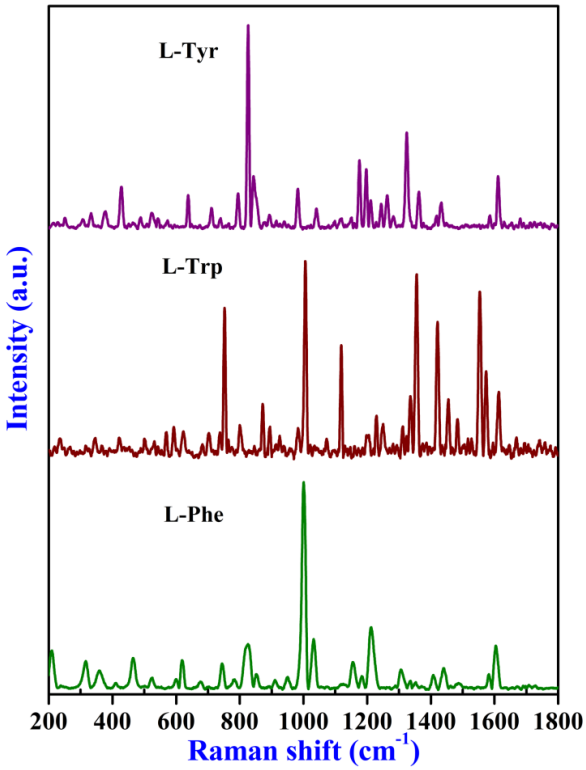


*Figure 6.3: Raman spectra of L-Phe, L-Trp and L-Tyr in the as-received powder form.*

L-Trp is an essential amino acid in the human diet. It is important in the medical field as an anti-depressant and a narcotic. The L-Trp has indole ring containing pyrrole ring in its side chain which makes the difference in structure and Raman modes compared to the other amino acids. NR spectrum of as-received powder form is shown in figure 6.3. The Raman lines which are present in the spectrum are in good agreement with the reported ones [14 - 16]. The Raman lines at 594 $cm^{-1}$, 874 $cm^{-1}$, 1007 $cm^{-1}$ and 1117 $cm^{-1}$ are relevant to indole bonds. These lines are assigned as the deformation mode of NH, coupled deformation vibration involving benzene and pyrrole moieties CH and benzene ring and pyrrole ring skeletal deformation, respectively. The strong line at 755 $cm^{-1}$ is due to pyrrole ring.

Peaks at 1336 $cm^{-1}$ and 1356 $cm^{-1}$ are known as Tryptophan doublet. Weak bonds at 1229 $cm^{-1}$ and 1202 $cm^{-1}$ are due to the CH bending vibration of the indole fragment. Intense bonds at 1355 $cm^{-1}$ and 1421 $cm^{-1}$ are attributed to $COO^-$ stretching modes and the Raman line at 1553 $cm^{-1}$ is C-C stretching mode. The weak line at 1312 $cm^{-1}$ is the aliphatic $CH_2$ deformation mode.

L-Tyr is a semi-essential amino acid. It plays an import role in the body in addition to protein formation. It functions as a receiver of phosphate groups. Preliminary work has been carried on Raman and SERS studies of L-Tyr in the literature [17-19]. NR spectrum of L-Tyr in as-received powder form is also shown in figure 6.3. The intense and slightly intense Raman lines are observed at 826 $cm^{-1}$ and 843 $cm^{-1}$, respectively. These lines are assigned to Tyrosine doublet.

SERS spectra of $10^{-6}$ M concentration of L-Phe, L-Trp and L-Tyr are shown in figure 6.4. The peaks of L-Phe which are present in the spectrum are in good agreement with the earlier reports [3, 11-13]. The SERS peak positions are close to but do not exactly match with the Raman lines of the as-received amino acid. This may be due to a small change in the frequency of the Raman active modes when the molecule is attached to the metal surface. The intense SERS line of phenol ring breathing mode appearing in the SERS spectrum at 1000 $cm^{-1}$ is in very good agreement with the as-received sample. The line in the SERS spectrum at 930 $cm^{-1}$ is noted as a typical ring vibration which was not observed in the as-received sample. The lines at 1390 $cm^{-1}$ due to $COO^-$ symmetric stretching vibration and 1440 $cm^{-1}$ due to $CH_2$ scissoring mode compare well with the lines observed for the as-received sample. The $COO^-$ symmetric stretching mode is presented in all the 19 L-amino acids in the range 1384 $cm^{-1}$ - 1410 $cm^{-1}$. When we compare

normal Raman and SERS spectra an additional line has appeared in SERS at 242 $cm^{-1}$. This line was assigned to Ag-N band [20] and it is appearing in all the 19 amino acids in the range 230 $cm^{-1}$ to 242 $cm^{-1}$. The peak assignments of L-Phe are given in the table T1 (Appendix).

The Raman lines of L-Trp at 1560 $cm^{-1}$ and the 1618 $cm^{-1}$ are due to the deformations of C-C stretching and Indole N-H vibration, respectively. The common carboxylate line is also seen in the SERS spectrum of L-Trp. A comparison of the Raman shifts of normal Raman and the SERS spectra is shown in table T2 (Appendix) in which peak assignments are also given.

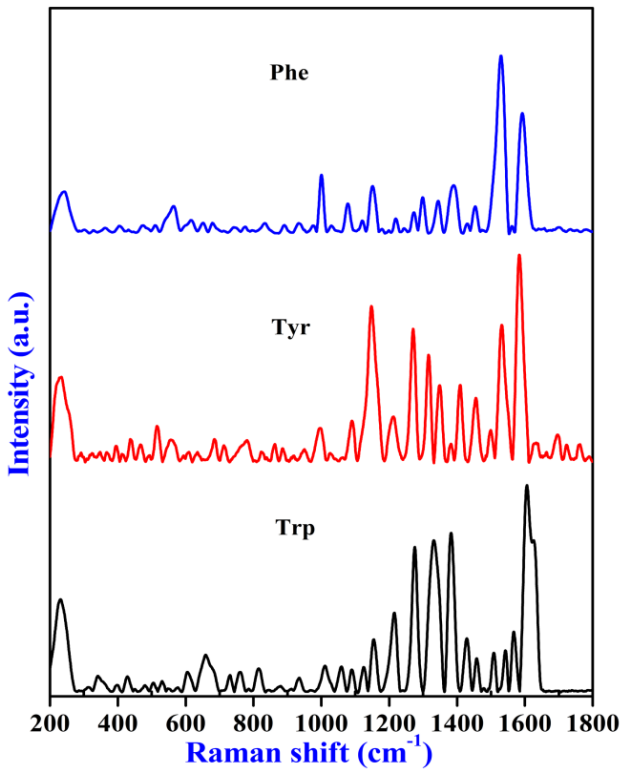


*Figure 6.4: SERS spectra of $10^{-6}$ M L-Phe, L-Trp and L-Tyr adsorbed on Ag nanocluster substrate with laser excitation wavelength of 514.5 nm.*

The peaks at 1327 $cm^{-1}$ and the 1365 $cm^{-1}$ in NR spectrum of L-Tyr are due to ring vibration and ring stretching, respectively. The Raman line at 1205 $cm^{-1}$ in SERS spectrum is due to phenol C stretching. A comparison of the Raman shifts of normal Raman and the SERS spectra is shown in table T3 (Appendix)

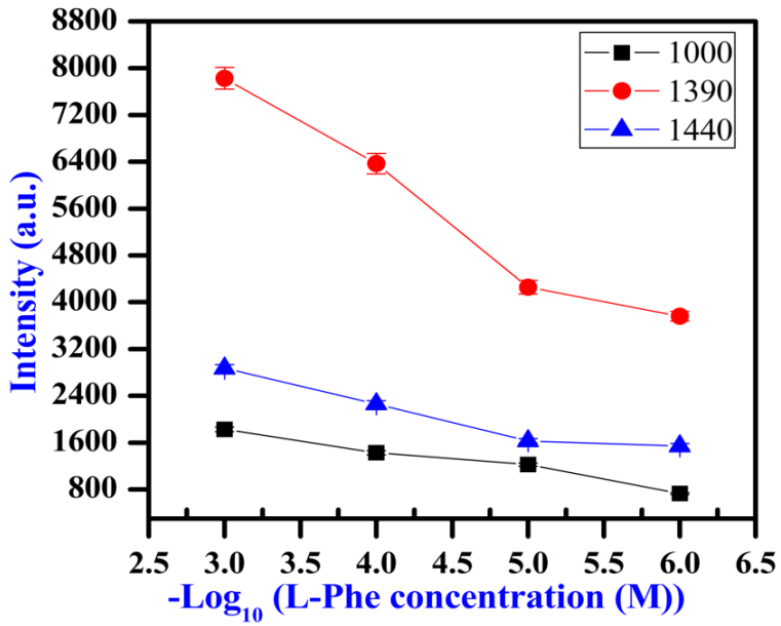


*Figure 6.5: Raman lines intensity variation with molar concentration of L-Phe.*

To be able to use the intensity of the Raman lines for quantitative measurements it is essential to identify the characteristic lines specific to the amino acid. The intensity of the Raman line at 1390 $cm^{-1}$ from the carboxylic group ($COO^-$ symmetric stretching mode) shows a variation with concentration for all the amino acids. Besides this common line, the intense Raman line at 1000 $cm^{-1}$ (ring breathing mode) and the 1440 $cm^{-1}$ peak ($CH_2$ scissoring mode) of L-Phe were identified for quantitative measurements. The intensities of these Raman lines were obtained by carrying out a

Lorentzian fit to the peaks and finding the area under the peaks. These intensities are plotted as a function of molar concentration as shown in figure 6.5.

In addition to the common carboxylate line (L-Trp at 1388 $cm^{-1}$, 1410 $cm^{-1}$ for L-Tyr), the Raman lines of L-Trp at 1556 $cm^{-1}$ (C-C stretching) and 1620 $cm^{-1}$ (indole N-H vibration), and the L-Tyr Raman at 1205 $cm^{-1}$ (Phenyl C stretching mode) were identified for quantitative measurements. The intensities are plotted as a function of molar concentration and shown in figures F1- F2 (Appendix).

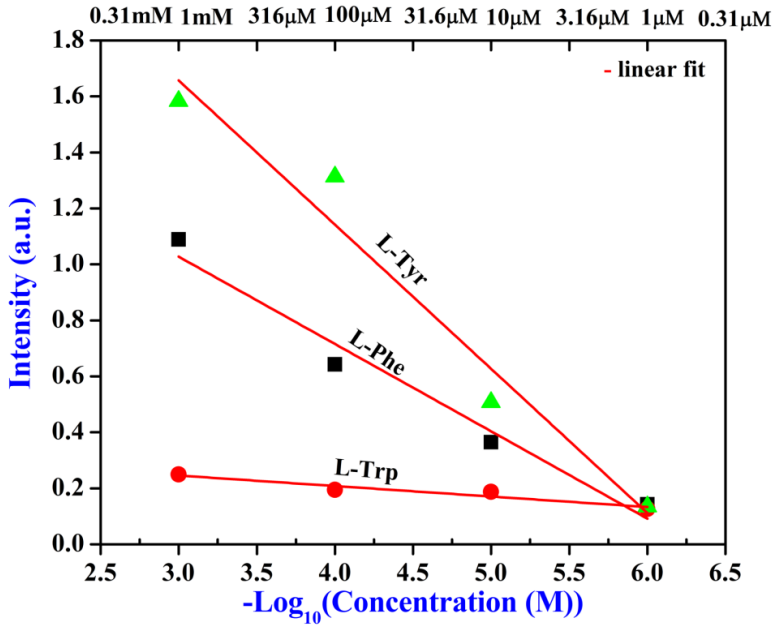


*Figure 6.6: Integrated intensities (sum of intensities of Raman lines normalized to the line intensity of Ag-N) as a function of molar concentrations of L-Trp, L-Phe and L-Tyr.*

The correlation between intensity and molar concentration becomes more apparent if we sum the reference lines intensities and normalize it by dividing the intensity of Ag-N band Raman line (~ 230 $cm^{-1}$). This eliminates

experimental artifact if any due to the areal distribution of nanoclusters between different substrates. The normalized intensities are plotted as a function of molar concentration as shown in figure 6.6. This result shows a good correlation between the two quantities thus providing confidence in our approach for quantifying the data. The same normalization procedure has therefore been followed in the subsequent sections.

### 6.3 Basic Amino Acids:

There are three amino acids in this group, namely L-Histidine (L-His), L-Lysine (L-Lys) and L-Arginine (L-Arg). The chemical structures of the Basic amino acids are shown in the figure 6.7.

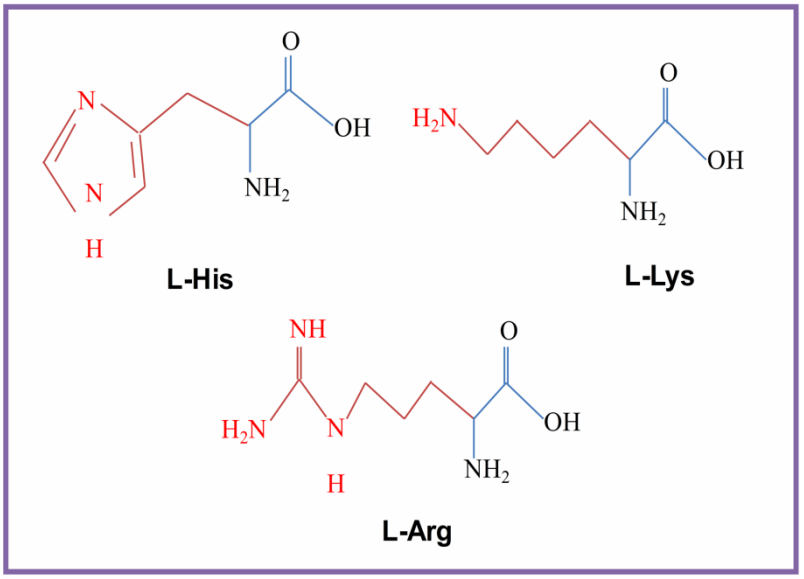


*Figure 6.7: Chemical structures of L-His, L-Lys and L-Arg.*

L-His is an essential amino acid. It has imidazole ring in its side chain. It has been studied extensively and intensively due to its biochemical significance. L-His is involved in various biological processes including

enzymes actions and medical applications [21]. L-Lysine (L-Lys) is an essential amino acid. The amino acid L-Arg is semi-essential or conditionally essential amino acid in mammals. In preterm infants, it is critical because infants are unable to synthesize it. It plays an important role in body like, cell division, healing wounds, immune function, removing ammonia from the body and release of hormones. Raman, IR and SERS studies on L-Arg have been reported in the literature [22, 23].

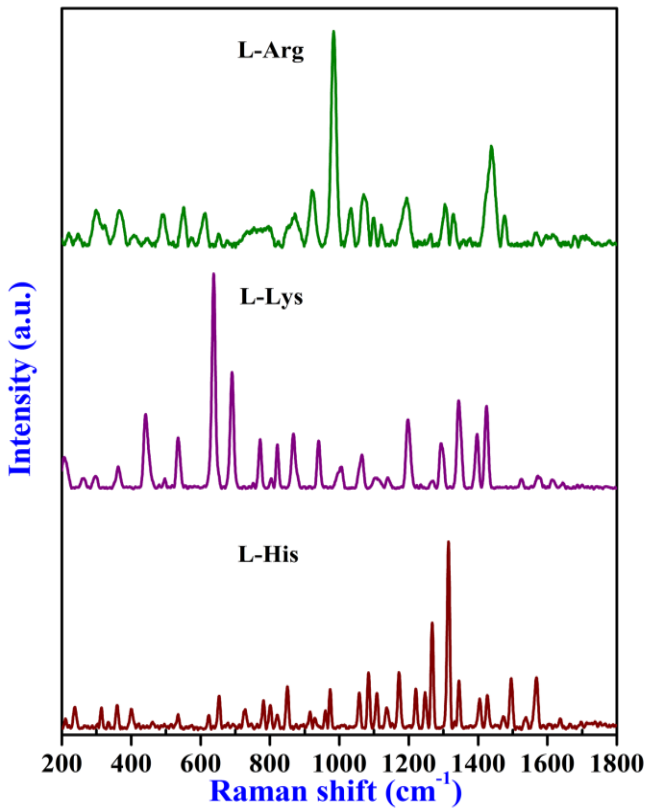


*Figure 6.8: Raman spectra of L-His, L-Lys and L-Arg in the as-received powder form.*

NR spectra of as-received powder forms of L-His, L-Lys and L-Arg are shown in figure 6.8. The Raman lines of L-His are in good agreement with reported ones [19, 20, 24]. L-Arg is associated with guanidinium fragment

(GF) in the side chain which makes it structurally different from other amino acids. The Raman line at 1437 $cm^{-1}$ is assigned to NH deformation in GF.

SERS spectra of $10^{-6}$ M concentration of L-His, L-Lys and L-Arg adsorbed on substrates are shown in figure 6.9. The L-His NR line at 1568 $cm^{-1}$ which is due to C=C stretching + N-H bending is enhanced in the SERS spectrum and moves to 1580 $cm^{-1}$. The L-Arg and L-Lys results are in good agreement with the reported literature [3, 25]. The peak assignments are given in tables T4-T6 (Appendix).

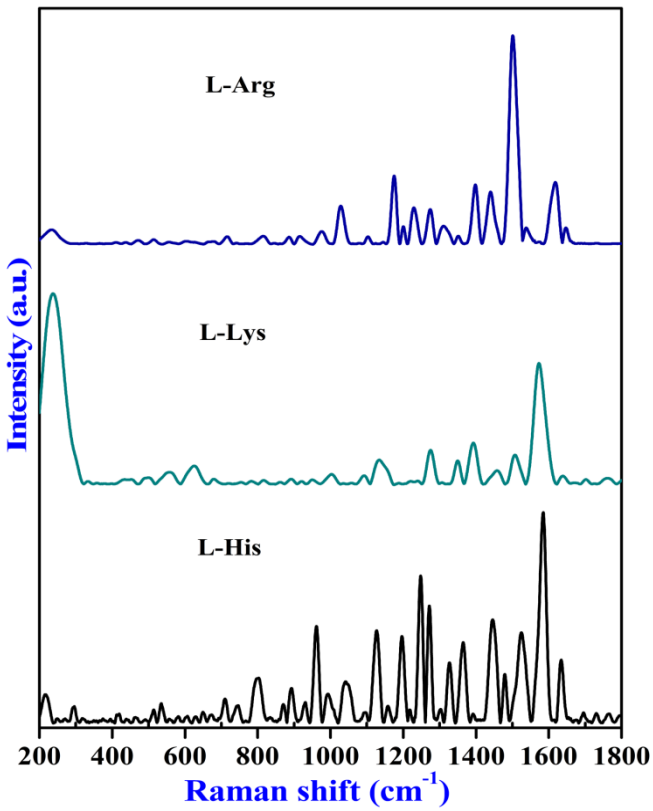


*Figure 6.9: SERS spectrum of $10^{-6}$M L-His, L-Lys and L-Arg adsorbed on Ag nanocluster substrate with laser excitation wavelength of 514.5 nm.*

In addition to the common carboxylic line (at 1390 $cm^{-1}$ (L-His) and 1400 $cm^{-1}$ (L-Lys and L-Arg)), the Raman lines at 800 $cm^{-1}$ (imidazole ring breathing mode) for L-His, 1440 $cm^{-1}$ ($CH_2$ scissoring+ NH deformation) and 1080 $cm^{-1}$ (C-N stretching) for L-Lys and the lines of L-Arg at 1444 $cm^{-1}$ (NH deformation in GF) and 1340 $cm^{-1}$ (CH deformation mode) were identified for quantitative measurements. The intensity variations with molar concentrations are shown in figures F3-F5 in the appendix. The normalized intensity as a function of molar concentrations of L-His, L-Arg and L-Lys are depicted in figure 6.10.

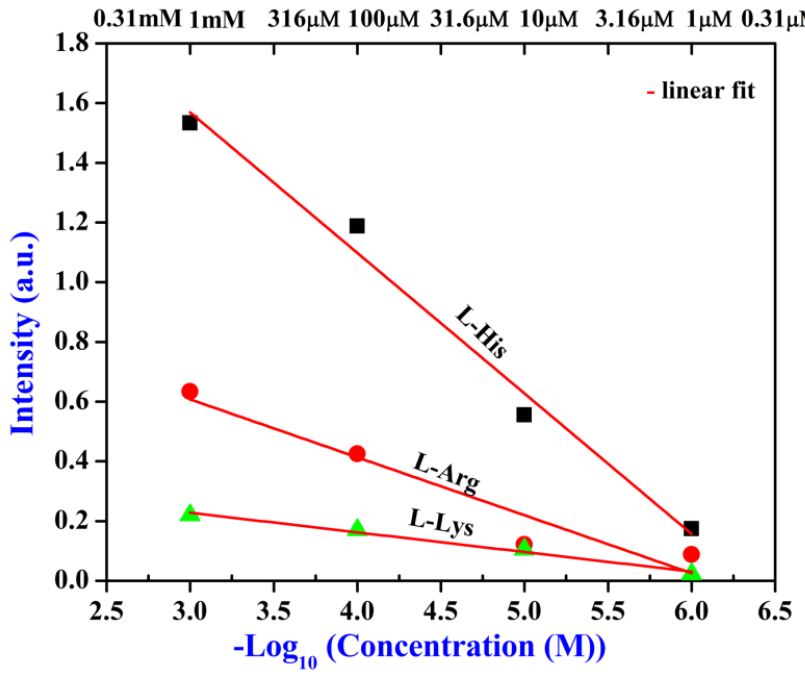


*Figure 6.10: Integrated intensities (sum of intensities of Raman lines normalized to intensity of Ag-N) as a function of molar concentration of L-His, L-Arg and L-Lys.*

## 6.4 Amidic Amino Acids:

The amidic group contains $CONH_2$ functional group in the side chain. There are two amino acids in this group viz. L-Asparagine (L-Asn) and L-Glutamine (L-Gln). The chemical structures of the amidic amino acids are depicted in figure 6.11.

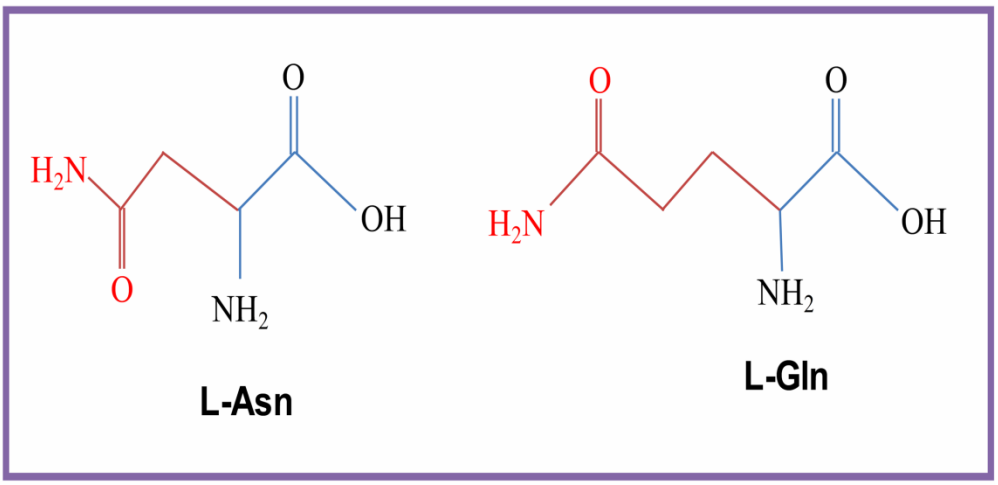


*Figure 6.11: L-Asn and L-Gln chemical structures.*

L-Asn is a non-essential amino acid. It requires for the development and function of brain. L-Gln is a conditionally essential or semi essential amino acid. The difference between L-Gln and L-Asn is the number of methyl groups. L-Gln has one extra methyl group compared to L-Asn. NR spectra of L-Asn and L-Gln in the as received powder form is shown in figure 6.12.

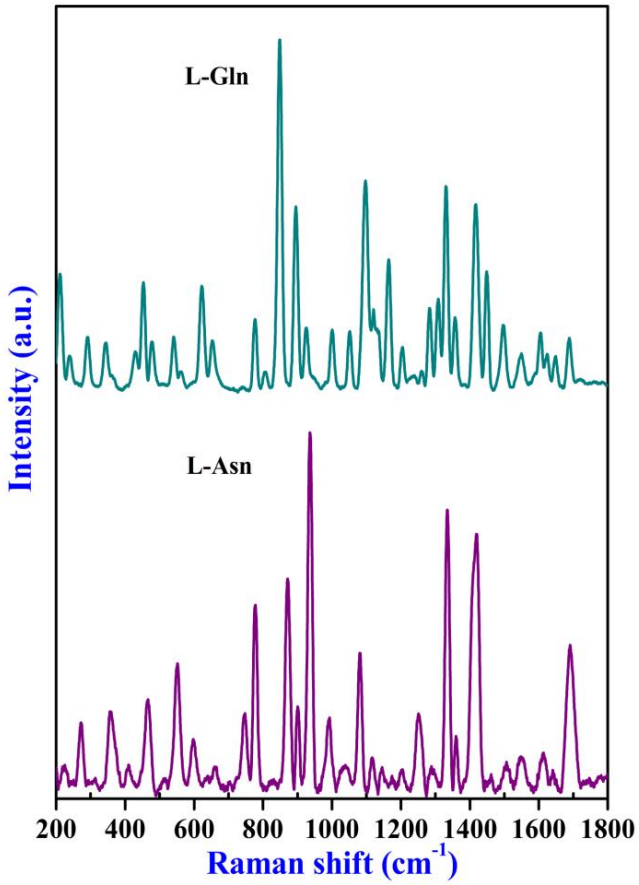


*Figure 6.12: Raman spectra of L-Asn and L-Gln in the as-received powder form.*

SERS spectra of $10^{-6}$ M L-Asn and L-Gln adsorbed on substrates are depicted in figure 6.13. The SERS spectra of L-Asn snd L-Gln are in good agreement with reported ones [26, 1]. The Raman lines of L-Asn at 540 $cm^{-1}$ in NR spectrum and the 554 $cm^{-1}$ peak in SERS spectrum are due to O=C-N skeletal deformation. The L-Gln Raman lines at 540 $cm^{-1}$ in NR and 544 $cm^{-1}$ in SERS spectra are due to O=C-N skeletal deformation. A comparison of the Raman shifts of NR and the SERS spectra are given in tables T7-T8 (Appendix). Peak assignments are also listed in these tables.

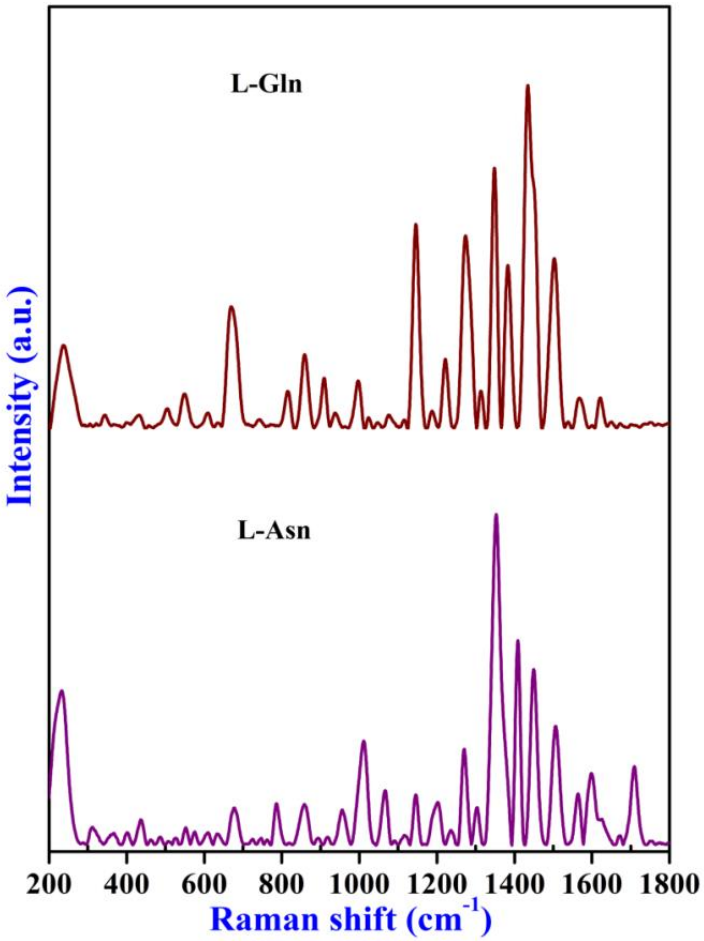


*Figure 6.13: SERS spectra of $10^{-6}$M L-Asn and L-Gln adsorbed on Ag nanocluster substrate with laser excitation wavelength of 514.5 nm.*

In addition to carboxylate mode (1400 $cm^{-1}$), the peak at 1256 $cm^{-1}$ ($CH_2$ wagging) of L-Asn and the peak at 1134 $cm^{-1}$ ($NH_3^+$ deformation) of L-Gln were taken as reference lines for quantitative measurements. The intensities as a function of molar concentrations are shown in the figures F6-F7 (Appendix). The integrated normalized intensity variations with molar concentrations of L-Asn and L-Gln are shown in figure 6.14.

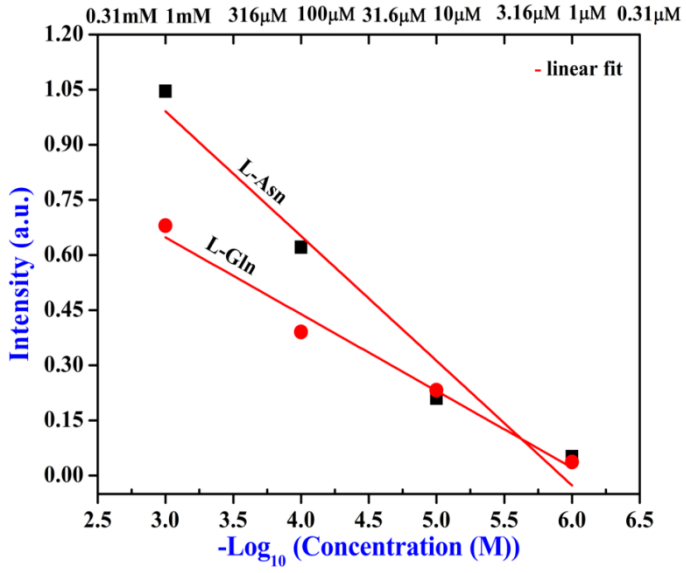


*Figure 6.14: Integrated intensities (sum of intensities of Raman lines normalized to intensity line of Ag-N) as a function of molar concentration of L-Asn and L-Gln.*

## 6.5 Acidic Amino Acids:

There are two amino acids in this category, namely L-Aspartic acid (L-Asp) and L-Glutamic acid (L-Glu). The chemical structures of these amino acids are shown in figure 6.15.

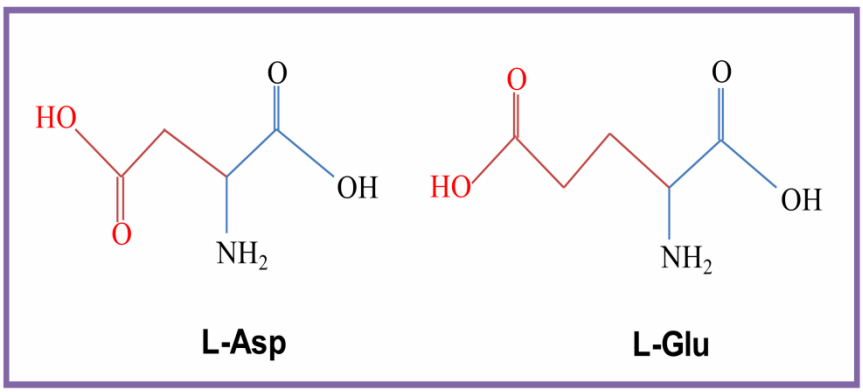


*Figure 6.15: Chemical structures of L-Asp and L-Glu.*

L-Asp is non-essential amino acid. Body can produce this by other amino acids. L-Glu is non-essential amino acid. These two amino acids have two carboxylate groups; one is in the back bone and second is in the side chain. NR spectra of L-Asp and L-Glu in the as-received powder form are shown in figure 6.16. The most intense Raman line of L-Asp at 936 $cm^{-1}$ is due to C-$COO^-$ stretching and a Raman line at 1690 $cm^{-1}$ is due to $NH_2$ shear vibration. The peaks at 777 $cm^{-1}$ and 871 $cm^{-1}$ are due to out of plane $OCO^-$ vibration and CC stretching, respectively. For L-Glu, the intense Raman line observed at 863 $cm^{-1}$ is ascribed to COOH vibration. The Raman line at 917 $cm^{-1}$ is due to C-C-N stretching mode.

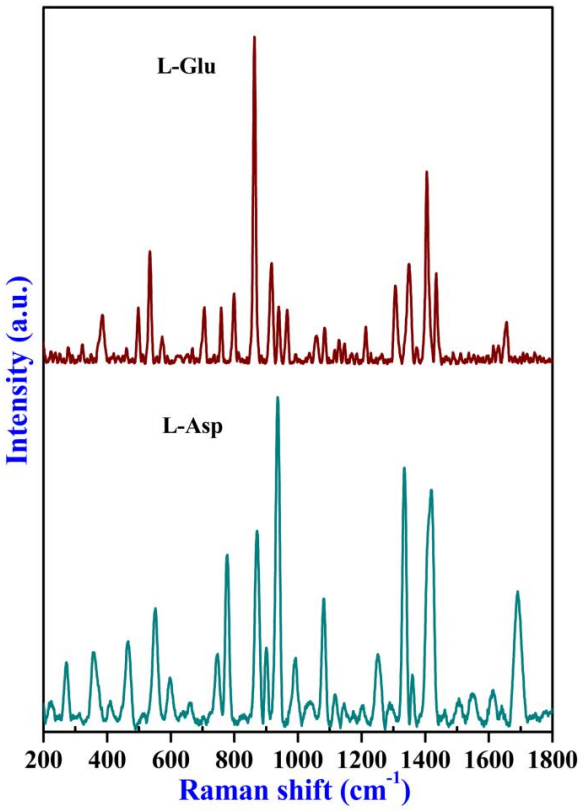


*Figure 6.16: Raman spectra of L-Asp and L-Glu in the as-received powder form.*

SERS spectrum of $10^{-6}$ M L-Asp and L-Glu adsorbed on substrates are shown in figure 6.17. The SERS spectra of L-Asp and L-Glu are in good agreement with the reported ones [27, 3]. L-Asp has COOH group in the side chain. The intense Raman lines due to the $COO^-$ were showing up at 936 $cm^{-1}$, 1334 $cm^{-1}$ and 1419 $cm^{-1}$ in NR spectrum and at 930 $cm^{-1}$, 1324 $cm^{-1}$ and 1400 $cm^{-1}$ in SERS spectrum. For L-Glu, the peak at 1405 $cm^{-1}$ in NR spectrum and 1400 $cm^{-1}$ in SERS spectrum are due to $COO^-$ symmetric stretching vibration. A comparison of the Raman shifts of NR and the SERS spectra and the peak assignments are shown in tables T9-T10 (Appendix) in the appendix.

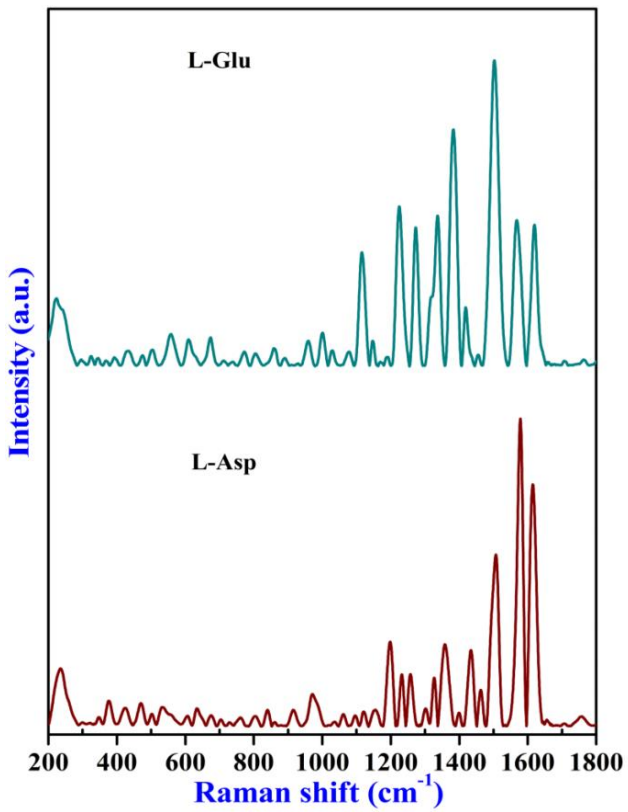


*Figure 6.17: SERS spectra of $10^{-6}$M L-Asp and L-Glu adsorbed on Ag nanocluster substrate with laser excitation wavelength of 514.5 nm.*

In addition to the common carboxylate line, the Raman line of L-Asp at 930 $cm^{-1}$ due to C-$COO^-$ stretching and the L-Glu Raman line at 1275 $cm^{-1}$ (OH bending + CO stretching) were taken for quantitative measurements. The intensities of Raman lines as a function of molar concentrations are shown in figures F8-F9 (appendix). The normalized intensities along with molar concentrations of L-Asp and L-Glu are depicted in figure 6.18.

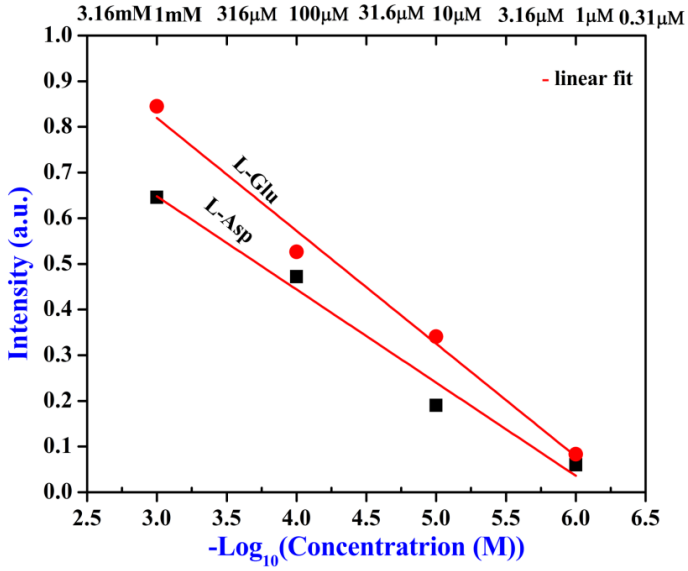


*Figure 6.18: Integrated intensities (sum of intensities of Raman lines normalized to intensity line of Ag-N) as a function of molar concentration of L-Asp and L-Glu.*

## 6.6 Aliphatic Amino Acids:

There are six amino acids in this group viz. L-Glycine (L-Gly), L-Alanine (L-Ala), L-Valine (L-Val), L-Proline (L-Pro), L-Leucine (L-Leu) and L-Isoleucine (L-Ile). The chemical structures of these aliphatic amino acids are illustrated in the figure 6.19.

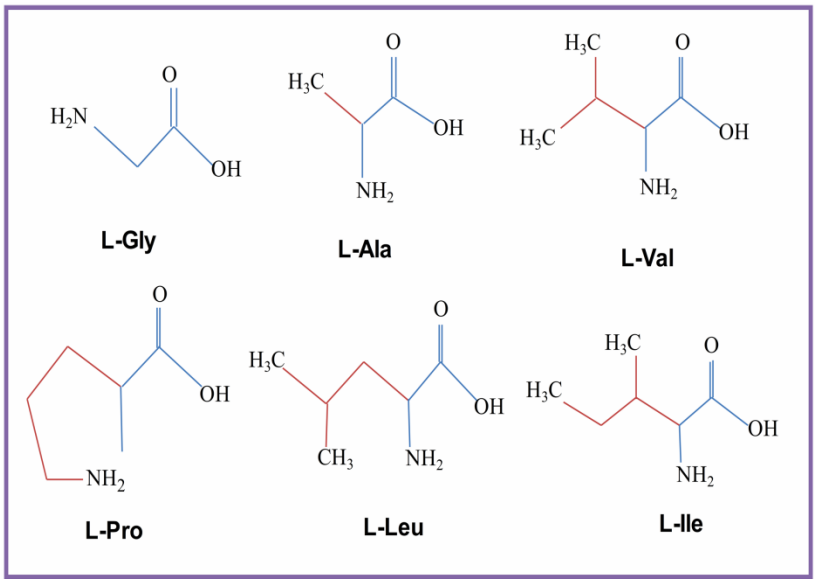


*Figure 6.19: Chemical structures of L-Gly, L-Ala, L-Val, L-Pro, L-Leu and L-Ile.*

L-Gly is a semi essential amino acid. It is the simplest molecule among the 20 L-amino acids. The Glycine is a precursor to the proteins and plays a role in the formation of collagen helix with hydroxyproline. L-Ala is a non-essential amino acid. Alanine plays a vital role in glucose alanine cycles between tissues and liver. High levels of Alanine link to high blood pressure. If Alanine cycle is modified that increases the levels of aminotransferase (ALT) which is linked to type II diabetes. ALT is found in plasma and other body tissues, but mostly in the liver. L-Ala has a similar structure to L-Gly except hydrogen in methylene group is replaced by a methyl group. The slightest change in the geometry may alter the intensities of the vibrational modes. L-Val is an essential amino acid. L-Pro is a semi essential amino acid. L-Pro and its derivatives are utilized in organic reactions as an asymmetric catalyst. L-Pro has a pyrrolidine ring in side chain and it is considered as secondary amine. L-Leu is an essential amino acid. It is utilized in liver, adipose tissue and muscle tissue. L-Ile is an

essential amino acid. Isoleucine and Leucine both are having the same molecular formula but the difference is in its structure, especially the position of methyl group in the side chain. NR spectra of aliphatic amino acids as-received powder form are shown in figure 6.20.

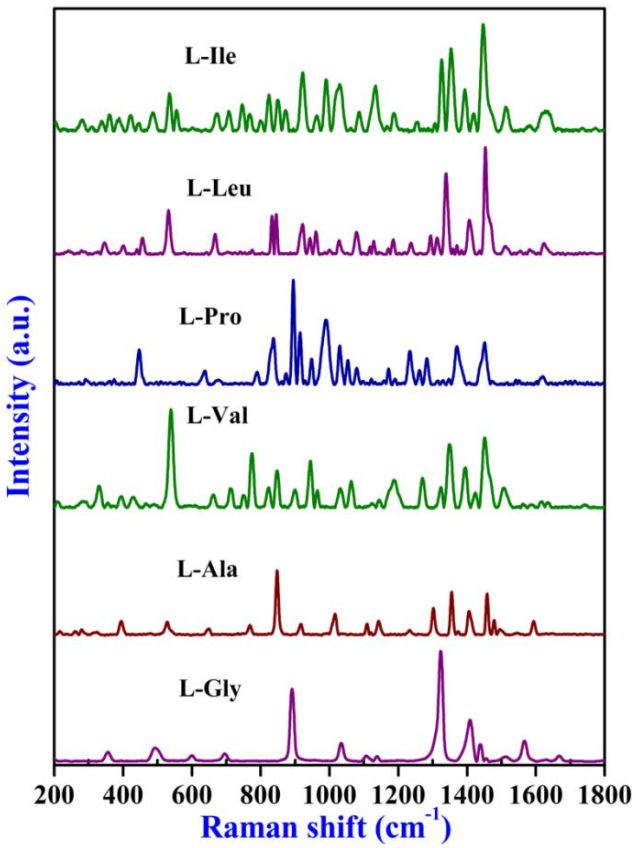


*Figure 6.20: Raman spectra of L-Gly, L-Ala, L-Val, L-Pro, L-Leu and L-Ile in the as-received powder form.*

SERS spectra of $10^{-6}$ M concentration of L-Gly, L-Ala and L-Val adsorbed on substrates are shown in figure 6.21. The Raman line of L-Gly observed at 891 $cm^{-1}$ in NR spectrum and 920 $cm^{-1}$ in SERS spectrum is due to C-C skeletal stretching. This line is intense in NR spectrum, whereas slightly lesser intense and blue shifted in SERS spectrum. SERS spectrum of

L-Ala is different from L-Gly in many ways. L-Ala has two C-C stretching bands, one at 843 $cm^{-1}$ (C-$CH_3$ stretching) and the second one at 917 $cm^{-1}$, these lines are not present in the L-Gly. Raman lines at 917 $cm^{-1}$ in the normal Raman spectrum and at 914 $cm^{-1}$ in SERS spectrum are due to single methyl group in the side chain. The L-Gly, L-Ala and L-L-Val SERS results are in accordance with previously reported one [3, 28]. In the appendix, tables T11-T13 show the peak assignments.

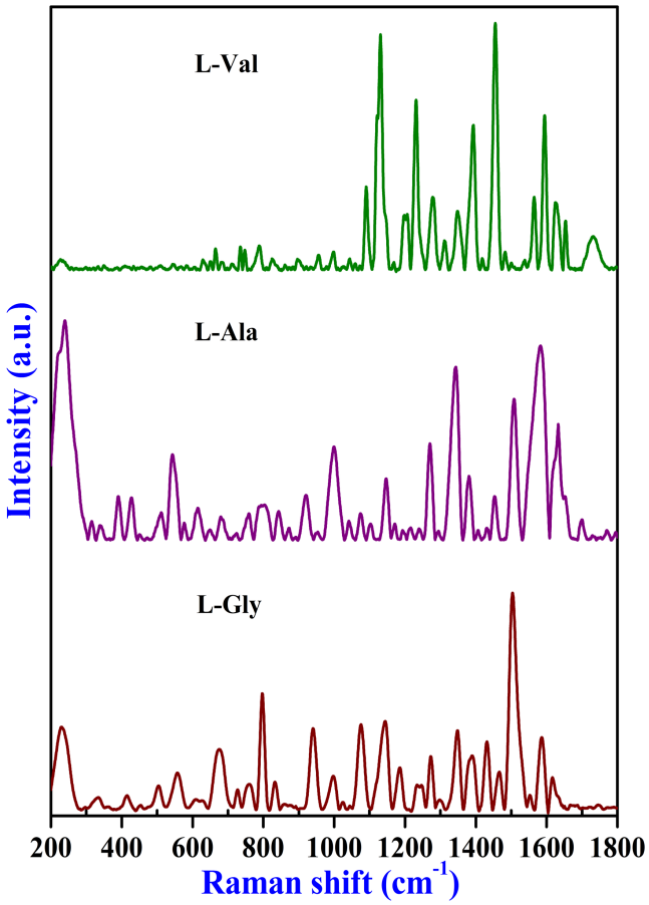


*Figure 6.21: SERS spectra of $10^{-6}$M L-Gly, L-Ala and L-Val adsorbed on Ag nanocluster substrate with laser excitation wavelength of 514.5 nm.*

SERS spectrum of $10^{-6}$ M of L-Pro, L-Leu and L-Ile adsorbed on substrates are shown in figure 6.22. The Raman line of L-Pro observed at 1171 $cm^{-1}$ in NR spectrum and the 1165 $cm^{-1}$ in SERS spectrum is due to secondary amine in the molecule. The intense Raman lines in NR and SERS spectra of L-Leu and L-Ile are attributed to C-C and C-H vibrational modes. Peak assignments are given in the tables T14-T16 (Appendix).

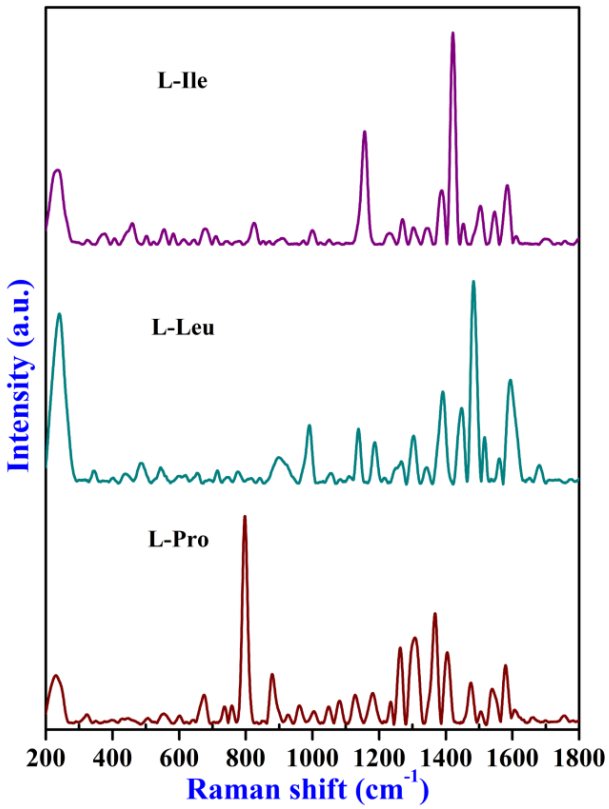


*Figure 6.22: SERS spectra of $10^{-6}$M L-Pro, L-Leu and L-Ile adsorbed on Ag nanocluster substrate with laser excitation wavelength of 514.5 nm.*

In addition to the common carboxylate mode (1400 $cm^{-1}$), the L-Gly line at 1140 $cm^{-1}$ ($NH_3^+$ deformation), the lines of L-Ala at 1460 $cm^{-1}$ ($CH_3$ asymmetric deformation), 1270 $cm^{-1}$ (CO stretching) and the 930 $cm^{-1}$ (CC stretching), the peaks of L-Val at 1550 $cm^{-1}$ ($COO^-$ asymmetric vibration)

and the 1200 $cm^{-1}$ ($CH_2$ twist and rock), the L-Pro line at 1165 $cm^{-1}$ ($NH_2^+$ deformation), the L-Leu peak at 1120 $cm^{-1}$ ($NH_3^+$ deformation) and the L-Ile lines at 1457 $cm^{-1}$ ($CH_2$ scissoring) and the 991 $cm^{-1}$ (C-C stretching) were taken for quantitative measurements. The intensities are plotted against molar concentrations as shown in figures F10-F15 (Appendix). The normalized intensities are depicted in figure 6.23 as a function of molar concentrations of aliphatic amino acids.

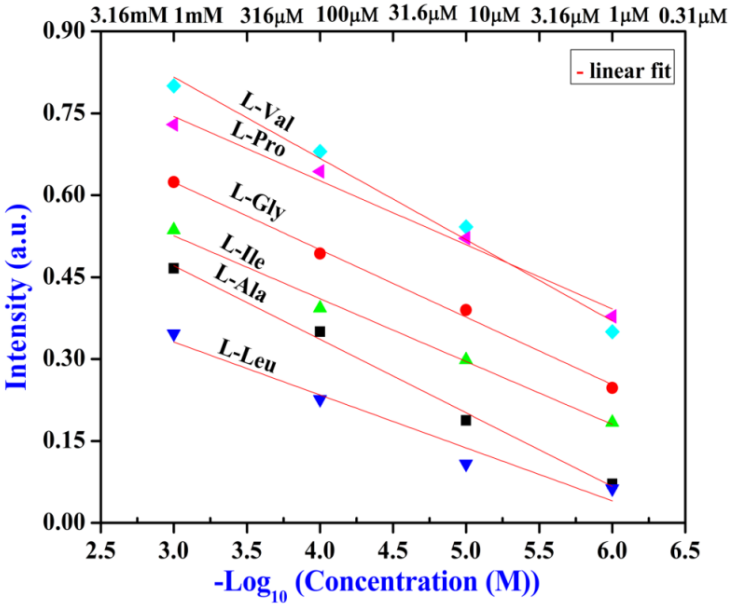


*Figure 6.23: Integrated intensities (sum of intensities of Raman lines normalized to intensity line of Ag-N) as a function of molar concentration of L-Leu, L-Ala, L-Ile, L-Gly, L-Pro and L-Val.*

## 6.7 Hydroxylic Amino Acids:

Hydroxylic group amino acids contain hydroxyl (-OH) functional group in the side chain. There are two amino acids in this group viz. L-Threonine (L-Thr) and L-Serine (L-Ser). The chemical structures of these two amino acids are given in figure 6.24.

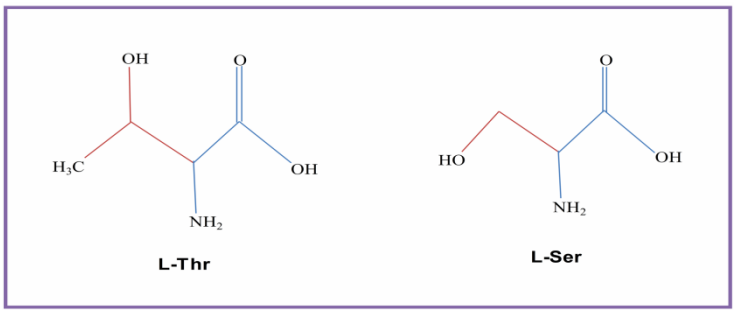


*Figure 6.24: Chemical structures of L-Thr and L-Ser.*

L-Thr is an essential amino acid. It is a precursor of Glycine and can be used as a prodrug to reliably elevate the Glycine levels in the brain. L-Ser is a non-essential amino acid. It is important in metabolism wherein it participates in the biosynthesis of purines and pyrimidines. NR spectra of L-Thr and L-Ser in the as-received powder form are shown in figure 6.25.

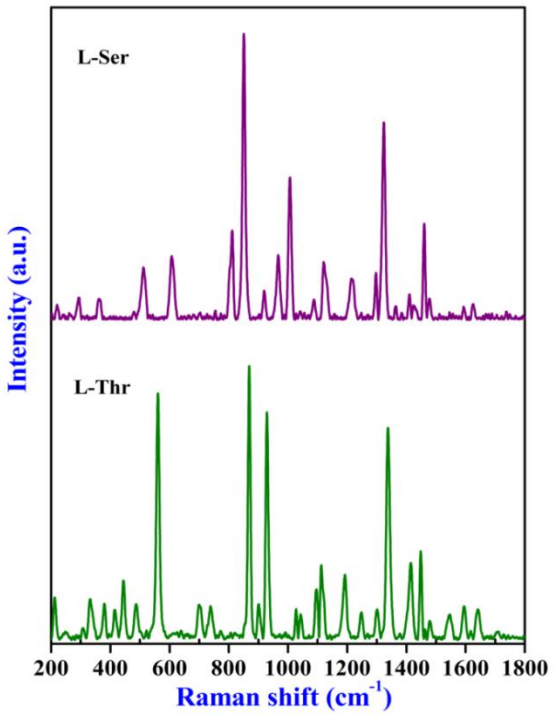


*Figure 6.25: Raman spectra of L-Thr and L-Ser in the as-received powder form.*

L-Thr and L-Ser results are in accordance with the reported literature [7, 3]. L-Thr has the functional group of secondary alcohol. The OH deformation mode is observed at 1042 $cm^{-1}$. The intense Raman line at 869 $cm^{-1}$ is due to CCN stretching. The intense Raman band at 1338 $cm^{-1}$ and weak bands at 1448 $cm^{-1}$ are attributed to the CH deformation modes. The Raman lines at 1112 $cm^{-1}$ and the 1248 $cm^{-1}$ are ascribed to $NH_3$ rocking and $NH_3^+$ deformation, respectively.

L-Ser has primary alcohol in the side chain. The Raman line due to C-C-O symmetric stretching vibration of primary alcohol is presented at 811 $cm^{-1}$. The band at 1006 $cm^{-1}$ is due to C-O-H deformation of alcoholic hydroxyl. An intense Raman line is observed at 850 $cm^{-1}$ and this is ascribed to CC skeletal stretch.

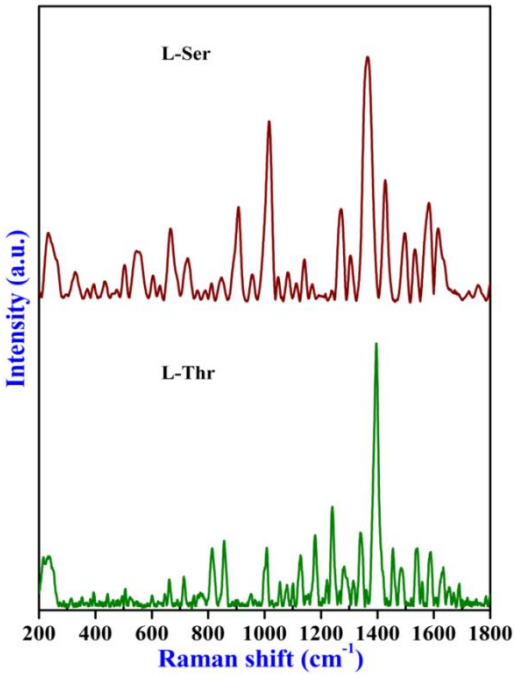


*Figure 6.26: SERS spectra of $10^{-6}$M L-Thr and L-Ser adsorbed on Ag nanocluster substrate with laser excitation wavelength of 514.5 nm.*

SERS spectra of $10^{-6}$ M L-Thr and L-Ser adsorbed on substrates are shown in figure 6.26. A comparison has been made of normal Raman and SERS spectra and summarized in the tables T17 and T18 (Appendix).

L-Thr Raman line at 891 $cm^{-1}$ (C-C stretching) and the Raman line of L-Ser at 1323 $cm^{-1}$ ($CH_2$ wagging) were taken for quantitative measurements. The intensities as a function of molar concentration are depicted in figures F16-F17 (Appendix). The normalized intensities as a function of molar concentrations are depicted in figure 6.27.

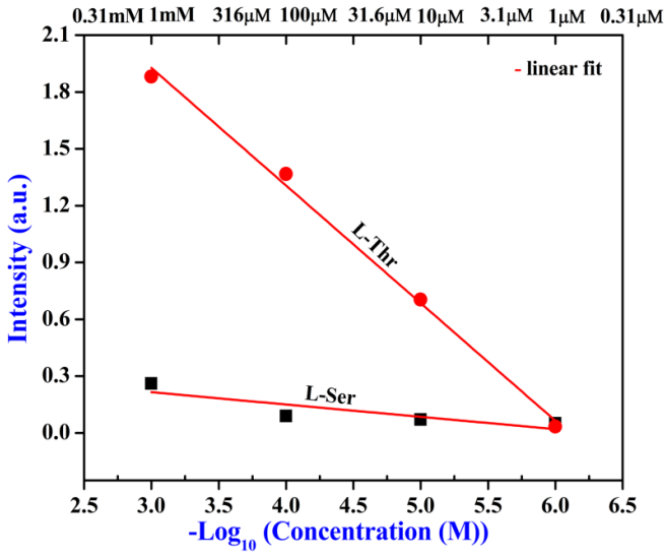


*Figure 6.27: Integrated intensities (sum of intensities of Raman lines normalized to intensity line of Ag-N) as a function of molar concentration of L-Thr and L-Ser.*

## 6.8 Sulphur containing Amino Acids:

This group of amino acids contain Sulphur atom in the side chain. There are two amino acids in this group namely L-Methionine (L-Met) and L-Cysteine (L-Cys) out of which only the first one was studied in this work.

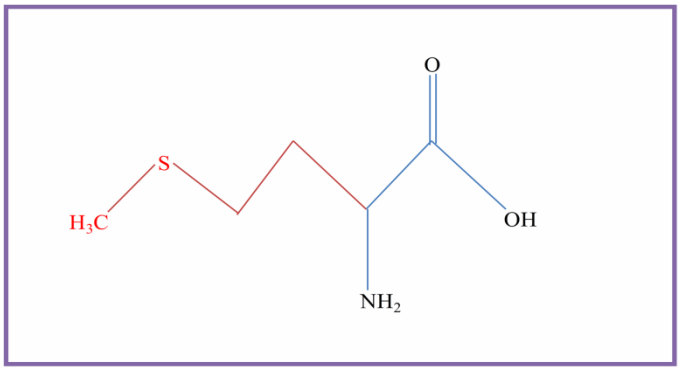


*Figure 6.28: L-Met chemical structure.*

Figure 6.28 shows the L-Methionine (L-Met) chemical structure. It is an essential amino acid. It is essential for normal metabolism, maintenance and growth of body tissue. L-Met helps to initiate translation of messenger RNA. NR spectrum of L-Met in the as-received powder form is shown in figure 6.29. Intense line at 718 $cm^{-1}$ is ascribed to S-$CH_3$ stretching.

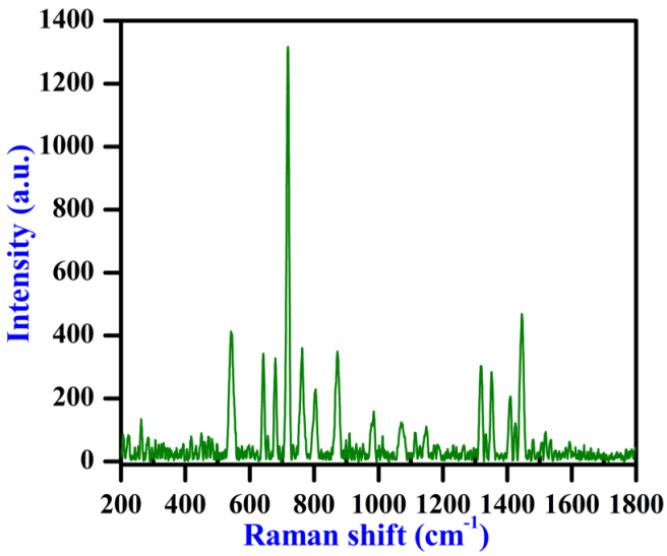


*Figure 6.29: Raman spectrum of L-Met in the as-received powder form.*

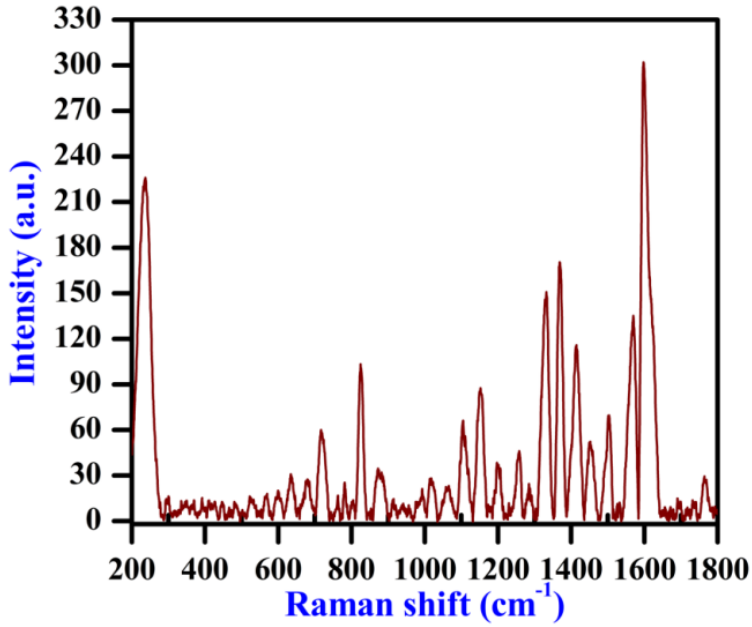


*Figure 6.30: SERS spectrum of $10^{-6}$M L-Met adsorbed on Ag nanocluster substrate with laser excitation wavelength of 514.5 nm.*

SERS spectrum of $10^{-6}$ M of L-Met adsorbed on substrate is shown in figure 6.30. L-Met contains sulphur atom in its side chain. The indicative vibrational modes of sulphur are present at 679 $cm^{-1}$ and 674 $cm^{-1}$ (C-S stretching) in NR and SERS spectra, respectively. The Raman lines at 718 $cm^{-1}$ in NR and 716 $cm^{-1}$ in SERS spectra are due to S-$CH_3$ stretching. A comparison of the Raman shifts of NR and the SERS spectra is given in table T19 (Appendix) in which the peak assignments are also given.

The Raman line at 1410 $cm^{-1}$ ($COO^-$ symmetric stretching) was taken for quantitative measurements. The intensity as a function of molar concentration is plotted in figure F18 (Appendix). The normalized intensity as a function of molar concentration is shown in figure 6.31. A good correlation has been found between intensity of Raman lines and molar concentration.

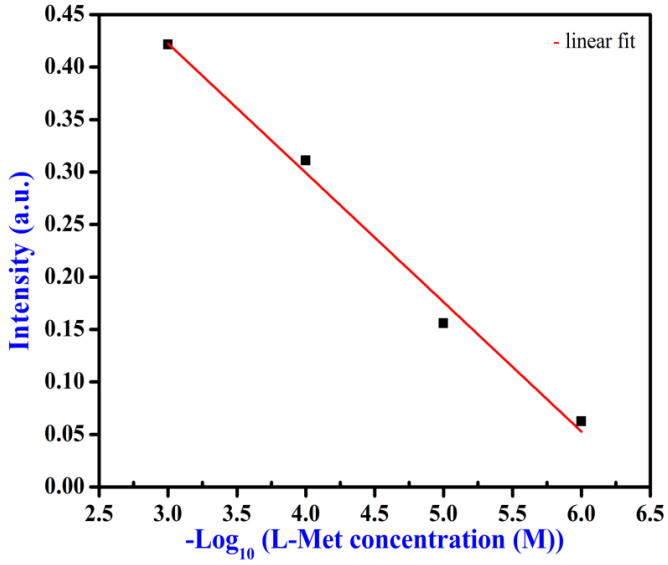


*Figure 6.31: Integrated intensity (sum of intensities of Raman lines normalized to intensity line of Ag-N) as a function of molar concentration of L-Met.*

## 6.9 Conclusions:

L-amino acids were detected up to 1μM concentration levels using Surface Enhanced Raman Spectroscopy. The characteristic Raman lines were identified for each of the amino acids. A new Raman line observed in all the 19 L-amino acids in the region of 230-240 cm $^{-1}$ due to the formation of Ag-N bond between the amino acid and silver surface was taken to normalize the intensity of the characteristic Raman lines. The variation of normalized intensity with molar concentration showed a good linear correlation between the two quantities for all the amino acids studied. We have thus been able to provide for the first time a quantitative method for the assessment of the amino acids up to a low concentration level of 1 μM in aqueous solutions. It is expected that SERS can serve as a sensitive tool to detect these bio-molecules and quantify their concentrations in more complex systems such as proteins and enzymes.

**References:**

[1] S. Maryam, M. Abdolreza and F. Maryam, "Application of a quartz crystal nanobalance and principal component analysis for the detection and deter- mination of histidine" *Anal. Bioanal. Chem. 391 (2008) 2875.*

[2] J.S. Suh and M. Moskovits, "Surface-Enhanced Raman Spectroscopy of Amino Acids and Nucleotide Bases Adsorbed on Silver" *J. Am. Chem. Soc. 108 (1986) 4711.*

[3] S. Stewarts and P.M. Fredericks, "Surface-enhanced Raman spectroscopy of amino acids adsorbed on an electrochemically prepared silver surface" *Spectrochim. Acta. A 55 (1999) 1641.*

[4] E. Podstawka, Y. Ozaki and L.M. Proniewicz, "Part I: Surface-Enhanced Raman Spectroscopy Invesigation of Amino Acids and Their Homopeptides adsorbed on Colloidal Silver" *App. Spectrosc. 58 (2004) 570.*

[5] E. Podstawka, Y. Ozaki and L.M. Proniewicz, "Part III: Surface-Enhanced Raman Scattering of Amino Acids and Their Homopeptide Monolayers Deposited onto Colloidal Gold Surface" *App. Spectrosc. 59 (2005) 1516.*

[6] J. Guicheteau, L. Argue, A. Hyre, M. Jacobson and S.D. Christesen, "Raman and Surface-enhanced Raman spectroscopy of amino acids and nucleotide bases for target bacterial vibrational mode identification" *Proc. of SPIE Vol. 6218, 621800 (2006).*

[7] G. Zhu, X. Zhu, Q. Fan and X. Wan, "Raman spectra of amino acids and their aqueous solutions" *Spectrochim. Acta. A 78 (2011) 1187.*

[8] H. Lin, Q. Shao, F. Hu, H. Wang and M. Shao, "A direct detection of amino acids with surface-enhanced Raman scattering: Cu nanoparticle-coated

copper vanadate nanoribbons from mechanochemistry" *Thin Solid Films 558 (2014) 385.*

[9] A. Brambilla, A. Philippidis, A. Nevin, D. Comelli, G. Valentini and D. Anglos, "Adapting and testing a portable Raman spectrometer for SERS analysis of amino acids and small peptides" *J. Mol. Struct. 1044 (2013) 121.*

[10] I.R. Nabiev, S.D. Trakhanov, E.S. Efremov, V.V. Marinyuk and R.M. Lasorenko-Manevich, " Surface Enhanced Raman-Spectra of some biological molecules adsorbed at silver electrodes" *Bioorg. Khim.* 7 (1981) 941.

[11] A. Kaminska, O. Inya-Agha, R.J. Foster and T.E. Keyes, "Chemically bound gold nanoparticle arrays on silicon: assembly, properties and SERS study of protein interactions" *Phys. Chem. Chem. Phys. 10 (2008) 4172.*

[12] J. Guicheteau, S. Christesen, D. Emge, P. Wilcox and A.W. Fountain III, "Assessing Metal Naonofabricated Substrates for Surface-Enhanced Raman Scattering (SERS) Activity and Reproducibility" *Appl. Spectrosc. 65 (2011) 144.*

[13] F. Ota, S. Higuchi, Y. Gohshi, K. Furuya, M. Ban and M. Kyoto, "Some Considerations of the SERS Effect of L-Phenylalanine in the Near-Infrared Region Using Silver Colloid Solution" *J. Raman Spectrosc. 28 (1997) 849.*

[14] C.H Chuang and Y.T Chen, "Raman scattering of L-Tryptophan enhanced by surface plasmon of silver nanoparticles: vibrational assignment and structural determination" *J. Raman Spectrosc. 40 (2009) 150.*

[15] A. Kandakkathara, I. Utkin and R. Fedosejevs, "Surface-Enhanced Raman Scattering (SERS) Detection of Low Concentrations of Tryptophan Amino Acid in Silver Colloid" *Appl. Spectrosc. 65 (2011) 507.*

[16] A.E. Aliaga, I.O. Román, P. Leyton, C. Garrido, J. Cárcamo, C. Caniulef, F. Célis, G. Díaz F., E. Clavijo, J.S. Gómez-Jeria and M.M. Campos-Vallette, "Surface-enhanced Raman scattering study of L-Tryptophan" *J. Raman Spectrosc. 40 (2009) 164.*

[17] H.I. Lee, M.S. Kim and S.W. Suh, "Raman Spectroscopy of L-Phenylalaline, L-Tyrosine, and their Peptides Adsorbed on Silver Surface" *Bull. Korean Chem. Soc. 9 (1988) 218.*

[18] M.L. Cheng, B.C. Tsai and J. Yang, "Silver nanoparticle-treated filter paper as a highly sensitive surface-enhanced Raman scattering (SERS) substrate for detection of tyrosine in aqueous solution" *Anal. Chim. Acta 708 (2011) 89.*

[19] Y. Zhao, M. Shao, R. Que and Z. Zhang, "The surface-enhanced Raman scattering for monitoring histidine and tyrosine using silver vanadate nanoribbons as substrates" *J. Phys. Chem. Solid. 74 (2013) 255.*

[20] M. Muntaz-Miranda, N. Neto and G. Sbrana, "Surface Enhanced Raman Scattering of Pyrazine adsorbed on silver colloidal particles" *J. Mol. Strcut. 143 (1986) 275.*

[21] R.J. Sundberg and R.B. Martin, "Interactions of histidine and other imidazole derivatives with transition-metal ions in chemical and biological-systems" *Chem. Rev. 74 (1974) 471.*

[22] A.E. Aliaga, C. Garrido, P. Leyton, G. Díaz F., J.S. Gómez-Jeria, T. Aguayo, E. Clavijo, M.M. Campos-Vallette and S. Sanchez-Cortes, "SERS and theoretical studies of Arginine" *Spectrochim. Acta A 76 (2010) 458.*

[23] J.D. Gelder, K.D. Gussem, P. Vandenabeele and L. Moens, "Reference database of Raman spectra of biological molecules" *J. Raman Spectrosc. 38 (2007) 1133.*

[24] S. Martusevičius, G. Niaura, Z. Talaikytė and V. Razumas, "Adsorption of L-Histidine on copper surface as evidenced by surface-enhanced Raman scattering spectroscopy" *Vib. Spectrosc. 10 (1996) 271.*

[25] A.E. Aliaga, I.O. Román, C. Garrido, P. Leyton, J. Cárcamo, E. Clavijo, C. Caniulef, J.S. Gómez-Jeria, G. Díaz F., and M.M. Campos-Vallette, "Surface-enhanced Raman scattering study of L-Lysine" *Vib. Spectrosc. 50 (2009) 131.*

[26] R. Slojkowska, B. Palys and M. Jurkiewicz-Herbich, "Adsorption of asparagine on the gold electrode and air/solution interface" *Electro. Chim. Acta 49 (2004) 4109.*

[27] J.L. Castro, M.A. Montanez, J.C. Otero and J.J. Marcos, "SERS and Vibrational Spectra of Aspartic Acid" *J. Mol. Struct. 349 (1995) 113.*

[28] J. Guicheteau, L. Argue, A. Hyre, M. Jacobson and S.D. Christesen, "Raman and surface-enhanced Raman spectroscopy of amino acids and nucleotide bases for target bacterial vibrational mode identification" *Proc. of SPIE Vol. 6218, 62180O, (2006).*

# Appendix

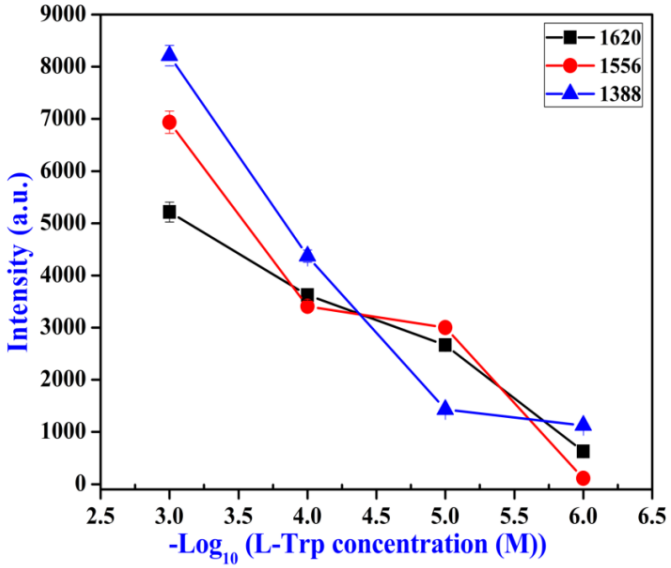


*Figure F1: Raman lines intensity variation with molar concentration of L-Trp.*

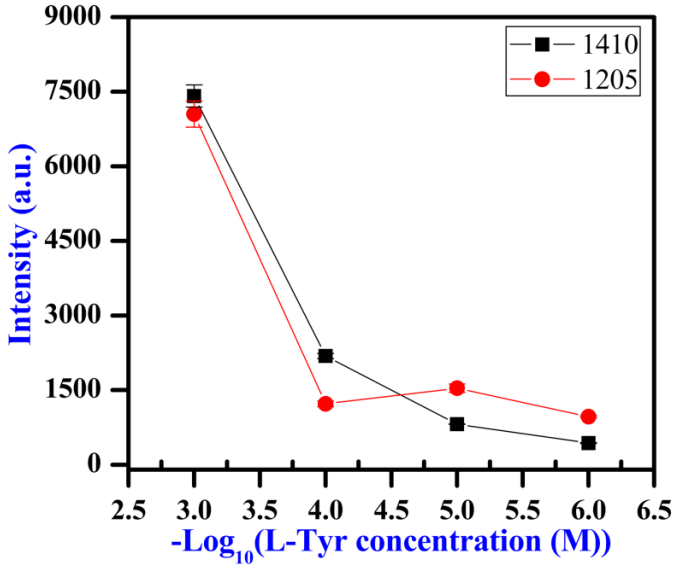


*Figure F2: Raman lines intensity variation with molar concentration of L-Tyr.*

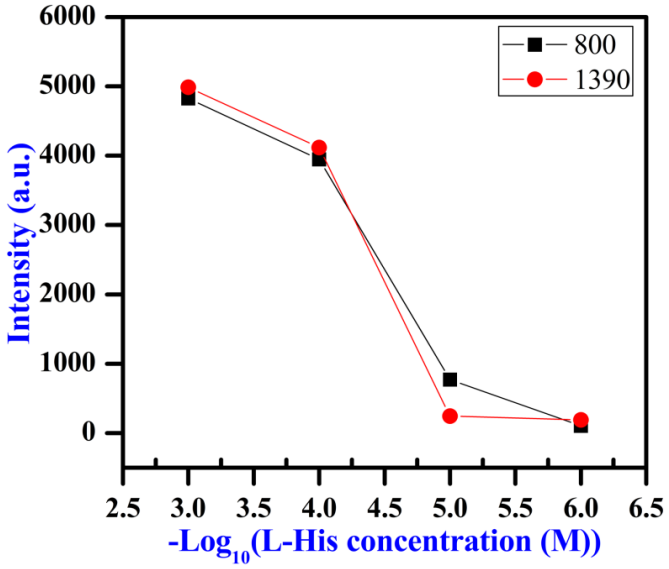


*Figure F3: Raman lines intensity variation with molar concentrations of L-His.*

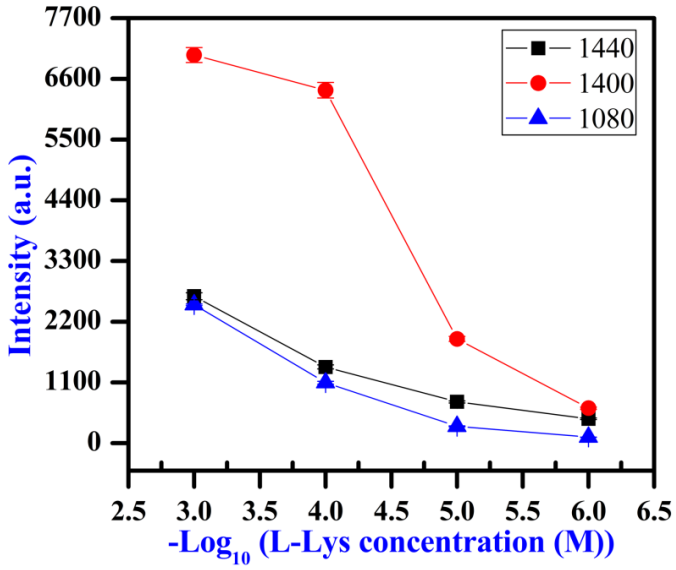


*Figure F4: Raman lines intensity variation with molar concentration of L-Lys.*

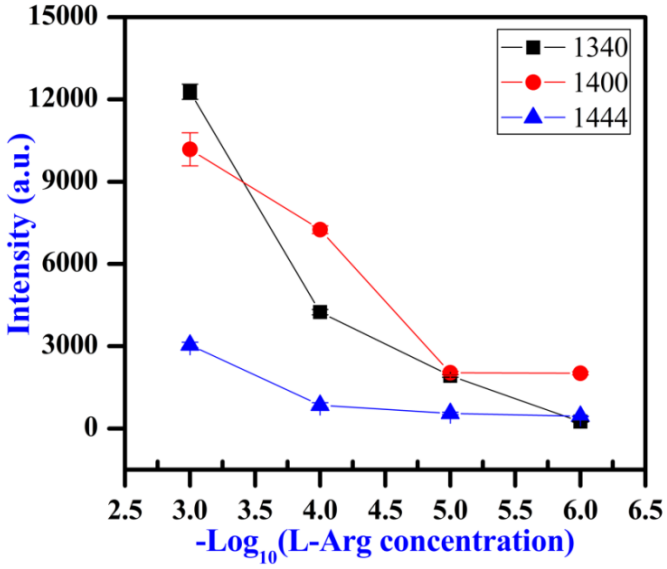


*Figure F5: Raman lines intensity variation with molar concentration of L-Arg.*

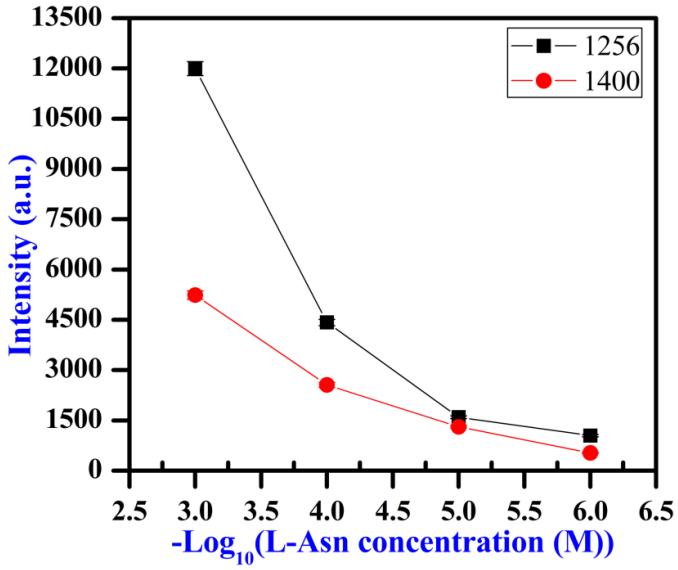


*Figure F6: Raman lines intensity variation with molar concentrations of L-Asn.*

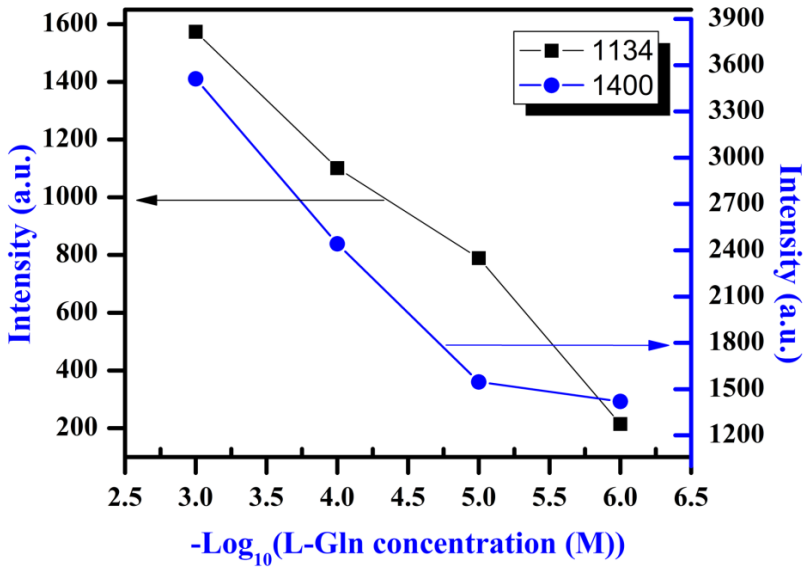


*Figure F7: Raman lines intensity variation with molar concentrations of L-Gln.*

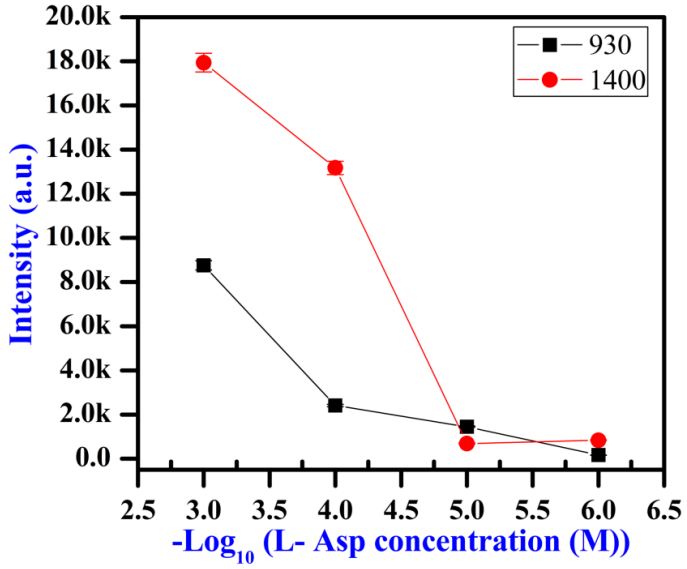


*Figure F8: Raman lines intensity variation with molar concentrations of L-Asp.*

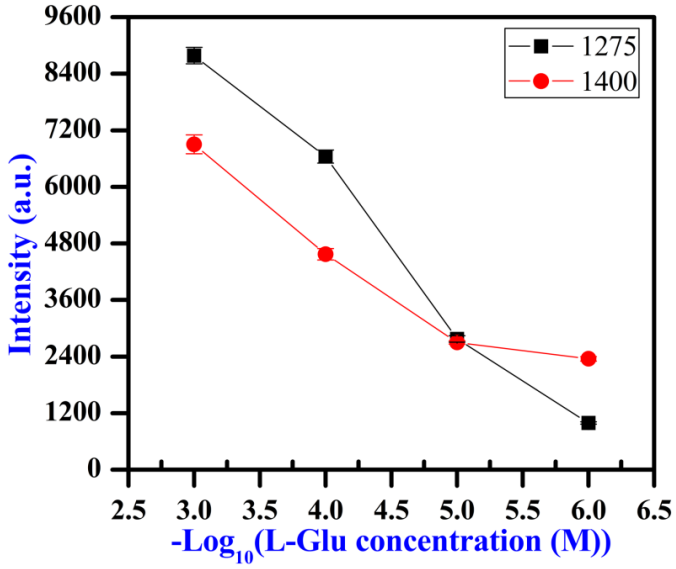


*Figure F9: Raman lines intensity variation with molar concentrations of L-Glu.*

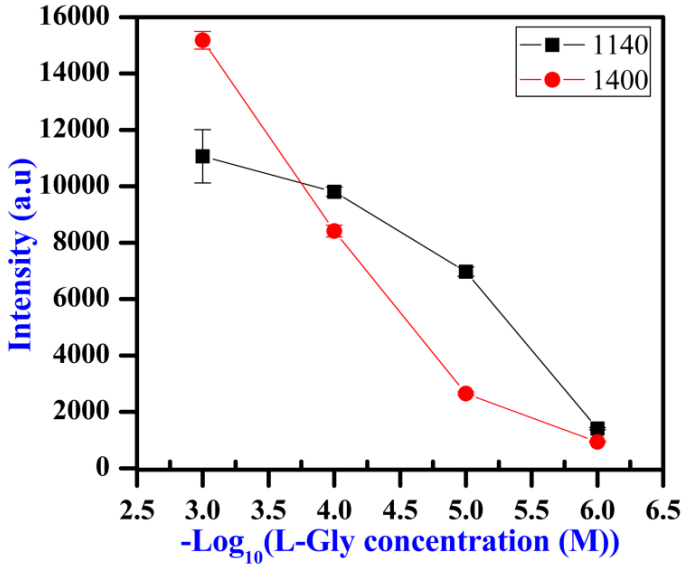


*Figure F10: Raman lines intensity variation with molar concentrations of L-Gly.*

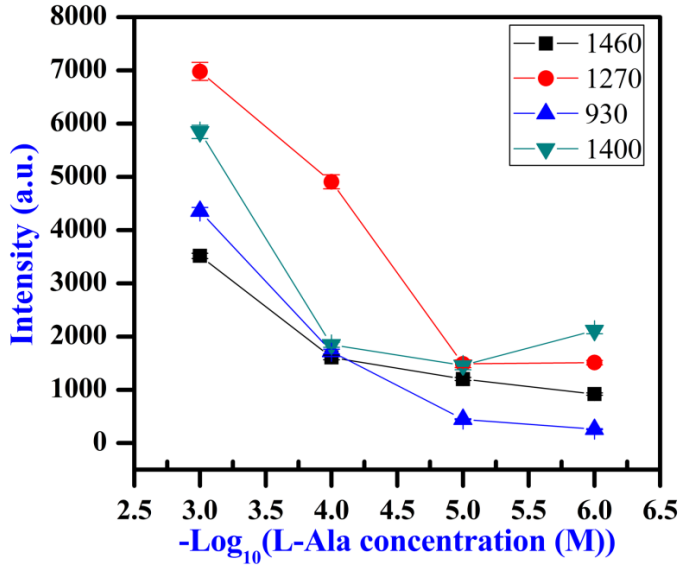


*Figure F11: Raman lines intensity variation with molar concentrations of L-Ala.*

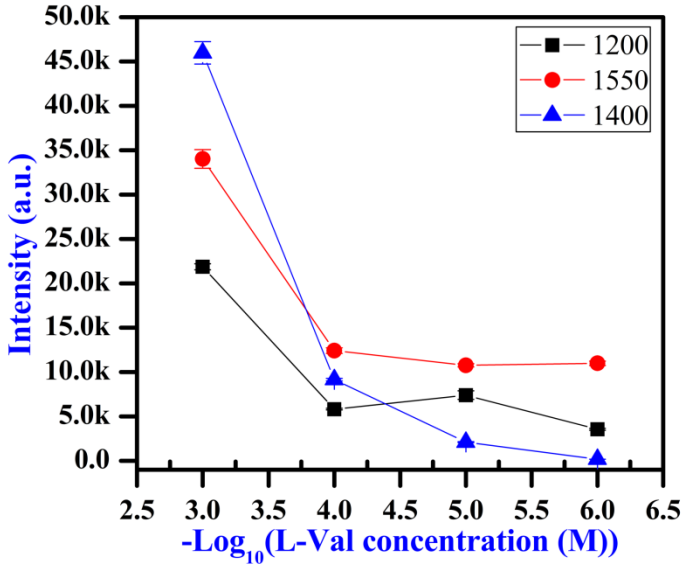


*Figure F12: Raman lines intensity variation with molar concentrations of L-Val.*

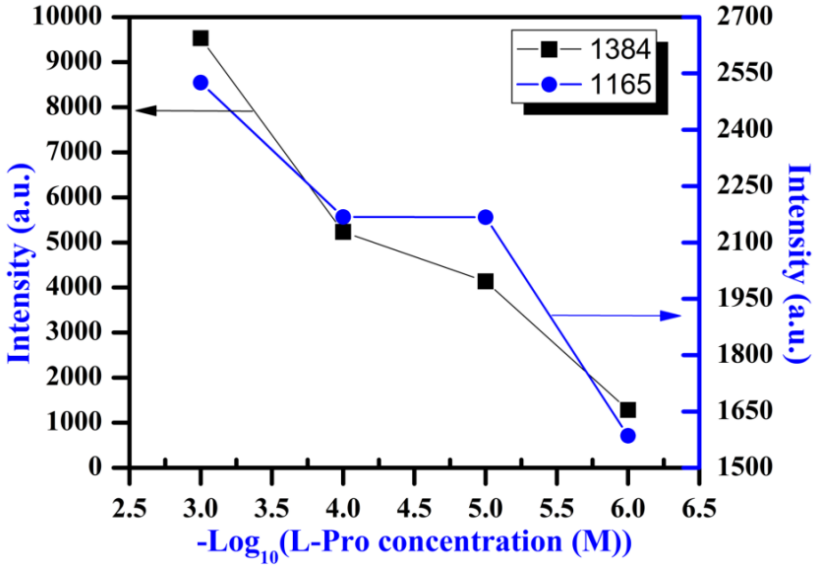


*Figure F13: Raman lines intensity variation with molar concentrations of L-Pro.*

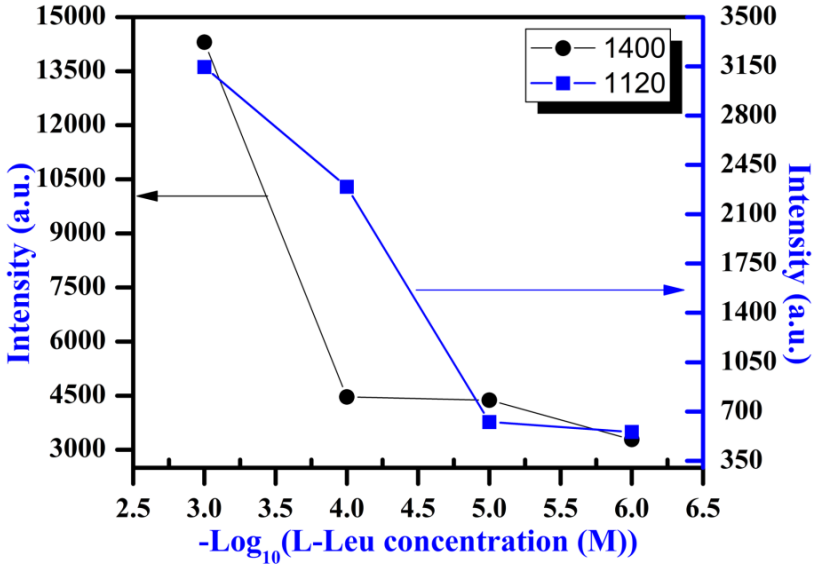


*Figure F14: Raman lines intensity variation with molar concentrations of L-Leu.*

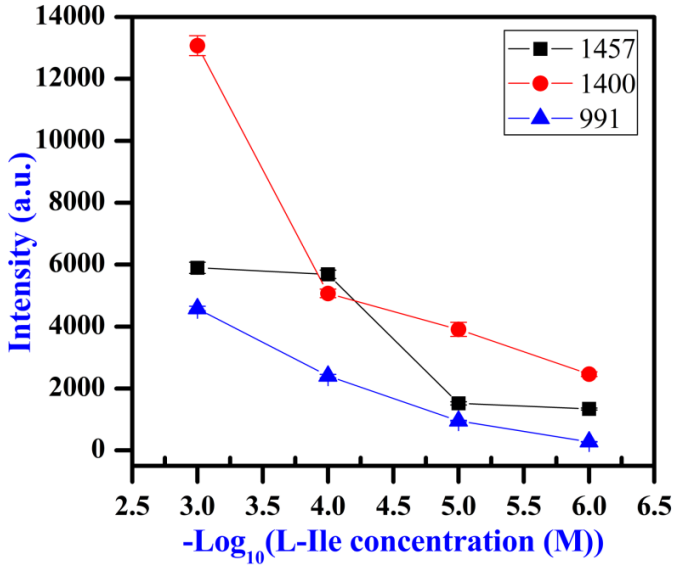


*Figure F15: Raman lines intensity variation with molar concentrations of L-Ile.*

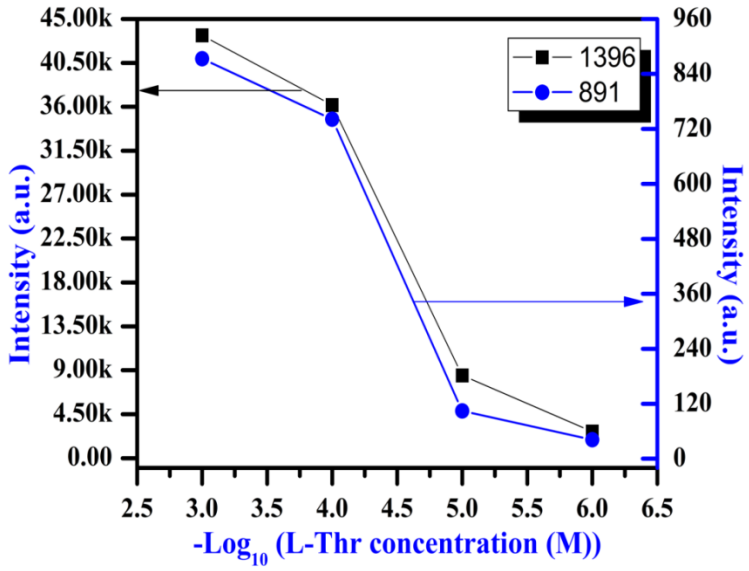


*Figure F16: Raman lines intensity variation with molar concentrations of L-Thr.*

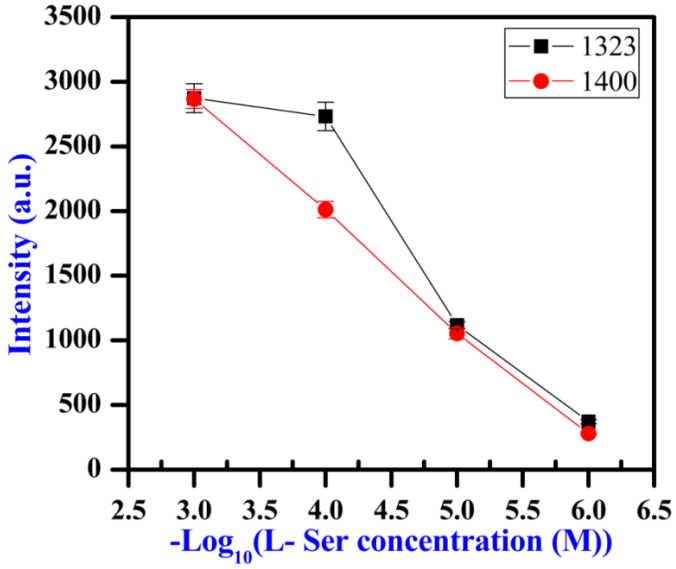


*Figure F17: Raman lines intensity variation with molar concentrations of L-Ser.*

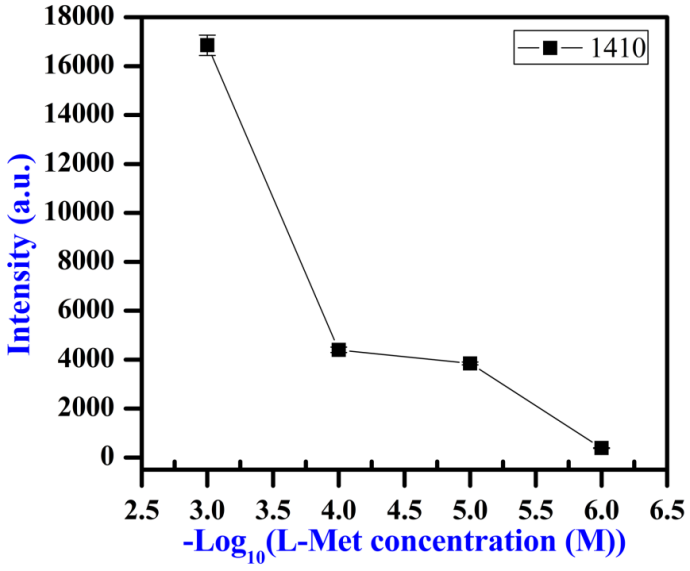


*Figure F18: Raman lines intensity variation with molar concentrations of L-Met.*

*Table T1: L-Phenylalanine (L-Phe) peak assignments and comparison of normal Raman and SERS spectra.*

| Assignment | Normal Raman | SERS |
|---|---|---|
| Ag-N | | 242 |
| | 316 | |
| | 358 | 362 |
| | 410 | 404 |
| | 464 | 475 |
| CO twisting+C=O bending | 525 | 510 |
| | | 564 |
| | 599 | |
| Ring deformation (monosubstituted benzenes) | 619 | 616 |
| | | 651 |
| | 676 | 679 |
| | 744 | 742 |
| | 783 | 775 |
| $CH_2$ rock | 825 | 833 |
| C-C skeletal stret./C-$CH_3$ stret. | 852 | |
| | | 890 |
| C-C stretching/C-$COO^-$ Stretching vibration | 910 | |
| Typical ring vibration | | 930 |
| | 950 | 975 |
| Ring breathing mode | 1000 | 1000 |
| In plane CH deformation( monosubstituted benzenes)Phenol Ring | 1031 | 1028 |
| | | 1078 |
| CCN asymmetric Stretching | | 1120 |
| | 1154 | 1150 |
| $CH_2$ twist and rock/$NH_3$ rocking/CH-$NH_2$ | 1183 | 1179 |
| C6H5-C vibration/ Phenol C stretching | | 1199 |
| Phenol ring | 1214 | 1219 |
| | | 1243 |
| | | 1273 |
| $CH_2$ wagging | 1305 | 1298 |
| | 1336 | 1344 |

| | | |
|---|---|---|
| | 1352 | |
| $COO^-$ stretching vibration | 1407 | 1390 |
| $CH_2$ scissoring | 1441 | 1440 |
| | | 1454 |
| | | 1529 |
| Ring CC stretching | 1582 | 1561 |
| Ring CC stretching | 1604 | 1592 |

*Table T2: L-Tryptophan (L-Trp) peak assignments and comparison of normal Raman and SERS spectra.*

| Assignment | Normal Raman | SERS |
|---|---|---|
| Ag-N | 234(186) | 231(205) |
| CH-$CH_2$ twisting | 346(189) | 341(35) |
| | | 397(15) |
| Deformation of benzene ring, pyrrole ring | 422(182) | 428(40) |
| CH-$CH_2$ twisting | 499(182) | 504(23) |
| | 531 | 530 |
| | 569 | |
| | 592 | |
| | 623 | 615 |
| | | 656 |
| | 683 | |
| | 702 | |
| | 738 | 731 |
| Benzene stretching/Pyrrole in- phase breathing | 752 | 761 |
| | 800 | |
| | | 815 |
| N-H bending, indole ring vibration | 874 | |
| | 894 | |
| | 925 | 935 |
| | 982 | |
| Benzene/pyrrole out-of-phase breathing | 1002 | 1011 |
| | | 1059 |
| C-N stretch/amino terminal | 1073 | 1089 |

| | | |
|---|---|---|
| group/$NH_3$ twist | | |
| | 1117 | 1125 |
| CCN asymmetric stretching | | 1154 |
| | | 1214 |
| | 1229 | |
| | 1250 | |
| | | 1275 |
| Aliphatic $CH_2$ deformation | 1312 | |
| Tryptophan doublet in proteins | 1336 | 1331 |
| Fermi resonance N-C in pyrrole ring | 1355 | |
| $COO^-$ symmetric stretching | | 1388 |
| C-X-C stretch, substituted pyrroles | 1420 | 1428 |
| | 1455 | 1457 |
| | 1483 | 1508 |
| C-C stretching, Pyrrole ring | 1553 | 1556 |
| C-C stretching | | 1560 |
| C=C out-of-phase stretch | 1572 | |
| Indole N-H vibration | 1615 | 1620 |

*Table T3: L-Tyrosine (L-Tyr) peak assignments and comparison of normal Raman and SERS spectra.*

| Assignment | Normal Raman | SERS |
|---|---|---|
| Ag-N | | 233 |
| | | 394 |
| | 427 | 436 |
| | | 515 |
| Parasubstituted benzene | 637 | |
| | | 684 |
| | 710 | 712 |
| | 739 | |
| | | 781 |
| | 794 | |
| Tyr doublet/phenol ring breathing/disubstituted benzenes | 826 | 826 |
| | 843 | |
| | | 863 |
| | | 886 |
| | | 950 |

| | | |
|---|---|---|
| | 982 | |
| | | 996 |
| C-$NH_2$ stretching/$CH_2$ rocking | 1040 | |
| | | 1096 |
| | | 1147 |
| $CH_2$ twist and rock | 1175 | |
| | 1197 | |
| Ring stretching | | 1205 |
| | 1211 | |
| C-O stretching | 1243 | |
| C-O stretching | 1263 | |
| | 1282 | 1270 |
| | | 1316 |
| Ring stretching | 1327 | |
| | | 1348 |
| Ring stretching | 1365 | |
| $COO^-$ symmetric Stretching | 1418 | 1410 |
| | 1433 | |
| | | 1455 |
| C-H bending | | 1499 |
| | | 1532 |
| C-OH stretching | 1585 | 1583 |
| Ring vibration/ring stretching, benzene derivative | 1611 | |

*Table T4: L-Histidine (L-His) peak assignments and comparison of normal Raman and SERS spectra.*

| Assignment | Normal Raman | SERS |
|---|---|---|
| | 210 | 216 |
| Ag-N | 237 | 240 |
| | 314 | 297 |
| | 333 | 333 |
| | 360 | 368 |
| | 399 | |
| | | 473 |
| | | 514 |
| | 535 | 534 |

| | | |
|---|---|---|
| Ring in plane bend | 623 | |
| Ring in plane bend | 653 | 649 |
| $COO^-$ deformation | 728 | 710 |
| | | 746 |
| COOH bend | 781 | |
| Imidazole ring breathing | 801 | 800 |
| | 821 | |
| C-C stretching+ ring bend | 850 | 864 |
| | | 893 |
| C-H in plane | 915 | |
| C-$COO^-$ stretching | 929 | 931 |
| | 959 | 961 |
| C-N stretching+ ring bend | 973 | |
| | | 992 |
| N-H bend, in plane (N twist) | 1057 | 1040 |
| C-N stretching, C-H bend | 1084 | |
| C-N stretching, C-H bend | 1108 | |
| | 1136 | 1126 |
| N-H waging | | 1157 |
| Stretching C-N, N-H in-plane bending | 1171 | |
| Imidazole ring deformation | | 1196 |
| | 1220 | |
| | 1247 | 1247 |
| | 1267 | 1272 |
| | 1314 | 1303 |
| ring (C-N) stretching | 1344 | 1326 |
| | | 1364 |
| $COO^-$ symmetric Stretching | 1404 | 1390 |
| | 1426 | |
| | | 1445 |
| N-H in-plane bending | 1472 | 1478 |
| N-H in-plane bending | 1495 | |
| | 1538 | 1524 |
| C-C stretching + N-H bending | 1568 | 1580 |
| | | 1634 |

*Table T5: L-Lysine (L-Lys) peak assignment and comparison of normal Raman and SERS spectra.*

| Assignment | Normal Raman | SERS |
|---|---|---|
| Ag-N | | 236(242) |
| | 297(193) | |
| | 362(332) | |
| | 441(1100) | |
| | | 499(8) |
| | 535(758) | |
| | | 558 |
| | 637 | 625 |
| | | 679 |
| $COO^-$ deformation | 690 | |
| | 771 | |
| | 821 | |
| C-N Stretching | 868 | |
| | | 892 |
| υ C-$COO^-$ mode | 940 | 945 |
| | 1006 | 1003 |
| C-N stretching | 1065 | |
| C-N stretching | | 1080 |
| | 1104 | |
| N-H waging | 1140 | 1134 |
| | 1196 | |
| | 1270 | 1275 |
| | 1292 | |
| CH bend | 1344 | 1349 |
| $COO^-$ symmetric stretching | 1397 | 1400 |
| $CH_2$ scissoring | 1424 | |
| $CH_2$ scissoring + NH deformation | | 1440 |
| | | 1507 |
| | 1525 | |
| $COO^-$ asymmetric stretching | 1572 | 1573 |

*Table T6: L-Arginine (L-Arg) peak assignments and comparison of normal Raman and SERS spectra.*

| Assignment | Normal Raman | SERS |
|---|---|---|
| Ag-N | | 233(184) |
| | 298(125) | |
| | 365(124) | |
| | | 469(47) |
| | 493(110) | 513(60) |
| | 551(134) | |
| $COO^-$ deformation | 613 | |
| | 651 | |
| | | 715 |
| | | 815 |
| | | 886 |
| | 920 | 915 |
| $CH_2$ mode | 983 | 976 |
| $NH_3^+$ wagging | 1033 | 1028 |
| NH deformation GF | 1070 | |
| | 1099 | 1102 |
| | 1120 | |
| $NH_2$ rocking vibration | | |
| | 1194 | 1174 |
| | | 1200 |
| | | 1129 |
| $CH_2$ bending | 1264 | 1274 |
| $CH_2$ bending | 1304 | 1310 |
| $CH_2$ wagging | 1328 | |
| CH deformation | | 1340 |
| $COO^-$ symmetric Stretching | | 1400 |
| NH vibration of the guanidinium fragment (GF) | 1437 | 1444 |
| Deformation $CH_2$ Aliphatic Fragment (AF) | 1475 | |
| $NH_3^+$ symmetric deformation | | 1501 |
| | | 1538 |
| | | 1618 |
| | | 1642 |

*Table T7: L-Asparagine (L-Asn) peak assignments and comparison of normal Raman and SERS spectra.*

| Assignment | Normal Raman | SERS |
|---|---|---|
| | 193(179) | |
| Ag-N | | 237(232) |
| | 326(166) | 337(70) |
| | 373(51) | |
| | 411 | 427 |
| $COO^-$ rocking/CC bending/amide bending | 450 | |
| | | 495 |
| O=C-N skeletal deformation | 540 | 554 |
| | 583 | |
| | | 676 |
| $COO^-$ deformation | | 735 |
| $CH_2$ and $CH_3$ rocking | 756 | |
| CC stretching | | 780 |
| C-C stretching | 876 | 887 |
| C-C stretching/CCN stretch/$COO^-$ stretch | 940 | 954 |
| C-C stretching | 987 | |
| | | 1006 |
| C-C stretching/C-O stretching | 1071 | |
| | | 1098 |
| $NH_2$ rock | 1114 | |
| $NH_3^+$ deformation | 1156 | 1151 |
| | | 1188 |
| $CH_2$ wagging | 1262 | 1256 |
| | | 1289 |
| CH deformation | 1329 | |
| $CH_2$ scissoring | 1356 | 1352 |
| $COO^-$ symmetric stretching | 1416 | 1400 |
| | | 1425 |
| | 1501 | |
| | | 1526 |
| | 1561 | |
| | | 1582 |
| C=O Stretching | 1620 | 1625 |

*Table T8: L-Glutamine (L-Gln) peak assignments of normal Raman and SERS spectra.*

| Assignment | Normal Raman | SERS |
|---|---|---|
| Ag-N | 238 | 236 |
| | 291 | |
| | 344 | 344 |
| | 428 | 431 |
| $COO^-$ rocking/CC bending/amide bending | 452 | |
| | 478 | |
| | | 504 |
| O=C-N skeletal deformation | 540 | 544 |
| | 561 | |
| | | 604 |
| $COO^-$ wagging | 622 | |
| | 652 | 669 |
| $CH_2$ and $CH_3$ rocking | 776 | |
| | | |
| | 806 | 815 |
| C-C stretching | 848 | 858 |
| C-C stretching | 895 | 909 |
| C-$COO^-$ Stretching | 926 | 937 |
| Methylene rocking/CC stretching | 1000 | 996 |
| C-N stretching | 1051 | 1056 |
| $NH_2$ rock | 1097 | 1094 |
| $NH_3^+$ deformation | | 1134 |
| C-N asymmetric stretching | 1164 | |
| | 1204 | 1191 |
| | | 1221 |
| | 1260 | |
| $CH_2$ wagging | 1282 | 1274 |
| $CH_2$ wagging | 1308 | 1313 |
| CH deformation | 1330 | 1341 |
| $CH_2$ scissoring | 1356 | |
| $COO^-$ symmetric stretching | 1417 | 1400 |
| $CH_2$ scissoring | 1448 | 1434 |
| | 1496 | 1502 |
| | 1549 | 1567 |

| | | |
|---|---|---|
| $NH_2$ scissors/$NH_2$ deformation/Amide II band | 1606 | |
| C=O Stretching | 1624 | 1621 |
| | 1649 | |
| | 1688 | |

*Table T9: L-Aspartic acid (L-Asp) peak assignments and comparison of normal Raman and SERS spectra.*

| Assignment | Normal Raman | SERS |
|---|---|---|
| Ag-N | 225 | 235 |
| | 272 | |
| | 356 | |
| | | 376 |
| | 410 | 424 |
| $COO^-$ rocking/CC bending/amide bending | 466 | 470 |
| | 552 | |
| | 597 | |
| $COO^-$ wagging | | 634 |
| | 747 | |
| Out of plane $OCO^-$ vibration | 777 | |
| | | 800 |
| | | 839 |
| C-C stretching | 871 | |
| C-C stretching/C-COOH stretching | 900 | |
| C-$COO^-$ stretching | 936 | 930 |
| | | 970( |
| Methylene rocking | 993 | |
| | | 1061 |
| C-C stretching/C-O stretching | 1081 | 1096 |
| $NH_3^+$ deformation | 1116 | 1120 |
| | 1145 | 1154 |
| | 1204 | 1198 |
| $CH_2$ twist and rock/$CH_2$ deformation | 1251 | 1257 |
| | | 1300 |
| CH deformation | 1334 | 1324 |
| $CH_2$ scissoring | 1359 | 1357 |

| | | |
|---|---|---|
| $COO^-$ symmetric stretching | 1419 | 1400 |
| | | 1434 |
| | | 1463 |
| | 1506 | 1507 |
| | 1547 | |
| | | 1579 |
| $NH_2$ scissors/$NH_2$ deformation/Amide II band | 1613 | 1614 |
| $NH_2$ shear vibration | 1690 | |

*Table T10: L-Glutamic acid (L-Glu) peak assignments and comparison of normal Raman and SERS spectra.*

| Assignment | Normal Raman | SERS |
|---|---|---|
| Ag-N | | 224 |
| | 385 | |
| | | 434 |
| | 498 | 503 |
| Deformation of O=C-O and C-C-O/O=CN deformation | 534 | |
| | 573 | 561 |
| | | 610 |
| | 668 | 674 |
| | 705 | |
| | | 772 |
| CC skeletal stretch/C-$CH_3$ stretching | 799 | 805 |
| COOH vibration | 863 | 858 |
| C-C-N stretching | 917 | |
| C-$COO^-$ stretching | 939 | 935 |
| C-C stretching | 965 | 958 |
| | | 1000 |
| C-$NH_2$ stretching/C-N stretching | 1058 | |
| | 1083 | 1079 |
| $NH_3^+$ deformation | 1128 | 1115 |
| | 1146 | |
| | 1213 | |
| $CH_2$ wagging | | 1224 |
| (OH) bending+(CO) stretching | | 1275 |

| | | |
|---|---|---|
| $CH_2$ wagging | 1306 | |
| | 1348 | 1336 |
| $COO^-$ symmetric stretching | 1405 | 1400 |
| $CH_2$ scissoring | 1434 | |
| | | 1503 |
| | | 1567 |
| | | 1619 |
| | 1656 | |

*Table T11: L-Glycine (L-Gly) peak assignments and comparison of normal Raman and SERS spectra.*

| Assignment | Normal Raman | SERS |
|---|---|---|
| Ag-N | | 230 |
| | 355 | |
| | | 443 |
| | 492 | 486 |
| | | 557 |
| | 599 | |
| | | 674 |
| | 695 | |
| | | 727 |
| | | 760 |
| | | 797 |
| | | 832 |
| CC skeletal stretch/C-COO stretching | 891 | 920 |
| | | 941 |
| CC stretching/Methylene rocking | | 997 |
| C-N stretch | 1034 | 1026 |
| | | 1075 |
| $NH_2$ twist | 1107 | 1115 |
| $NH_3^+$ deformation | 1138 | 1140 |
| | | 1185 |
| | | 1273 |
| $CH_2$ wagging | 1323 | |
| | | 1348 |
| $COO^-$ symmetric stretching | 1409 | 1410 |
| | 1438 | 1431 |

| | | |
|---|---|---|
| $CH_2$ scissoring | 1455 | 1466 |
| | | 1503 |
| | 1514 | |
| $COO^-$ antisymmetric vibration | 1566 | |
| $NH_2$ scissoring/COOH stretching | | 1588 |
| | 1667 | |

*Table T12: L-Alanine (L-Ala) peak assignments and comparison of normal Raman and SERS spectra.*

| Assignment | Normal Raman | SERS |
|---|---|---|
| | 216 | |
| Ag-N | | 231 |
| | 262 | |
| | 279 | |
| | 323 | 315 |
| | | 338 |
| | 394 | 389 |
| | | 427 |
| | | 512 |
| Deformation of O=C-O and C-C-O/O=CN deformation | 528 | |
| | | 543 |
| | | 576 |
| | | 615 |
| $COO^-$ wagging | 649 | 649 |
| | | 679 |
| $COO^-$ deformation | | 720 |
| CC vibration, $NH_2$ wagging | 768 | 758 |
| | | 802 |
| C-$CH_3$ stretching | 847 | 843 |
| | | 872 |
| CC stretching | 917 | 914 |
| CC stretching | | 930 |
| $CH_3$rocking | 1016 | 1004 |
| | | 1074 |
| C-N stretching | 1109 | 1102 |
| | 1120 | |

| | | |
|---|---|---|
| $NH_3^+$ deformation | 1143 | 1147 |
| | | 1170 |
| | 1232 | |
| CO stretching | | 1270 |
| $CH_2$ twist and rock | 1301 | |
| $CH_3$ symmetric deformation | 1355 | 1343 |
| | 1374 | |
| $COO^-$ symmetric stretching | 1406 | 1400 |
| | | |
| $CH_3$ asymmetric deformation | 1458 | 1459 |
| | 1478 | |
| | 1495 | 1508 |
| | | 1583 |
| $NH_2$ deformation | 1593 | |
| | | 1626 |

*Table T13: L-Valine (L-Val) peak assignments and comparison of normal Raman and SERS spectra.*

| Assignment | Normal Raman | SERS |
|---|---|---|
| | 207 | |
| Ag-N | | 227 |
| | 283 | |
| | 328 | |
| | 396 | |
| | 430 | |
| Deformation of O=C-O and C-C-O/O=CN deformation | 539 | |
| | | 629 |
| | | 649 |
| $COO^-$ wagging | 661 | 664 |
| | | 681 |
| | 713 | 711 |
| | | 735 |
| $CH_2$ and $CH_3$ rocking | 750 | 747 |
| C-C skeletal stretch | 775 | 787 |
| | 823 | 824 |
| C-C stretching | 847 | |

| | | |
|---|---|---|
| | 899 | 896 |
| C-C stretch | 944 | |
| C-C stretch | 965 | 955 |
| | | 998 |
| C-C strech/C-N stretch/C-$NH_2$ stretch | 1031 | 1043 |
| C-C stretchiong/C-O stretching | 1063 | 1059 |
| | | 1090 |
| | 1144 | 1131 |
| $CH_2$ twist and rock | 1187 | 1201 |
| | | 1231 |
| | 1270 | 1278 |
| $CH_2$ wagging | 1323 | 1311 |
| $CH_3$ symmetric deformation | 1348 | 1348 |
| $COO^-$ symmetric stretching | 1395 | 1393 |
| | 1424 | |
| CH and $CH_3$ deformation | 1451 | 1455 |
| | 1506 | |
| $COO^-$ asymmetric vibration | | 1550 |
| | | 1594 |
| $NH_2$ scissors | | 1625 |
| | | 1653 |
| | | 1732 |

*Table T14: L-Proline (L-Pro) peak assignments and comparison of normal Raman and SERS spectra.*

| Assignment | Normal Raman | SERS |
|---|---|---|
| Ag-N | | 230 |
| | 291 | |
| $COO^-$ rocking/CC bending/amide bending | 447 | |
| | | 556 |
| $COO^-$ wagging | 638 | |
| | 671 | 675 |
| | | 736 |
| | | 758 |
| $CH_2$ deformations in the ring | 789 | 797 |
| | 836 | |

| | | |
|---|---|---|
| | 873 | 879 |
| Pyrrolidine ring breathing | 894 | |
| CC stretch/C-COO stretch | 914 | |
| CC stretching | 948 | 960 |
| $CH_2$ wagging | 989 | 999 |
| C-N stretch | 1029 | |
| C-$NH_2$ stretching/$CH_2$ rocking | 1053 | 1048 |
| | 1079 | 1082 |
| | | 1126 |
| $NH_2^+$ deformation | 1171 | 1165 |
| | | 1189 |
| $CH_2$ twist and rock | 1232 | 1236 |
| | 1261 | 1263 |
| | 1283 | |
| | | 1304 |
| $CH_2$ wagging | 1370 | |
| $COO^-$ symmetric deformation | | 1384 |
| $CH_2$ scissoring | 1451 | 1475 |
| | | 1539 |
| | | 1579 |

*Table T15: L-Leucine (L-Leu) peak assignments and comparison of normal Raman and SERS spectra.*

| Assignment | Normal Raman | SERS |
|---|---|---|
| Ag-N | | 238 |
| | 345 | |
| | 401 | |
| | | 432 |
| $COO^-$ rocking/CC bending/amide bending | 456 | 455 |
| Deformation of O=C-O and C-C-O/O=CN deformation | 532 | 545 |
| | | 594 |
| | | 629 |
| | 667 | |
| | | 709 |
| | | 795 |

| | | |
|---|---|---|
| CC skeletal stretch | 832 | |
| C-C stretching | 845 | |
| C-$COO^-$ stretching | 922 | |
| C-C stretching | 943 | |
| C-C stretching | 960 | |
| | | 1002 |
| $CH_2$ wagging | 1028 | |
| | 1078 | 1083 |
| | 1118 | |
| $NH_3^+$ deformation | 1128 | 1132 |
| | 1170 | |
| $CH_2$ twist and rock/$NH_3$ rocking | 1185 | 1178 |
| $CH_2$ twist and rock | 1237 | 1243 |
| | | 1275 |
| | 1294 | |
| | 1312 | 1316 |
| $CH_3$ symmetric deformation | 1338 | 1344 |
| | 1370 | |
| $COO^-$ symmetric stretching | 1406 | 1396 |
| $CH_2$ scissoring | 1453 | 1452 |
| | 1512 | 1502 |
| | | 1564 |
| | 1623 | |

*Table T16: L-Isoleucine (L-Ile) peak assignments and comparison of normal Raman and SERS spectra.*

| Assignment | Normal Raman | SERS |
|---|---|---|
| | 204 | |
| Ag-N | | 235 |
| | 280 | |
| | 337 | |
| | 360 | |
| | 388 | 376 |
| | 422 | |
| | 447 | 459 |
| | 487 | |
| | | 501 |

| | | |
|---|---|---|
| Deformation of O=C-O and C-C-O/O=CN deformation | 534 | |
| | 555 | 555 |
| | | 582 |
| | 673 | 678 |
| | 707 | 710 |
| | 746 | |
| | 768 | |
| | 799 | |
| | 824 | 824 |
| C-C stretching | 849 | |
| | 872 | |
| C-C stretching | 922 | |
| | 963 | |
| C-C stretching | 990 | 991 |
| C-N stretching | 1029 | |
| | 1085 | |
| $NH_3^+$ deformation | 1134 | |
| | | 1156 |
| $CH_2$ twist and rock | 1187 | |
| | | 1230 |
| $CH_2$ twist and rock | 1256 | 1269 |
| | | 1302 |
| $CH_2$ wagging | 1326 | |
| $CH_3$ symmetric deformation | 1353 | 1343 |
| $COO^-$ symmetric stretching | 1393 | 1400 |
| | 1419 | 1421 |
| $CH_2$ scissoring | 1446 | 1457 |
| | 1512 | 1504 |
| | | 1546 |
| $NH_2$ scissors | | 1584 |
| | 1626 | |

*Table T17: L-Threonine (L-Thr) peak assignments and comparison of normal Raman and SERS spectra.*

| Assignment | Normal Raman | SERS |
|---|---|---|
| Ag-N | | 239 |
| | 307 | |
| | 332 | 333 |
| | 379 | |
| | 415 | |
| | 443 | |
| | 487 | |
| | | 503 |
| Deformation of O=C-O and C-C-O/O=CN deformation | 560 | 558 |
| | | 663 |
| $COO^-$ wagging | 699 | 713 |
| C-OH twisting | 738 | |
| $COO^-$ bending | | |
| | | 813 |
| C-C-N stretching | 869 | |
| C-C stretching | 901 | 891 |
| C-$COO^-$ stretching | 928 | 925 |
| | | 1006 |
| | 1027 | |
| OH deformation | 1042 | 1053 |
| | | 1079 |
| | 1096 | 1100 |
| $NH_3$ rocking vibration | 1112 | |
| | | 1128 |
| | | 1179 |
| $CH_2$ twist and rock | 1192 | |
| | | 1222 |
| $NH_3^+$ deformation | 1248 | 1239 |
| | | 1281 |
| | 1300 | 1314 |
| $CH_3$ symmetric bend | 1338 | 1340 |
| $COO^-$ symmetric stretching | 1414 | 1396 |
| $CH_3$ asymmetric bend | 1448 | 1455 |

| | | |
|---|---|---|
| | 1478 | 1485 |
| | 1546 | 1539 |
| | | 1558 |
| $NH_2$ scissors/COOH stretching | 1595 | 1588 |
| $NH_2$ scissors/$NH_2$ deformation | 1640 | 1631 |

*Table T18: L-Serine (L-Ser) peak assignments and comparison of normal Raman and SERS spectra.*

| Assignment | Normal Raman | SERS |
|---|---|---|
| Ag-N | 220 | 233 |
| | 293 | |
| | 361 | |
| | 511 | 503 |
| | | 547 |
| | 607 | 604 |
| | | 666 |
| | | 689 |
| | | 728 |
| C-C-O symmetric stretching | 811 | |
| CC skeletal stretch | 850 | 847 |
| | | 907 |
| C-C stretching/C-COOH stretching | 919 | |
| C-C stretching | 966 | |
| C-O-H deformation | 1006 | 1015 |
| | | 1048 |
| | 1087 | 1082 |
| $NH_3^+$ deformation | 1120 | |
| | | 1141 |
| $CH_2$ twist and rock | | 1180 |
| | 1214 | |
| | | 1272 |
| $CH_2$ wagging | 1297 | 1303 |
| | 1323 | 1323 |
| | 1364 | 1365 |
| $COO^-$ symmetric stretching | 1410 | 1400 |
| | 1423 | 1427 |

| | | |
|---|---|---|
| $CH_2$ scissoring | 1460 | |
| $CH_3$ deformation | 1477 | |
| | | 1496 |
| | | 1533 |
| $NH_2$ scissors | 1593 | 1582 |
| $NH_2$ scissors/$NH_2$ antisymmetric def. | 1625 | 1615 |

*Table T19: L-Methionine (L-Met) peak assignments and comparison of normal Raman and SERS spectra.*

| Assignment | Normal Raman | SERS |
|---|---|---|
| Ag-N | | 236 |
| | 262 | |
| | | 502 |
| | 542 | 537 |
| $CH_2$-S stretching | 642 | |
| C-S stretch | 679 | 674 |
| S-$CH_3$ stretching | 718 | 716 |
| $CH_2$ and $CH_3$ rocking | 762 | |
| $COO^-$ bending | 804 | |
| | | 824 |
| C-C stretching | 872 | 872 |
| | 985 | |
| | | 1014 |
| C-N stretching | 1071 | 1065 |
| | | 1104 |
| $NH_3^+$ deformation | 1148 | 1149 |
| | | 1197 |
| | | 1256 |
| $CH_2$ wagging | 1318 | |
| | | 1332 |
| $CH_3$ symmetric bend | 1351 | 1368 |
| $COO^-$ symmetric stretching | 1410 | 1410 |
| $CH_2$ scissoring | 1425 | |
| $CH_2$ scissoring | 1445 | 1450 |
| | | 1503 |
| | | 1569 |

# Chapter 7

# Scope for future work

## 7.1 Search for new SERS substrates:

In this work, SERS active substrates were prepared by depositing Ag nanoclusters on different substrates viz. glass, silicon and alumina. Out of these substrates the glass substrates were optimized by suitable heat treatments to get the best SERS signal enhancement. This work can be extended to find the optimum conditions for silver clusters deposited on the silicon and alumina substrates as well as other new substrates such as ITO or Mylar. We have also observed different clusters shapes such as nanorods, spheroidal nanoparticles etc. on alumina substrates. The work can be extended to find suitable conditions to get nanorods which have applications in SERS of biological samples as the LSPR wavelengths in nanorods are shifted to higher values in the infrared region which will not adversely affect the biological samples.

## 7.2 Development of non-invasive glucose sensor:

Accurate D-glucose detection in saliva would be useful to develop a non-invasive glucose sensor. The normal glucose levels in saliva are 80 μM and increase up-to 200 μM in diabetic persons. In the present thesis, D-glucose level in the concentration range of 1 μM-500 μM could be quantitatively detected using SERS. Further work needs to be done using actual saliva sample from human beings and to see if the D-glucose levels can be ascertained. It would also be necessary to correlate the glucose levels

in saliva with blood glucose levels to make a suitable non-invasive glucose sensor

### 7.3 Protein analysis:

Proteins are composed of varying number of amino acids. To analyze the protein SERS spectra we need to have a knowledge of individual amino acids interaction with metal nanoparticles. In the present work we have quantified 19 L-amino acids in the concentration range 1 mM – 1 μM. So this work can be extended for protein analysis.

**List of Publications:**

**Journals**

1. Raju Botta, A. Rajanikanth, C. Bansal, " Surface Enhanced Raman Scattering studies on L-amino acids adsorbed on silver nanoclusters" Chem. Phys. Lett. 618 (2015) 14-19. (2 Citations)
2. Raju Botta, G. Upender, R. Sathyavathi, D. Narayana Rao, C. Bansal, "Silver nanocluster films for single molecule detection using Surface Enhanced Raman Scattering (SERS)" Mat. Chem. Phys. 137 (2013) 699-703. (25 Citations)
3. G. Upender, R. Sathyavathi, B. Raju, C. Bansal, D. Narayana Rao, "SERS studies of molecules on Ag nanocluster films deposited on glass and silicon substrates by cluster deposition method" J. Mol. Struc., 1012 (2012) 56-61. (16 Citations)
4. G. Upender, R. Sathyavathi, B. Raju, K. Shadak Alee, D. Narayana Rao, C. Bansal, "Silver nanocluster films as novel SERS substrates for ultrasensitive detection of molecules" Chem. Phys. Lett., 511 (2011) 309-314. (33 Citations)
5. Raju Botta, A. Rajanikanth, C. Bansal, "Silver nanoclusters films for glucose sensing by Surface Enhanced Raman Scattering (SERS)" Sensing and Bio-sensing Research (Under Review).

**Conference Proceedings**

6. Raju Botta, G. Upender, C. Bansal, " Silver nanocluster films on ITO coated glass as novel substrates for the detection of molecules using Surface Enhanced Raman Scattering (SERS)" IOP Conf. Series: Mater. Sci. Engg. 73 (2015) 012143.

7. Raju Botta, C. Bansal, “Surface enhanced Raman scattering (SERS) study of L-arginine adsorbed on Ag nanoclusters on glass substrate by nanocluster deposition method” AIP Conf. Proc. 1665 (2015) 054007.

**Patent:** Method for quantitative determination of micro molar concentration levels of D-Glucose using Surface Enhanced Raman Spectroscopy (SERS) with 2-Thienylboronic Acid as a linker molecule on silver nanocluster substrates (ApplicationReference Number 3146/CHE/2015).

# Quantitative detection of molecules using Surface Enhanced Raman Spectroscopy with silver nanocluster films as active substrates

ORIGINALITY REPORT

| 9% | 5% | 8% | % |
|---|---|---|---|
| SIMILARITY INDEX | INTERNET SOURCES | PUBLICATIONS | STUDENT PAPERS |

PRIMARY SOURCES

| | | |
|---|---|---|
| 1 | www.researchgate.net<br>Internet Source | 1% |
| 2 | www.kosi.com<br>Internet Source | 1% |
| 3 | Upender, G.. "Silver nanocluster films as novel SERS substrates for ultrasensitive detection of molecules", Chemical Physics Letters, 20110805<br>Publication | 1% |
| 4 | Guicheteau, Jason, Leanne Argue, Aaron Hyre, Michele Jacobson, Steven D. Christesen, and Augustus W. Fountain III. "", Chemical and Biological Sensing VII, 2006.<br>Publication | <1% |
| 5 | Sundaraganesan, N.. "Vibrational spectra, assignments and normal coordinate analysis of 2-amino-5-bromopyridine", Spectrochimica Acta Part A: Molecular and Biomolecular Spectroscopy, 20030315<br>Publication | <1% |